SCUOLA NORMALE SUPERIORE

Graphene for Hydrogen Storage

Sarah Goler

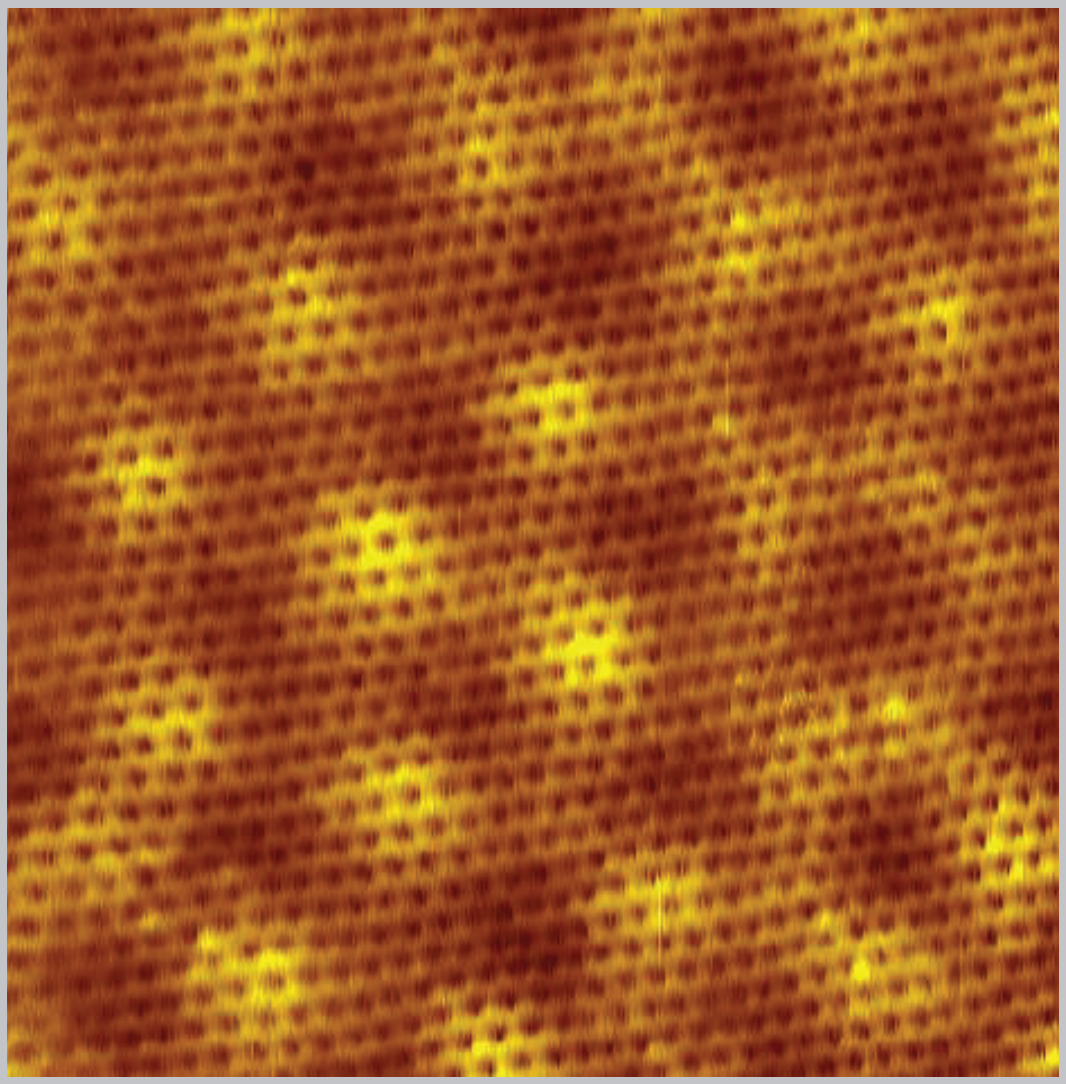

2014

SCUOLA NORMALE SUPERIORE

CLASSE DI SCIENZE

TESI DI PERFEZIONAMENTO IN FISICA DELLA MATERIA CONDENSATA

GRAPHENE FOR HYDROGEN STORAGE

Candidata:
Sarah Goler

Relatori:
Dott. Vittorio Pellegrini
Dott. Stefan Heun
Prof. Fabio Beltram

ANNO ACCADEMICO 2013/2014

Sarah Goler: *Graphene for Hydrogen Storage.*
SUPERVISORS:
Dott. Vittorio Pellegrini
Dott. Stefan Heun
Prof. Fabio Beltram

Miriam my sister and best friend.
I love you.

— Sarah

ABSTRACT

The ever dwindling supply of fossil fuels and the unsustainable growing demand for energy due to worldwide improvements in the quality of life has induced significant increases in fuel prices across the globe. This in turn has lead to research in alternative energy; solar, wind, biofuels, etc. The choice of alternative energy will depend on the specific use and the resources available in the vicinity. One attractive possibility is hydrogen, the third most abundant element available on Earth [1]. However, hydrogen is often found in compounds such as water and must be extracted. The production or extraction of pure hydrogen is an energy consuming process which still requires extensive research to optimize the production methods. Hydrogen is what is called an energy vector meaning that it can be used to store and transport energy. Using only hydrogen and oxygen, hydrogen fuel cells produce electricity with water being the only by-product. The hydrogen energy cycle is sustainable and does not release carbon dioxide, a greenhouse gas, into the environment. However, one of the main hurdles facing a hydrogen based energy economy is hydrogen storage. Hydrogen is a gas at room temperature and pressure, a considerable hindrance to engineering applicable storage devices. Ample funding and research has been allocated to finding and implementing a safe, cheap, nontoxic, and compact method of storing and releasing hydrogen.

There are many solid state materials that absorb and release hydrogen such as metal hydrides, metal organic frameworks, and carbon based materials such as carbon nanotubes. Metal hydrides absorb hydrogen into the lattice. This process requires high temperature and/or high pressure to force the hydrogen into the metal lattice. Furthermore, the metal-hydrogen bonds are often very stable and in order to release the hydrogen, elevated temperatures are necessary. These temperatures are frequently near the melting point of the metal hydride reducing the number of absorption and release cycles possible before the material degrades. Another category of materials for hydrogen storage are metal organic frameworks. These porous structures physisorb molecular hydrogen by weak forces such as the van der Waals force. The magnitude of the attractive force between the hydrogen and the porous structure is small which in turn means that a low temperature is required to release the hydrogen. The density of the molecular hydrogen stored in the porous scaffold can be increased by increasing the hydrogen pressure. Metal organic frameworks occupy large volumes and the density of stored hydrogen is low. These two types of materials exemplify the two different mechanisms of hydrogen bonding, chemisorption and physisorption. Chemical bonds require high temperatures to release the hydrogen while on the contrary, low temperatures are necessary for physisorbed molecular hydrogen which is often unstable at room temperature. These materials are not ideal for hydrogen storage because they rely on huge changes in both the temperature and the pressure to adsorb, store, and release the hydrogen.

Graphene, on the other hand, is an interesting candidate for hydrogen storage. Graphene is a two-dimensional lattice of carbon atoms in a honeycomb configuration. Each carbon atom is covalently bonded to three neighboring carbon atoms forming an sp^2 scaffold. Carbon has four valence electrons so every carbon atom in the graphene lattice can bond with one hydrogen atom forming sp^3 bonds. In 2009, this material was created and given the name graphane [2]. The carbon-hydrogen bonds as mentioned above are extremely stable, requiring high temperatures to break. However, unlike the materials above, theoretical calculations indicate that by controlling the curvature of graphene it is possible to tune the binding energy of atomic hydrogen to the graphene lattice [3]. When the curvature is convex, the C-H bonds are predicted to be stable at room temperature and when the curvature is concave, the C-H bonds are unstable. This provides the possibility of creating a hydrogen storage device that does not depend on a change in pressure or temperature and solely on a change in curvature, a novel idea that has not been achieved yet.

The work presented in this thesis focuses on basic research on the interaction between atomic hydrogen and graphene and the role of curvature on their interaction. We carried out scanning tunneling microscopy experiments on graphene on a periodically corrugated surface. The experiments were performed on monolayer graphene grown on the silicon face of silicon carbide (SiC(0001)). The reason for choosing monolayer graphene on SiC(0001) is that it possesses an intrinsic periodic corrugation on a length scale of about 2nm. The 2nm length scale results in a pronounced curvature of the graphene sheet at the atomic scale. Furthermore, the periodic corrugation of the graphene translates into a spatial equivalency: the scanning tunneling microscopy measurements can be taken on any area of the sample since the corrugation is the same everywhere. We show that the hydrogen adsorption is curvature dependent. Atomic hydrogen bonds to the convex areas of the graphene lattice and not in the concave areas. We were able to identify the stable hydrogen configurations that form on the graphene surface and relate the scanning tunneling microscopy images to images produced via theoretical calculations. The atomic hydrogen bound to the maximally convex areas of the graphene lattice remained adsorbed up to very high temperatures, in agreement with theory. We were able to relate the temperature at which the carbon-hydrogen bond broke to a hydrogen energy desorption barrier using the Arrhenius equation that relates the rate at which the graphene-hydrogen system is heated and the temperature at which the hydrogen desorbs. These studies will lead to an alternative method of hydrogen storage utilizing a graphene based scaffold.

The organization of the thesis begins with background information of graphene pertinent to understanding the experiments presented later on. Subsequently the state of the art in hydrogen storage devices and materials available today is described to establish the pros and cons of graphene based storage in the grand scheme of hydrogen storage devices. The third chapter discusses the growth and characterization (predominantly Raman spectroscopy and scanning tunneling microscopy) of pristine graphene and graphene derivatives with varying intrinsic curvature. The graphene is subsequently exposed to atomic hydrogen in an ultra high vacuum scanning tunneling microscope setup. The stable hydrogen conformations on the graphene surface are atomically resolved and

identified. The curvature dependence of hydrogen adsorption is investigated. The graphene layer is annealed in temperature steps of 50°C, and after each annealing step imaged by scanning tunneling microscopy. The areas of graphene that are convexly curved form the most stable C-H bonds. The results are consistent with density functional theory (DFT) calculations performed at NEST. DFT is a method that employs electron density functions of a system, in this case carbon atoms arranged in a honeycomb lattice, to compute properties of that system. The C-H binding energy as a function of the curvature of the graphene layer or the stable hydrogen configurations that can form on a graphene layer are two such properties that can be calculated using this method. These results lay the basis for developing a hydrogen storage device based on graphene that adsorbs and releases hydrogen by changing the local curvature of the graphene sheet. A possible method for modifying the curvature is suggested in the conclusions.

PUBLICATIONS

Some ideas and figures have appeared previously in the following publications:

S. Goler, C. Coletti, V. Tozzini, V. Piazza, T. Mashoff, F. Beltram, V. Pellegrini, S. Heun. The influence of graphene curvature on hydrogen adsorption: towards hydrogen storage devices. *The Journal of Physical Chemistry C*, 117: 11506-11513, 2013.

S. Goler, C. Coletti, V. Pellegrini, K. V. Emtsev, U. Starke, F. Beltram, S. Heun. Revealing the atomic structure of the buffer layer between SiC(0001) abd epitaxial graphene. *Carbon*, 51: 249-254, 2013.

S. Goler, J. Yan, V. Pellegrini, A. Pinczuk. Raman spectroscopy of magnetophonon resonances in graphene and graphite. *Solid State Communications*, 152: 1289-1293, 2012.

S. Goler, V. Piazza, S. Roddaro, V. Pellegrini, F. Beltram, P. Pingue. Self-assembly and electron-beam-induced direct etching of suspended graphene nanostructures. *Journal of Applied Physics*, 110: 0064308, 2011.

J. Yan, S. Goler, T. D. Rhone, M. Han, P. Kim, V. Pellegrini, A. Pinczuk. Observation of magnetophonon resonance of Dirac fermions in graphite. *Physical Review Letters*, 105: 227401, 2010.

J. Yan, Y. Zhang, S. Goler, P. Kim, A. Pinczuk. Raman scattering and tunable electron-phonon coupling in single layer graphene. *Solid State Communications*, 143: 39-43, 2007.

ACKNOWLEDGEMENTS

There are so many people who have contributed to my growth both as a scientist and as a woman in science in these formative years of my life.

I would like to thank Vittorio Pellegrini who believed in me. You taught me to think independently, an invaluable skill that will serve me throughout my scientific career. I cannot thank you enough for the time, patience, and kindness you showed me. I will share the gift you imparted to me by teaching a young student.

Stefan Heun was another important figure during my PhD, helping me in the STM lab, being available for scientific discussions and critically reviewing my papers and thesis.

I would like to thank Professor Fabio Beltram for giving me a chance to complete my PhD at the Scuola Normale Superiore although I needed a year to find my footing and learn Italian.

One of the most influential people, who set me on the path towards research and a PhD is Aron Pinczuk. You sparked curiosity in me.

Many, many people at NEST contributed to my growth and research and I would like to thank you all. You made Pisa my home. Here I will name just a few. Massimo and Torge for all the hours fixing the STM and trying not to laugh for fear of disturbing the measurements. Vincenzo, Pasquale, Valentina, Marco, and Bisu for sharing their knowledge with me. Alessandro T., for always being cheerful. Cami, who is an exceptional scientist, a brilliant teacher, and one of my dearest friends. Vale, you have always been there for me, even when I have showed up in the middle of the night at your doorstep for a hug, tea, and a film. Ang, a great friend. César, Stefano, Daniele, Giorgio and Elia, I will always think of you when I look back at this period in my life.

Seb, I hold your friendship closest to my heart.

Silvio, for always making me smile and sharing your life with me.

Lastly, I want to thank my family. Mom, you are the most amazing woman I have ever met. Miriam, you are my best friend and fan. Jayne, I am lucky to have you. Neil, you are the father I have always wanted. Irvila, not a day has passed without the need to share something special with you. Aaron, my brother and all the rest of my wonderful family. I love you all.

CONTENTS

I THESIS 1

1 INTRODUCTION TO GRAPHENE 3
- 1.1 Introduction to Graphene 3
- 1.2 What is Graphene? 4
- 1.3 Band Structure 4
- 1.4 Phonons 8
- 1.5 Raman Spectroscopy: Introduction to the Technique 10
- 1.6 Raman Spectroscopy in Graphene 11
- 1.7 Phonons in Magnetic Fields 14

2 STATE OF THE ART IN HYDROGEN STORAGE 17
- 2.1 Towards a Hydrogen Based Energy Technology 17
  - 2.1.1 Hydrogen Production 17
  - 2.1.2 Energy Production by Fuel Cells 18
- 2.2 State of the Art in Hydrogen Storage Materials 19
  - 2.2.1 High Pressure Tanks 19
  - 2.2.2 Hydrogen Storage in Solids 20
  - 2.2.3 Metal Hydrides 20
  - 2.2.4 Metal Organic Framework 21
  - 2.2.5 Carbon-Based Materials 22
  - 2.2.6 Why Graphene? 22
  - 2.2.7 Physisorption 23
  - 2.2.8 Chemisorption 23

3 GRAPHENE GROWTH AND CHARACTERIZATION 25
- 3.1 Crystal Structure of Silicon Carbide 25
- 3.2 Growth on Silicon Carbide 25
  - 3.2.1 Hydrogen Etching Process 30
  - 3.2.2 Growth Process 32
  - 3.2.3 Hydrogen Intercalation 33
- 3.3 Techniques for Sample Characterization 34
  - 3.3.1 Raman Spectroscopy: Setup 34
  - 3.3.2 STM Theory 35
  - 3.3.3 Scanning Tunneling Spectroscopy Theory 36
  - 3.3.4 Tip Etching 37
  - 3.3.5 In Situ Tip Preparation 37
  - 3.3.6 STM Setup 39
- 3.4 Buffer Layer on SiC 41
  - 3.4.1 Characterization of the Buffer Layer 41
  - 3.4.2 Atomically-Resolved STM Images of the Buffer Layer 44
  - 3.4.3 Corrugation 48
  - 3.4.4 STS Analysis 48
- 3.5 Monolayer Graphene on SiC 50
  - 3.5.1 Characterization of Monolayer Graphene 50
  - 3.5.2 Atomically-Resolved STM Images of Monolayer Graphene 52

3.5.3 Corrugation 53
3.5.4 STS Analysis 53
3.6 Quasi-Free-Standing Monolayer Graphene on SiC 57
3.6.1 Characterization of Quasi-Free-Standing Monolayer Graphene 57
3.6.2 Atomically-Resolved STM Images of Quasi-Free-Standing Monolayer Graphene 58
3.6.3 Corrugation 59
3.6.4 STS Analysis 60
4 HYDROGEN ON CORRUGATED GRAPHENE 61
4.1 Hydrogen Interaction on Corrugated Monolayer Graphene 62
4.1.1 Experiment 62
4.1.2 Results After a 5 Second Exposure to Atomic Hydrogen 64
4.1.3 Hydrogen on Graphene Compared to Other Carbon Materials 74
4.2 Hydrogen on the Buffer Layer 78
4.2.1 Experiment 78
4.2.2 Results 79
4.3 Conclusions 79
5 CONCLUSIONS 83

II APPENDIX 87
A CALCULATING THE ATOMIC FLUX OF HYDROGEN 89

BIBLIOGRAPHY 91

Part I

THESIS

1 INTRODUCTION TO GRAPHENE

The purpose of this chapter is to introduce graphene and provide descriptions of the basic physical properties that will be used throughout the thesis.

1.1 INTRODUCTION TO GRAPHENE

Writing has been an integral part of society dating back to the Sumer in Mesopotamia. Leaving a mark has been indispensable for civilizations and as a consequence, throughout history scribes have held eminent positions in society. Ancient civilizations carved their stories in stone and used various dyes to depict events on cave walls, animal skins, and plant based paper such as papyrus. For centuries, ink and dye were the predominant forms of writing. It was not until recently, in the history of writing, that the pencil was invented. In around 1565, the first pencils were produced in Cumberland England [4, 5]. The discovery of a dark, metallic, soft, oily material later recognized as graphite but at the time called plumbago [6], since it resembled lead, became the basis for the first pencils. The chemical composition was unknown until the late 1800's and it was not until 1789 when Abraham Gottlob Werner conceived of the name graphite derived from the Greek word *grafo*, to write [4, 5].

Graphite is a carbon allotrope comprised of layering two-dimensional crystal planes known as graphene. In a single plane, the carbon atoms are arranged in a honeycomb lattice. Each carbon atom has six electrons, two forming the 1s shell and four valence electrons 2s2p. Three of the valence electrons are bound to neighboring carbon atoms in the plane forming σ bonds, leaving one electron unbound. Less energy is required to fill a $2p_x$ and a $2p_y$ orbital than placing two electrons in the 2s orbital, resulting in the sp^2 hybridization [7]. The in-plane carbon bonds are extremely strong, however only van der Waals forces hold the layers together [8]. The weak inter-layer coupling is responsible for the writing capacity of graphite. The graphene layers can slide along each other leaving thin layers of graphite on the paper.

True 2D crystals were not believed to be thermodynamically stable [9] but the creation of graphene in 2004 proved otherwise [10, 11]. The first monolayers of graphene were created via a micromechanical method known as the scotch tape method. Graphite is cleaved recurrently by folding a piece of scotch tape back on itself repeatedly. Subsequently, the scotch tape is placed adhesive side down on a substrate. Once the tape is removed the substrate is left with a jumble of graphene, graphite and glue. Typically the substrate is silicon with a 300 nm layer of SiO_2 which increase the contrast of single to few layer graphene [12]. This striking effect allows for the optical identification of monolayer graphene.

The micromechanical method is time consuming and the graphene size and shape cannot be controlled. It is not a viable mode of producing graphene for industrial purposes. As a consequence, a variety of alternative methods of

producing high quality graphene are being explored such as epitaxial graphene grown on copper [13] or ruthenium [14], graphene transferred to hexagonal boron nitride [15], and silicon-carbide decomposition which will be discussed in greater depth in chapter 3.

1.2 WHAT IS GRAPHENE?

As mentioned briefly above, graphene is a single layer of graphite with the carbon atoms in a hexagonal lattice with a carbon-carbon spacing of 1.42 Å. The lattice is a compilation of two identical interpenetrating triangular sublattices. In Fig. 1, the two sublattices are labeled A and B. The three nearest neighbors of an atom in sublattice A are from the sublattice B and vice versa. The vectors that describe the positions of the nearest neighbors of an A atom are:

$$\mathbf{R}_1 = (\tfrac{a}{\sqrt{3}}, 0)$$

$$\mathbf{R}_2 = (-\tfrac{a}{2\sqrt{3}}, -\tfrac{a}{2})$$

$$\mathbf{R}_3 = (-\tfrac{a}{2\sqrt{3}}, \tfrac{a}{2})$$

The unit vectors in real space are:

$$\mathbf{a}_1 = (\tfrac{\sqrt{3}a}{2}, \tfrac{a}{2})$$

$$\mathbf{a}_2 = (\tfrac{\sqrt{3}a}{2}, -\tfrac{a}{2})$$

Here a equals 2.46 Å or $|\mathbf{a}_1| = |\mathbf{a}_2|$ = 1.42 Å x $\sqrt{3}$ = 2.46 Å [7]. The hexagonal lattice in real space translates into a hexagonal lattice in reciprocal space with a rotation of 90° and unit vectors [7]:

$$\mathbf{b}_1 = (\tfrac{2\pi}{\sqrt{3}a}, \tfrac{2\pi}{a})$$

$$\mathbf{b}_2 = (\tfrac{2\pi}{\sqrt{3}a}, -\tfrac{2\pi}{a})$$

1.3 BAND STRUCTURE

The hexagonal arrangement of carbon atoms leads to unique physics where the electrons react as if they are massless Dirac fermions. To arrive at this point, the band structure of monolayer graphene will be derived using a tight binding method. Bloch wavefunctions consisting of the p_z orbitals centered on the carbon atoms are the basis for resolving the Schrodinger equation [16]:

$$H\psi_{\mathbf{k}}(\mathbf{r}) = E(\mathbf{k})\psi_{\mathbf{k}}(\mathbf{r}) \tag{1}$$

H is the Hamiltonian that describes the coupling between nearest neighbor carbon atoms and E($\mathbf{k}$) denotes the energy eigenvalues which form the electronic

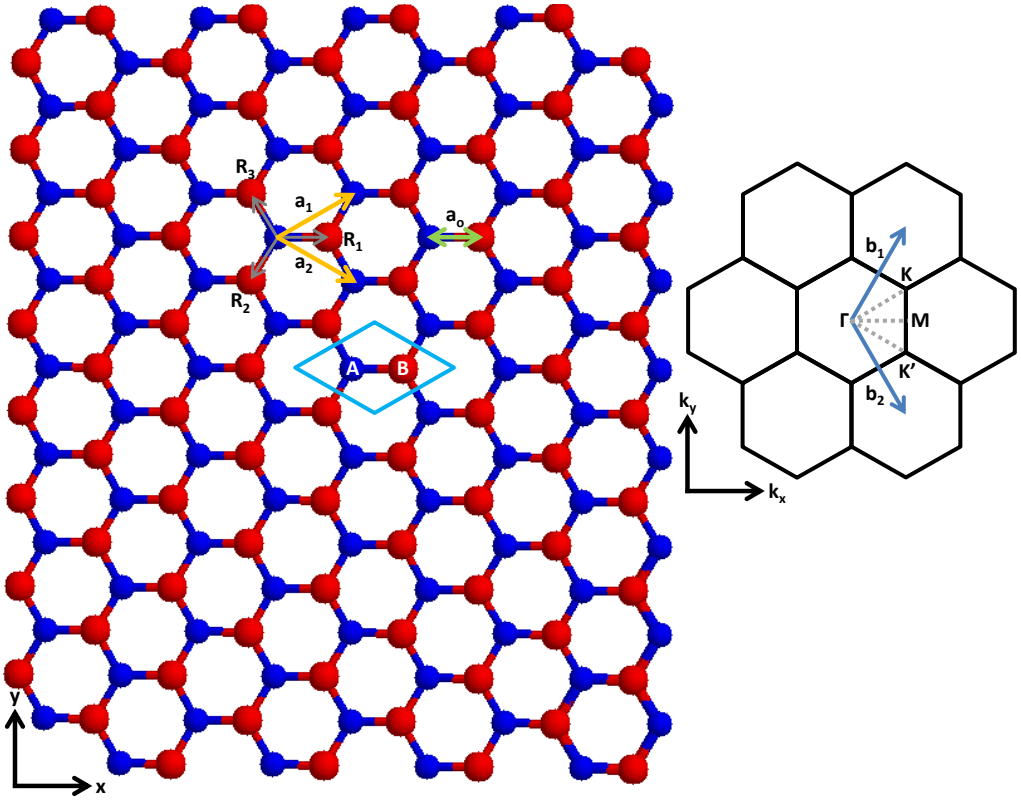

Figure 1: The graphene lattice in real space is shown on the left. The two sublattices are differentiated by color, blue and red. The unit cell is indicated by the blue diamond encompassing two atoms labeled A and B. $\mathbf{a}_\circ$ is the distance between neighboring carbon atoms, 1.42 Å. The unit vectors in real space are labeled $\mathbf{a}_1$ and $\mathbf{a}_2$ and the vectors indicating the nearest neighbor carbon atoms are $\mathbf{R}_1$, $\mathbf{R}_2$, and $\mathbf{R}_3$. The hexagonal reciprocal lattice is shown on the right rotated by 90°. The points of symmetry are labeled and the unit vectors $\mathbf{b}_1$ and $\mathbf{b}_2$ are indicated.

band structure. H was first resolved in 1947 by Wallace, as a first approximation for the band structure of graphite [17].

$$\psi^{\mathbf{k}}_{A(B)}(\mathbf{r}) = \frac{1}{\sqrt{N}} \sum_{A(B)} e^{i\mathbf{k}\mathbf{r}_{A(B)}} \Phi_{A(B)}(\mathbf{r} - \mathbf{r}_{A(B)}) \tag{2}$$

are the Bloch wavefunctions centered on the atoms in the sublattices, A and B with a contribution from the p_z orbitals. The p_z orbitals are an appropriate choice for deriving the electronic band structure because they are responsible for the valence band and the conduction band of graphene. The valence and conduction bands are much higher in energy than the bands that form due to the strong intralayer carbon-carbon bonds [16]. The number of unit cells is given by N and the positions of the atoms is given by $\mathbf{r}_A$ or $\mathbf{r}_B$, where the letter denotes the sublattice. $\mathbf{k}$ is the crystal momentum. A linear combination of the Bloch wavefunctions is the basis for resolving the secular equation given by [16]:

$$\begin{vmatrix} H_{AA} - E(\mathbf{k})S_{AA} & H_{AB} - E(\mathbf{k})S_{AB} \\ H^*_{AB} - E(\mathbf{k})S^*_{AB} & H_{BB} - E(\mathbf{k})S_{AA} \end{vmatrix} = 0 \tag{3}$$

In the characteristic equation above, only the nearest neighbor carbon atoms are included. Furthermore, since the two sublattices are identical, the matrix elements H_{AA} and H_{BB} are equal [16]. Using the same reasoning, $S_{AA} = S_{BB}$ since the overlap integral of an atomic wavefunction centered on itself is the same on both sublattices [16].
The determinant is given by:

$$(S^2_{AA} - S^*_{AB}S_{AB})E^2 + (H^*_{AB}S_{AB} + S^*_{AB}H_{AB} - 2H_{AA}S_{AA})E + (H_{AA}H_{BB} - H^*_{AB}H_{AB}) = 0 \tag{4}$$

When considering only nearest neighbors, the following equations for the matrix elements are derived [16]:

$$H_{AA} = \frac{1}{N} \sum_{A} e^{i\mathbf{k}\cdot(\mathbf{r}_A - \mathbf{r}_A)} < \Phi_A(\mathbf{r} - \mathbf{r}_A) \, |H| \, \Phi_A(\mathbf{r} - \mathbf{r}_A) > \tag{5}$$

H_{AA} is the Hamiltonian between two identical Bloch functions at the atomic position A which is simply the energy related to the $2p_z$ orbital [16, 18]. This constant does not affect the shape of the dispersion bands therefore it can be set to zero.

$$S_{AA} = < \Phi_A(\mathbf{r} - \mathbf{r}_A) \, | \Phi_A(\mathbf{r} - \mathbf{r}_A) > = 1 \tag{6}$$

S_{AA} is the overlap integral of a Bloch function onto itself which equals 1, assuming that the Bloch wavefunctions are normalized [16].

$$H_{AB} = \frac{1}{N} \sum_{A,B} < \Phi_A(\mathbf{r} - \mathbf{r}_A) \, |H| \, \Phi_B(\mathbf{r} - \mathbf{r}_B) > e^{i\mathbf{k}\cdot(\mathbf{r}_B - \mathbf{r}_A)} \tag{7}$$

H_{AB} is the Hamiltonian between two nearest neighbor atoms. It can be written as [16]:

$$H_{AB} = \gamma_\circ \sum_B e^{i\mathbf{k}\cdot(\mathbf{r}_B - \mathbf{r}_A)} = \gamma_\circ f(\mathbf{k}) \tag{8}$$

$$\gamma_\circ = \frac{1}{N} \sum_A < \Phi_A(\mathbf{r} - \mathbf{r}_A) \, |H| \, \Phi_B(\mathbf{r} - \mathbf{r}_B) > \tag{9}$$

where $\gamma_\circ$ is the hopping integral between two atoms in the lattice and has a value of $\sim$ 2.8 eV [19]. When the nearest neighbor vectors $(\mathbf{R}_1, \mathbf{R}_2, \mathbf{R}_3)$ are inserted into the Hamiltonian H_{AB}, the function $f(\mathbf{k})$ is obtained as

$$f(\mathbf{k}) = e^{ik_x a/\sqrt{3}} + 2e^{-ik_x a/2\sqrt{3}} \cos\left(\frac{k_y a}{2}\right) \tag{10}$$

The solution to the secular equation with the approximations stated previously is [7, 16]:

$$E^{\pm}(\mathbf{k}) = \pm\gamma_\circ \sqrt{f(\mathbf{k})^2} = \pm\gamma_\circ \sqrt{1 + 4\cos\frac{\sqrt{3}k_x a}{2} \cos\frac{k_y a}{2} + 4\cos^2\frac{k_y a}{2}} \tag{11}$$

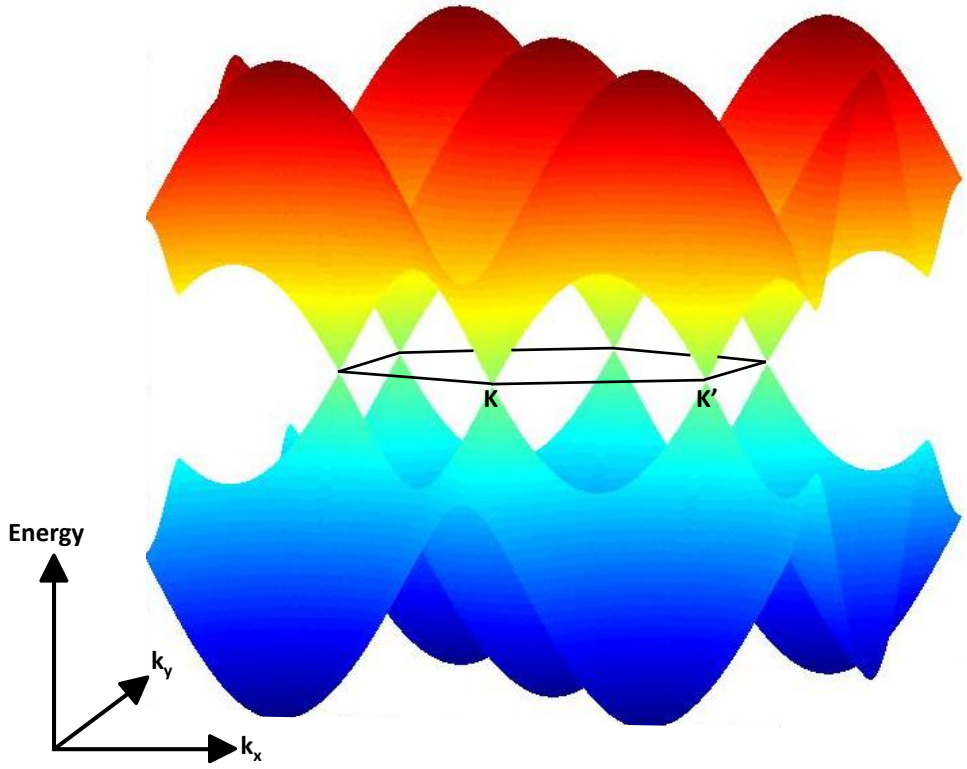

Figure 2: The electronic band structure of graphene. The Dirac points, **K** and **K'**, are indicated. Close to the Dirac points, the dispersion is linear.

By plotting the energy as a function of **k**, the well known dispersion curve for graphene is obtained (Fig. 2). The valence and conduction bands decrease

symmetrically to points at the six vertices of the Brillouin zone (black line in Fig. 2). These six points are known as the Dirac points or K(K′) points where the valance band touches the conduction band. Near these points, the dispersion curve becomes nearly linear and is often approximated as linear. A linear dispersion has non-trivial implications when studying the electronic properties of graphene. Typically in semiconductors such as GaAs or Si, the electronic band dispersion is quadratic around points of high symmetry. This results in a constant effective mass of the electrons that is different from the rest mass of an electron due to the interaction with the periodic lattice. In the case of graphene, the effective mass of the electrons is zero around the Dirac points so that the physics in this crystal mimics that of relativistic particles with an electron speed approximately 300 times slower than the speed of light.

1.4 PHONONS

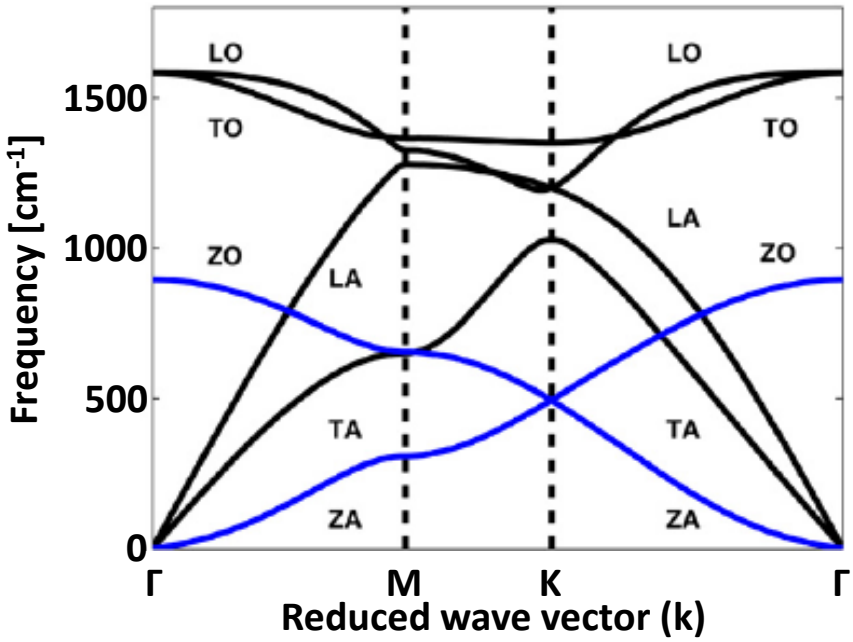

Figure 3: Graphene phonon dispersion. The longitudinal acoustic (LA) and transverse acoustic (TA) in-plane modes go to zero at Γ. The third acoustic mode (ZA) is an out of plane mode. There are also three optical modes of which two are in-plane stretching modes, longitudinal optical (LO) and transverse optical (TO) and one is an out of plane mode (ZO). Figure taken from reference [20].

The phonon dispersion in graphene (Fig. 3) has six branches resulting from the two carbon atoms in the unit cell. Common to all three acoustic modes at the Γ point, the displacement has no restoring force and the phonon frequency is zero [7]. The atomic motion of the three acoustic branches at the Γ point is shown in Fig. 4. There are also three optical phonon modes, two of which are degenerate at the Γ point. The degeneracy is a consequence of the two identical carbon atoms in the unit cell of graphene. The in-plane stretching modes are defined as longitudinal or transverse optical depending on the orientation of

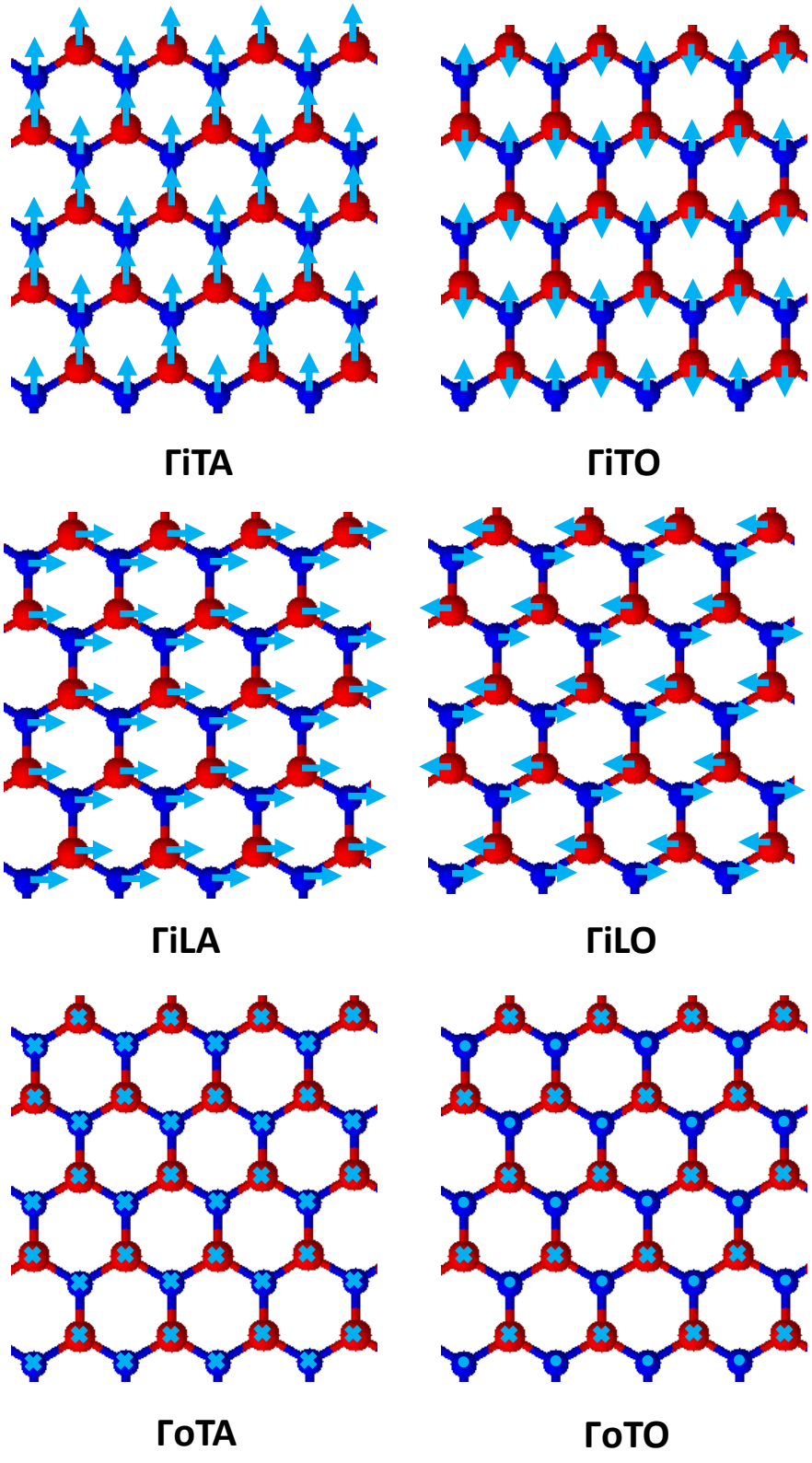

Figure 4: Graphene phonon modes at the Γ point in reciprocal space. The in-plane longitudinal acoustic (ΓiLA), in-plane transverse acoustic (ΓiTA) and out-of-plane transverse acoustic (ΓoTA) modes go to zero at Γ since the motions are translational, moving the entire graphene plane in a given direction. The longitudinal optical (ΓiLO) and transverse optical (ΓiTO) in-plane stretching modes are degenerate at the Γ point. The ΓiLO and ΓiTO modes gives rise to the G band observed in graphene. The out-of-plane transverse optical mode (ΓoTO) is also shown.

the carbon-carbon bond motion with respect to the excitation wavevector [7]. These optical in-plane stretching modes (ΓiTO and ΓiLO) are recorded by Raman spectroscopy and are responsible for the G band in graphene. The third optical mode is an out-of-plane stretching mode in which all the atoms in one sublattice move opposite to those in the intertwined sublattice as shown in Fig. 4.

1.5 RAMAN SPECTROSCOPY: INTRODUCTION TO THE TECHNIQUE

Light scattering provides a plethora of information about the fundamental properties of materials including such information as crystal structure, defects, vibrational or phonon mode structure, and phonon dynamics. In the basic modern light scattering experiment, a laser with a known wavelength is focused onto a material of interest and the photons scattered by the material are collected and analyzed in terms of such parameters as wavelength, polarization, scattering angle, and the like. Most of the scattered light has the same wavelength as the laser, but a small amount of the scattered light changes wavelength. When the wavelength is unchanged during the scattering process, it is known as elastic light scattering or Rayleigh scattering. On the other hand, a small amount of the scattered radiation has a different frequency from the excitation photon due to the creation or annihilation of a quantized excitation in the material [21]. This light scattering process is inelastic and known as the Raman effect [21]. Raman spectroscopy was acknowledged as an extremely valuable nondestructive method for extracting structural and chemical information of a material in 1930 when Sir Chandrasekhara Raman received the Nobel prize for his work on the subject [22].

A great many introductory and advanced texts have been written on the theory and selection rules responsible for the excitations visible by Raman spectroscopy [7, 23, 24]. In this thesis, Raman spectroscopy is primarily used as a tool for verifying the quality and types of materials being studied. More specifically it was utilized to distinguish how many graphene layers were present in the sample. For this reason, the discussion on Raman spectroscopy is limited to a short description of the laws governing the process.

As mentioned above, Raman spectroscopy is an inelastic light scattering process where the emitted photon has a different energy from the excitation photon due to the creation or destruction of a phonon in the material. When the emitted photon has a lower energy than the initial photon, the process is known as the Stokes process. If however, a quantized excitation is annihilated, increasing the energy of the emitted photon, it is known as the anti-Stokes process. In this thesis, only the Stokes process will be considered since all the measurements were taken at room temperature and the phonon population of graphene would mostly be in the ground state.

The Raman process abides by two conservation laws: conservation of energy which was stated above and conservation of momentum. Energy conservation can be expressed mathematically as:

$$E_i - E_f = E_{ph} \tag{12}$$

The energy difference between the excitation photon (E_i) and the measured photon (E_f) is exactly the energy of the phonon (E_{ph}).

The second conservation law is a result of the translational symmetry of the crystal and can be expressed as:

$$k_i - k_f = q_{ph} \tag{13}$$

Here k_i refers to the wavevector of the initial electron-hole pair excited by the incoming photon. k_f is the final photon wavevector after a phonon with momentum q_{ph} is created during the electron-phonon interaction. The excitation laser used in these experiments is in the visible range, 488 nm to be precise. The unit cell of graphene is 2.46 Å meaning that an excitation caused by a photon is nearly vertical in the Brillouin zone of graphene. Since photons in the visible have very small wavevectors, the area of the phonon spectrum accessible when considering first order processes alone is restricted to the Brillouin zone center, (Γ). When higher order processes with multiple quantum excitations are considered, then the individual phonons can have larger wavevectors provided that the sum of the wavevectors is nearly zero to satisfy the conservation of momentum.

1.6 RAMAN SPECTROSCOPY IN GRAPHENE

Graphene has a characteristic Raman spectrum which has become a standard in both identifying the number of layers in the sample as well as the quality of the graphene. There is a first order Raman mode in graphene known as the G mode. First order Raman spectroscopy probes the zone center phonons at the Γ point (Fig. 3). The E_{2g} phonon is an in-plane stretching motion of the two sublattices, A and B (see Fig. 4 ΓiTO and ΓiLO). In monolayer graphene, the G mode is a sharp peak centered at ~1585 cm^{-1} (Fig. 5). The width of this peak can provide information on the phonon lifetime. This phonon mode is also sensitive to the carrier density of the graphene layer [25, 26, 27] and lattice strain [28, 29].

In monolayer graphene there is a second very prominent sharp Raman peak at around 2700 cm^{-1} known as the 2D peak (Fig. 5). This is a second order process that requires two phonons with equal and opposite wavevectors in order to satisfy the momentum conservation law (discussed in more detail in chapter 3). When this condition is satisfied, a resonance occurs and a sharp peak appears around 2700 cm^{-1}. The exact position is excitation energy dependent since the peak shifts with the electronic band structure. Surprisingly, in monolayer graphene this peak is always much more intense than the G peak which is unexpected given that it is a second order Raman process.

The 2D peak is sensitive to the number of graphene layers [30]. There is a radical difference between single and bilayer graphene since the double resonance process depends on the electronic band structure as well as the phonon dispersion of graphene. The Dirac points in monolayer graphene consist of a single set of bands that cross. Therefore, the resonance condition is reached when the phonon emitted near Dirac cone K has the same magnitude but inverse direction as the phonon emitted near the Dirac cone K'. This intervalley process results in a single sharp peak at around 2690 cm^{-1} (Fig. 6a inset).

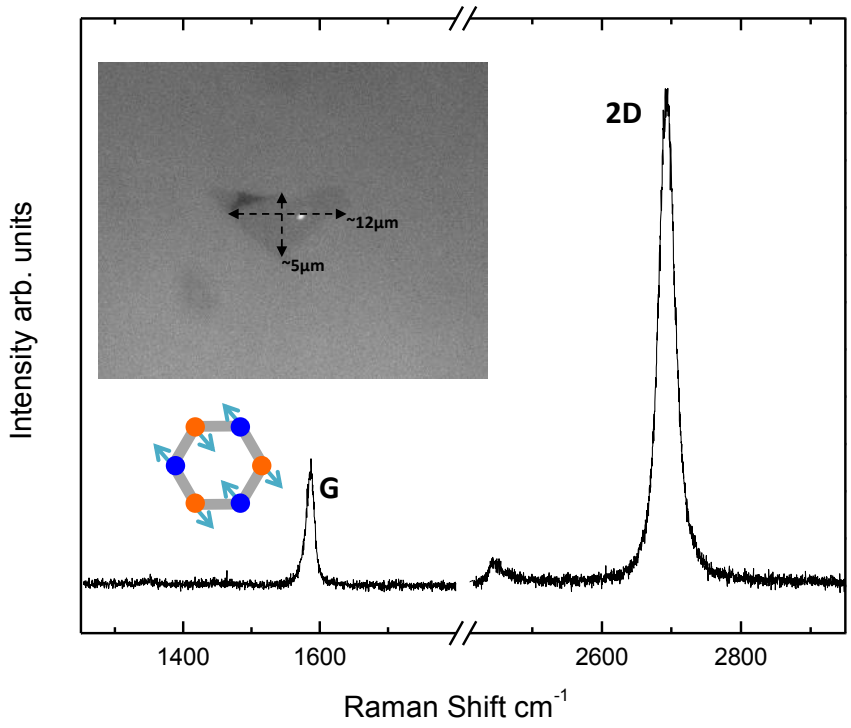

Figure 5: Raman spectrum of monolayer graphene produced by micromechanical exfoliation. The G mode is at 1585 cm^{-1} with a full width at half maximum (FWHM) of 16 cm^{-1} and the 2D mode is at 2700 cm^{-1} with a FWHM of 25 cm^{-1}. Both peaks were fitted with a single Lorentzian curve to extract the peak position and the FWHM. The spectrum lacks a D peak around 1350 cm^{-1} indicating that the graphene layer is of high quality. The inset is a CCD image of the graphene layer and the white dot is the laser spot. A diagram of the G mode is shown.

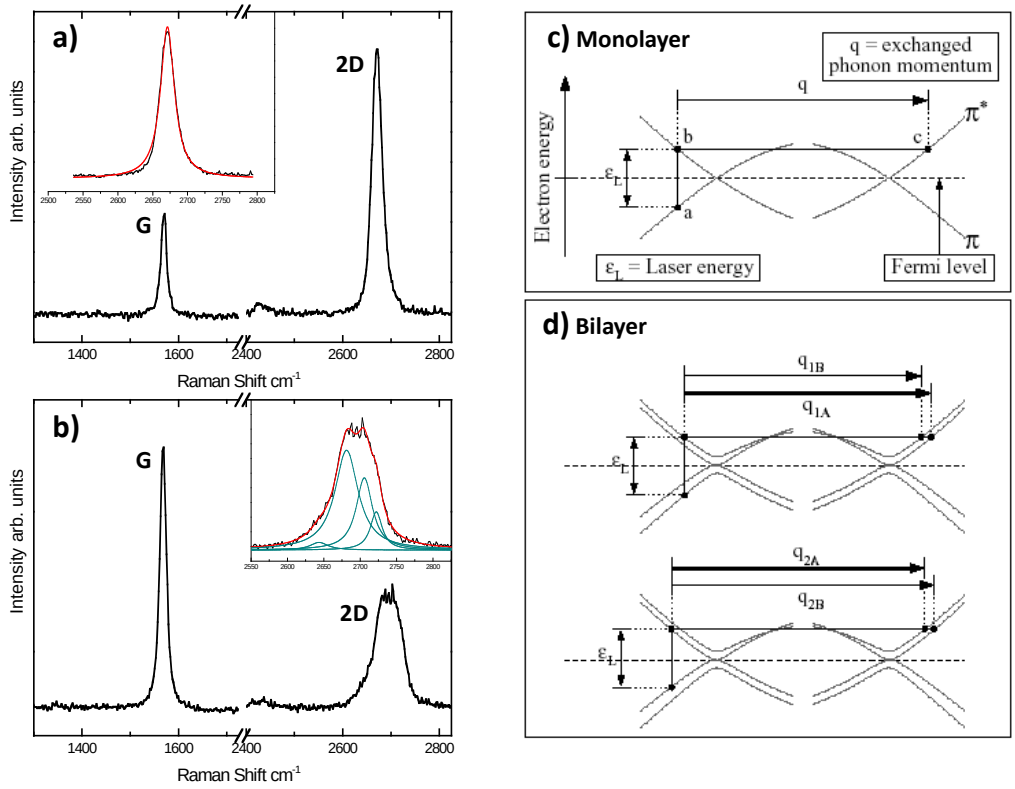

Figure 6: Comparison of the 2D band in monolayer and bilayer graphene. a) Raman spectrum of monolayer graphene with an inset of the 2D band fitted with a single Lorentzian curve. b) Raman spectrum of bilayer graphene with an inset of the 2D peak fitted with four curves. c) and d) are schematics of the 2D Raman process. The electronic band structure in monolayer graphene (panel c) around the Dirac points splits into four bands in bilayer graphene resulting in the 2D peak visible in panel b). c) and d) are from reference [30].

In bilayer graphene, the electronic band structure around the Dirac neutrality points is split into two π and π^* bands. The energy splitting between the two pairs of respective bands is small. With the same reasoning as for the monolayer case, there are four possible recombination processes that become resonant for any given excitation wavelength. Since the electronic band splitting is small, these four peaks overlap to create a broad 2D peak. The probability of electron-phonon coupling is stronger for two of the recombination pathways, which is responsible for the 2D shape seen in Fig. 6b. [30]

A third Raman peak is occasionally visible in graphitic spectra known as the D peak at ~1350 cm^{-1} due to the longitudinal optical phonons that require either a defect or an edge for activation [31]. This Raman mode does not conserve wavevector. It is a radial breathing mode in which all six carbon atoms in the hexagonal lattice move towards and away from the center of the hexagon. In pristine graphene with no defects, the D peak is not visible (Fig. 5).

The Raman spectra shown so far have all been from micromechanically exfoliated graphene. The same analysis can be performed on graphene produced by the decomposition of silicon carbide but the spectra are not as clear. There is a pronounced background from the silicon carbide crystal rendering the identification of monolayer graphene a more intensive process.

1.7 PHONONS IN MAGNETIC FIELDS

Phonon modes have been studied not only at zero magnetic field but also in magnetic fields. An interesting effect arises in semiconductors when a magnetic field is tuned so that the inter-Landau level energy difference is close to or equal to an optical phonon mode. This effect is called magneto-phonon resonance (MPR). When the inter-Landau level electronic transitions (Fig. 7b) in graphene have an energy comparable to the E_{2g} (G band) optical phonon at ~1585 cm^{-1} or ~196 meV (Fig. 7a), a resonance is observed.

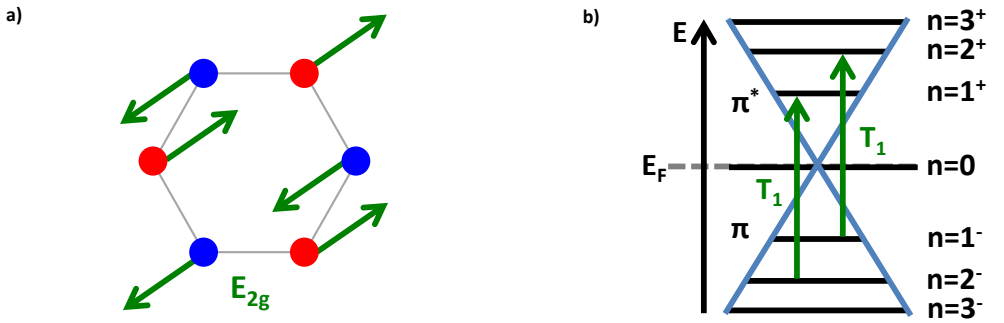

Figure 7: a) The atomic displacements corresponding to the E_{2g} (G mode) phonon. b) The inter-Landau level transitions that couple with the E_{2g} phonon are indicated by vertical arrows. The horizontal lines represent the Landau levels in monolayer graphene. Figure taken from reference [32].

The energy of the Landau levels in graphene is given by

$$\epsilon_{n^{\pm}} = \pm\sqrt{2n}\frac{\hbar v_f}{l_B} \tag{14}$$

n is a non-negative integer that labels the Landau levels. The positive energy values are in the π^* and negative energy values are in the π band. The $n = 0$ Landau level is at the Dirac point in graphene. The electron velocity is given by $v_f = 1.03x10^8$ cm/s [33]. The magnetic length is $l_B = (\frac{\hbar c}{|e|B})^{\frac{1}{2}}$.

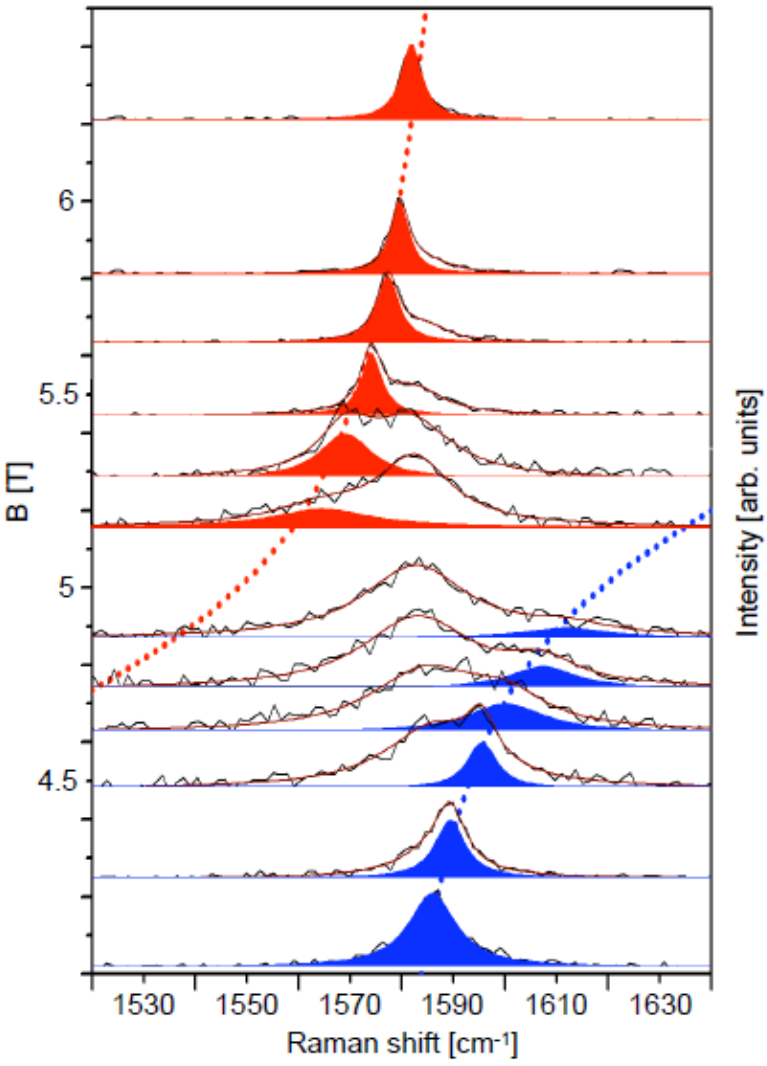

Figure 8: Raman spectra for magnetic fields ranging from 4.2T to 6.4T. The spectra are shifted vertically so that the peak positions of the two coupled modes (red and blue) are aligned with the anticrossing fit given by equation 15. Figure taken from reference [33].

Raman spectroscopy can be used to study MPR. Surprisingly, this phenomenon was seen in kish graphite at the magnetic field of 4.7T. This corresponds to the inter-Landau level transitions given by the expression above for graphene from $n = -2$ to $n = 1$ and $n = -1$ to $n = 2$ [33]. The MPR appears as an anticrossing as shown in the Raman spectra in Fig. 8 at ~5T. The Raman spectra were analyzed with an equation that describes the magneto-phonon exciton

and the phonon energy and half-width contributions to the resonance energy through the electron-phonon coupling strength (g). The equation used for the analysis is

$$\hbar\omega_{r\pm} = \frac{E_{Ph} + E_{ME}}{2} \pm \sqrt{(\frac{E_{Ph} - E_{ME}}{2})^2 + g^2} \tag{15}$$

The phonon contribution $E_{Ph} = \omega - i\gamma$ is comprised of the energy, (ω), and half width (γ) that can be extracted from the measurements. The same is true of the magneto-phonon exciton $E_{ME} = \Omega - i\Gamma$.

The anti-crossing was only visible on some areas of the kish graphite sample. One explanation is a large contribution to the Raman signal from decoupled graphene flakes. This can occur by turbostratic stacking which reduces the interaction between adjacent layers. Recently, MPR was also observed at high magnetic fields on monolayer graphene [34]. The transitions from $0 \longrightarrow 1$ were seen at ~25T using polarized light in samples with different filling factors, activating or blocking the inter-Landau level transitions [34].

2 STATE OF THE ART IN HYDROGEN STORAGE

The expanding worldwide energy consumption is quickly becoming a concern due to the limited quantity of fossil fuels, the basic source of energy. Predictions of when the supply of fossil fuels will be exhausted range from 40 years to 150 years [35], a relatively short time for developing and implementing an alternate source of energy. Aside from the practical issue of finite fossil fuels there are the detrimental environmental effects which put time constraints on the continued use of such forms of energy. Fossil fuels contribute to global warming since the combustion produces copious amounts of carbon dioxide, a greenhouse gas [35, 36]. Technological advances in developed countries along with ameliorating the quality of life in developing countries all require energy, magnifying the importance of such developments [36]. As a consequence, various forms of alternative energy such as solar, wind and biofuels are currently under exploration. These alternative energy forms, along with others, will most likely replace fossil fuels. The specific energy needs will dictate the choice of alternative energy. This chapter focuses on hydrogen as an energy vector. The positive aspects as well as the drawbacks of hydrogen related energy will be presented. The remainder of the chapter will focus on a central issue indispensable for the development of reliable hydrogen-based technology; the storage and transport of hydrogen. First the current state of the art methods and materials for hydrogen storage will be presented, followed by the advantages and disadvantages of using graphene as a scaffold for hydrogen storage.

2.1 TOWARDS A HYDROGEN BASED ENERGY TECHNOLOGY

2.1.1 *Hydrogen Production*

Hydrogen is an energy vector meaning that it can be used to store and transport energy [37]. It is not an energy source and although it is abundant in nature, it is mostly found in water which implies that to extract hydrogen, energy must be expended. One of the two main hurdles in the use of hydrogen is the process of producing pure hydrogen efficiently. This means that the production or extraction of hydrogen cannot succeed the specific energy capacity of hydrogen, 142MJ/kg. Specific energy capacity is a measure of the energy per weight of fuel [38]. One solution is to extract hydrogen via a renewable process such as wind, solar, tides, etc.

The production of hydrogen can be achieved by splitting water by electrolysis via any renewable energy source. One possible option is to emulate bacteria and microalgae which implement photochemical methods. They utilize adsorbed photons to oxidize water producing hydrogen as a by-product [36, 39]. There is no shortage of water available on the planet and by harnessing natural sources

of energy for separating hydrogen and oxygen, the hydrogen can then be used in fuel cells to provide energy with the only by-product being water.

2.1.2 *Energy Production by Fuel Cells*

Following the production of hydrogen, it is crucial to implement an efficient mode of storing it, which will be discussed at length after a short description on the consumption of hydrogen to produce electricity. The concept behind hydrogen fuel cells is the production of electricity by the catalyzed deprotonation of hydrogen [36]. The electrons are collected for electrical use before reuniting with the protons which have migrated across a polymer electrolyte membrane to combine with oxygen molecules forming water [36]. A schematic diagram is shown in Fig. 9. On the left, there is a hydrogen inlet connected to an anode with a catalyst such as Pt nanoparticles [36]. The catalyst separates the electrons which are carried through the anode, leaving the positive ions to move across the electrolyte membrane [36]. At the cathode, the electrons, protons, and oxygen combine forming water [36]. To economically mass produce hydrogen fuel cells, research on cheaper catalyst materials is essential.

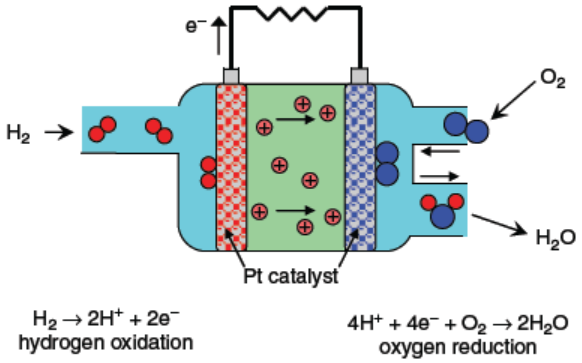

Figure 9: Diagram of a hydrogen fuel cell. Figure taken from reference [36].

Hydrogen has a remarkable energy capacity as compared to gasoline (46.4 MJ/kg), butane (49.1 MJ/kg), propane (49.6 MJ/kg), or diesel fuel (46.2 MJ/kg), further supporting a move towards a hydrogen based energy economy [40]. To provide a more concrete example, suppose a small car can go about 800km on a full tank (about 50L) of gasoline which weighs about 36.5kg [41], this corresponds to 11.9kg of hydrogen which at standard pressure and temperature is in a gaseous form that occupies 133 m^3! This is an enormous volume rendering hydrogen gas an impossible substitute for gasoline in spite of hydrogen's gravimetric energy density which is more than three times that of gasoline. The volume occupied by 11.9kg of liquid hydrogen is 0.17 m^3 but hydrogen is gaseous above -241°C [40]. The vacuum tanks designed for storage of liquid hydrogen are costly due to the 30% energy loss from the liquefaction process, the weight of the cryogenic tanks, and unavoidable loss of hydrogen due to boiloff [42]. BMW has developed a bi-fuel (gasoline and liquid hydrogen) luxury vehicle called the BMW Hydrogen 7 which has 100 cars in circulation that runs on liquid hydrogen in a vacuum tank, a dangerous and expensive choice

for storing hydrogen as demonstrated by the small output of vehicles [43]. One of the main branches of cutting edge research is focused on innovative ways of storing hydrogen.

The high energy capacity and the lack of environmental impact are two cardinal advantages for using hydrogen as an energy vector. Notably, every step of the hydrogen energy cycle must be optimized in order to practically use hydrogen as a cheap, renewable, carbon-free energy source starting from the production of hydrogen, to the storage of the extracted product, to the efficiency of the fuel cells used to produce electricity.

The focus of this chapter is on the storage of hydrogen, a key challenge in a hydrogen based economy. The evaluation of plausible methods of hydrogen storage will be discussed in a framework that provides clear numerical values to characterize the hydrogen storage efficiency, specifically, the gravimetric density and the volumetric density of the hydrogen system. The gravimetric density is the percentage of weight from hydrogen with respect to the total combined weight of the hydrogen and storage material [37]. The volumetric capacity is a measure of the hydrogen mass contained in a unit volume of the storage material [37].

The United States Department of Energy (DoE) is providing extensive funding for hydrogen storage research and has set standards that have become universal in the evaluation of materials. The standards set for 2017 are a gravimetric capacity of 5.5wt% (0.055 kg $H_2/kg_{systemtotal}$) of usable hydrogen and a volumetric capacity of 4% (0.04 kg $H_2/L_{systemtotal}$) [44]. The ultimate goals are 7.5wt% and 7.0%, respectively, for use in vehicles [44]. To comply with safety, the range of temperatures for the hydrogen release is restricted to -40°C to 85°C. The matrix used for storing hydrogen is expected to be reusable and perform a minimum of 1500 cycles of hydrogen release. Lastly, for practical use, a tank with a hydrogen capacity of 5kg is expected to be filled in 3.3 min. These are steep standards when compared to the current state of the art hydrogen storage technology.

2.2 STATE OF THE ART IN HYDROGEN STORAGE MATERIALS

2.2.1 *High Pressure Tanks*

As mentioned above, liquid hydrogen stored in cryo-compressed hydrogen tanks is one viable option [45]. A prototype known as the Gen-3 cryo-compressed carbon fiber reinforced tank was constructed [45]. The gravimetric and volumetric standards set by the DoE for 2017 are met by the Gen-3 cryo-compressed tank, 5.5wt%, and 4.18%, respectively. However, it is crucial to consider the energetic cost of hydrogen liquefaction and the total cost of the cryo-compressed tank which is elevated due to the composite material and the labor intensive manufacturing process [45].

Carbon fiber reinforced high pressure tanks can also be utilized for compressed hydrogen gas storage. The gas container can withstand 5000-10000psi

(345-689bar) [46, 47] and it is equipt with an external impact resistant shell for enhanced safety. The drawback of this storage method, as in the case of liquid hydrogen storage, is the cost of the carbon fiber composite material in addition to the large volume. The hydrogen volume can be reduced by cooling the compressed gas but liquid nitrogen cryo-compressed tanks have added weight, volume and cost due to cooling [47]. The development of high pressure canisters is ongoing, pursuing two crucial aspects, the material expenses along with safety.

2.2.2 *Hydrogen Storage in Solids*

Hydrogen can be stored in solid materials by either chemisorption or physisorption, the difference being the strength of the interaction between the hydrogen atom or molecule and the storage medium. Chemisorption is characterized by a strong bond that typically requires high temperatures (>100°C) to break, placing these types of materials outside of the standards set by the DoE, unless the desorption and adsorption barriers can be significantly reduced. On the other hand, physisorption is a weaker interaction and often requires cooling of the storage medium to increase the strength of the interaction. In the following sections we discuss the most relevant forms of hydrogen storage.

2.2.3 *Metal Hydrides*

Metal hydrides form when hydrogen atoms diffuse through a metal lattice forming a hydrogen sublattice [42]. There are a number of metal hydrides that comply and in some cases even surpass the gravimetric standards set by the DoE, yet there are hurdles that must be overcome. One issue involves the diffusion of hydrogen throughout the lattice which is determined by the metal-hydrogen bonding. In the case of transition metals, the hydrogen can partially donate its electron to the lattice leaving the proton to migrate through the crystal [42]. However, when hydrogen atoms bond covalently or ionically, the diffusion is impeded and the hydrogen atoms remain mainly at the surface of the metal lattice [42]. A practical solution is replacing bulk metals with nanoparticles, however, when the hydrogen-metal bonds are covalent or ionic, the hydride is stable, consequently, the energy required to release the hydrogen is extremely high. One such example is the lithium imide system starting from ballmilling lithium amide and lithium hydride where the hydrogen desorbs at 700°C [42]. Furthermore, a viable metal hydride must exhibit low heat dissipation during formation, fast kinetics, and resist degradation, retaining its properties over numerous dehydration/rehydration cycles [48].

A number of light weight metals have been considered for hydrogen storage with the inclusion of heavier catalytic elements that modify the formation, release or kinetic properties of the compound [48]. A few examples will be presented that touch on the gamut of metal hydride compounds explored over the years as possible solutions for hydrogen storage.

$NaBH_4$ is a promising material on account of its stability in air, formidable hydrogen uptake, 10.8wt%, and the advantage of a one step release mecha-

nism [49]. One drawback is the release of hydrogen takes place at temperatures above 500°C causing melting and decomposition of the compound making the process irreversible [49]. Reversibility is an essential quality in developing a sustainable alternate source of energy [49]. By creating core-shell nanoparticles with $NaBH_4$ covered by Ni which shields the core from melting due to the high melting temperature of Ni with respect to $NaBH_4$, the process becomes reversible [49]. However, the hydrogen weight percent is reduced to 5wt%, below the standards set by the DoE [49]. Furthermore, the absorption and desorption processes are slow (full absorption takes 5 hours) and require high temperatures (350°C) and elevated pressure (4MPa) [49]. These results published in 2012, are an indication of the state of the art of metal hydride materials illustrating the shortcomings regarding every standard set by the DoE demonstrating areas for significant improvement.

Magnesium is another commonly used element since the formation of the compound MgH_2 has a high gravimetric density (7.6wt%) [50, 51] and the cost of the material is low. A fundamental problem associated with magnesium stems from the thermodynamic stability of the hydride, consequently, the temperature required for releasing the hydrogen is approximately 400°C [50]. Furthermore, the kinetics of absorption is slowed by the formation of an oxide on the surface when not in an oxygen-free environment [48, 50]. A process known as ball-milling in which large surface areas are exposed by grinding the metal or metal compound to form nanocrystals, has been implemented with positive results: lowering the desorption temperature, increasing the surface area and therefore the speed of absorption of hydrogen. Nonetheless, the results do not meet the standards set by the DoE. In a recent study published in Nature Materials, Mg nanocrystals with a diameter of approximately 5nm were embedded in PMMA which acts as a sieve [52]. It is permeable to hydrogen and a barrier to oxygen, preventing the formation of oxide on the surface of the Mg nanocrystals that hinders the hydrogen uptake and release [52]. The composite formed from Mg nanocrystals in PMMA could absorb up to 4wt% hydrogen, when considering the entire composite mass [52]. The size of the nanocrystals and the selective permeability capacity of the polymer decrease the hydrogen absorption time to approximately 30 minutes at 200°C and a H_2 pressure of 35mbar while simultaneously stabilizing the composite in air [52]. The hydrogen absorption and release can be repeated about three times before the material begins to degrade reducing the efficiency [52]. These results are a notable improvement over Mg composite metal hydrides yet none of the standards set by the Department of Energy have been reached.

2.2.4 *Metal Organic Framework*

Another possibility for storing hydrogen are metal organic frameworks, a network of metal atoms bound to organic molecular chains, (metal-ligand bonds), forming a porous structure capable of adsorbing molecular hydrogen, predominantly via physisorption [53]. The weak van der Waals forces responsible for the hydrogen adsorption can be tuned by controlling the pore size. The drawbacks of metal organic frameworks are the low hydrogen binding energy and

the large volume. The former indicates that the hydrogen gravimetric capacity is enhanced by cooling the system to cryogenic temperatures which is both costly and increases the total weight of the combined storage system when considering the extra weight and volume required for cooling. The large volume is an intrinsic property of metal organic frameworks which stems from the large surface areas necessary for molecular hydrogen physisorption.

An example of one of the highest performing metal organic frameworks is $Zn_4O(BDC)_3$, an extended cubic structure formed with zinc based clusters bound to six organic linkers creating a porous periodic scaffold. It displays high surface area where hydrogen molecules interact strongly with the zinc vertices and weakly with the linkers [54, 55]. The 12 Å pore-diameter framework adsorbs 4.5wt% at 78K and 1bar but the physisorption properties dramatically decrease at room temperature requiring a moderate pressure of 20bar to achieve 1wt% [54, 56]. The gravimetric capacity does not satisfy the standard set by the DoE.

2.2.5 *Carbon-Based Materials*

A plethora of research has been dedicated to studying carbon-based materials for hydrogen storage. Initially fullerenes were considered due to their large hydrogen uptake which reached a gravimetric capacity of greater than 6wt% [57]. Unfortunately the hydrogenation time was 30 minutes at both elevated temperature and pressure, 400psi (28bar) and 180°C, respectively, well outside of the constraints set by the DoE [57]. Various catalysts were tested to reduce the temperature of hydrogenation and dehydrogenation but the DoE standards have not been obtained.

Soon after, carbon nanotubes captured the spot light and have been an area of ongoing study. Despite the advancements over the years carbon nanotubes are far from displaying advantageous qualities for hydrogen storage. Pristine bundled multiwall carbon nanotubes have a hydrogen gravimetric density of 0.52wt% which can be increased to 2.7wt% with the creation of nanopores and defects subsequently decorated with Pt nano particles, a costly catalyst [58]. This is still well below the gravimetric density of 5.5wt%, the DoE target for 2017.

2.2.6 *Why Graphene?*

Recently, there has been a renewed interest in carbon-based materials for hydrogen storage thanks to graphene. Graphene has taken center stage in the field of hydrogen storage due to the high surface area and vast possibilities of chemical functionalization. Furthermore, the predicted theoretical gravimetric densities range from 5wt% to 8wt% [37], well above the standards set for 2017 [44]. The adsorption of hydrogen on graphene can be separated into two categories: physisorption and chemisorption. Physisorption is mediated by weak interactions such as van der Waals forces between molecular hydrogen and graphene. Chemisorption is characterized by a chemical bond between hydrogen atoms and graphene.

2.2.7 *Physisorption*

Graphene was first considered an auspicious material for hydrogen storage in 2005 with the publication of a DFT study focused on creating a hydrogen nano pump by mediating the interlayer spacing to maximize the molecular hydrogen intake [59]. The theoretical results for the graphene nanopump did not comply with the standards set by the DoE, nonetheless, they provoked an interest in pursuing graphene as a potential material for hydrogen storage. It spurred many theoretical proposals for chemically modifying the graphene surface with various transition metals [60, 61, 62, 63, 64, 65, 66] to increase the interaction of molecular hydrogen and graphene.

2.2.8 *Chemisorption*

In 2007, a theoretical study predicted the stability of chemically bonding atomic hydrogen to graphene [67]. However, the decisive spark came in 2009 when graphane, hydrogen-passivated graphene, was first demonstrated [2]. Graphane is graphene with atomic hydrogen chemically bonded to each carbon atom in the graphene lattice which translates to a gravimetric density of 8wt%, well above the standards set for 2017 [2]. Furthermore, a unique advantage of graphene is the possibility of exploiting its flexibility to control the uptake and release of hydrogen at room temperature and pressure [3].

The experimental work presented in this thesis focuses on demonstrating the interaction between atomic hydrogen and graphene and secondly, the role of curvature in mediating the interaction. Initially, research was aimed at identifying a suitable graphene system characterized by possessing curvature on a local scale [3]. Chapter 3 describes the growth process used to produce various types of graphene: monolayer graphene grown on SiC(0001), the buffer layer (described in chapter 3), and quasi-free-standing monolayer graphene (details found in chapter 3). The three surfaces were characterized by Raman spectroscopy and scanning tunneling microscopy. We were able to acquire atomic resolution images of the surfaces and analyze the image profiles to select an ideally curved surface. We selected monolayer graphene grown on the silicon face of silicon carbide for studying the interaction of hydrogen and graphene. In chapter 4 the results of exposing the monolayer graphene to atomic hydrogen are presented. We were able to achieve atomic resolution images after hydrogenation and identify the stable hydrogen conformations which we compared to DFT calculations carried out at NEST. The most important observation was that the hydrogen preferentially chemisorbed on the convex areas of the graphene surface. The hydrogen attached to the most severely curved areas were stable up to ~650°C at which point the chemical bond was broken. The graphene remained intact and the process was repeated a few times. These results agree with theory and are a starting point for creating graphene based hydrogen storage devices that rely on curvature alone for the adsorption and desorption of hydrogen on graphene [3].

3 GRAPHENE GROWTH AND CHARACTERIZATION

The focus of this chapter is to explain how carbon-rich layers such as graphene can be produced from silicon carbide. A brief description of the growth process is presented followed by a section on the characterization techniques employed in identifying and evaluating the quality of the graphitic layers produced. In the last section these methods will be exploited to characterize the samples. These samples are studied in the following chapter to understand the interaction of hydrogen chemisorption on graphene.

3.1 CRYSTAL STRUCTURE OF SILICON CARBIDE

Silicon carbide (SiC) is a crystal formed from silicon and carbon atoms which in its most common form has a layered hexagonal structure. The basic unit is a tetrahedral structure as seen in Fig. 10, where the silicon atom is bonded to four carbon atoms and vice versa. The silicon carbon bond length is 0.189 nm and the in plane crystal structure is hexagonal with a lattice constant a = 0.308 nm. This silicon-carbon plane is called a bilayer. Bilayers can be stacked in numerous sequences but the three main polytypes of silicon carbide are 3C, 4H, and 6H. The number of bilayers in the stacking sequence is given by the number in front of the letter. The letters used to identify the silicon carbide polytype are related to the crystalline structure, hexagonal (H) or cubic (C), which describe the atoms as seen from above when the lattice is cut along the (0001) plane. The cubic structure is comprised of two interpenetrating face-centered cubic lattices with the tetrahedral basis described above. The bottom part of Fig. 10 shows the bilayer stacking sequences for the polytypes 3C, 4H, and 6H.

The most common polytypes used for producing graphene are 4H and 6H. Graphene can be grown on both the silicon face, SiC(0001) and the carbon face, SiC($000\bar{1}$) [68, 69, 70]. The number of layers of graphene grown on the carbon face is difficult to control since the growth process is fast. The graphene layers do not grow in a well defined staking sequence but turbostratically [69].

On the other hand, the stacking order and the number of layers grown on the silicon face can be controlled precisely by optimizing the growth temperature, time and growth chamber pressure [68, 70]. The graphene grown on the silicon face is corrugated with a periodicity given by the interaction with the surface below [71, 72]. The samples used in this thesis were grown on the silicon face in order to exploit the expected corrugation to study the interaction of hydrogen with graphene as a function of curvature.

3.2 GROWTH ON SILICON CARBIDE

The growth of graphene on SiC is a two-step process starting with hydrogen etching to remove the scratches on the surface. Large terraces form on the sur-

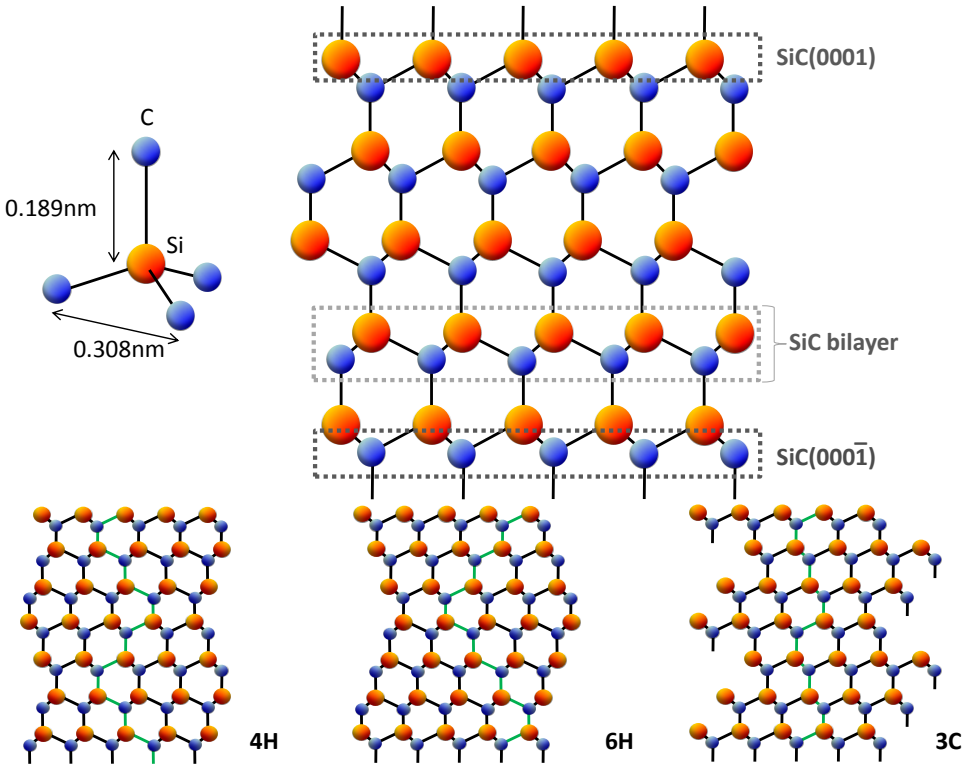

Figure 10: Silicon carbide crystal structure. The tetrahedral structure is shown on the left. The large orange circles are Si and the small blue balls are C. A diagram of the SiC crystal bilayer stacking is on the right. The three stacking sequences from left to right are 4H, 6H, and 3C.

face because the crystal is not cut directly along the plane (0001) which means that multiple bilayers are cut across. The angle off the plane (0001) determines the size of the terraces. The hydrogen etching process removes the scratches and only the terraces remain. The graphene growth process starts at the terrace edges better known as step edges [68, 70]. The second step is graphene growth in which the crystal is heated to high temperatures and the silicon sublimates leaving excess carbon on the surface which reassembles to form a carbon layer [68, 70]. The first carbon layer that forms during the growth process on the silicon face is called the buffer, interface, or zero layer. This is a carbon layer in the same topological configuration as graphene. The carbon atoms, however, bond to the SiC reconstruction below when the two lattices are in register [71]. The SiC lattice has a lattice constant of 3.08 Å and graphene has a lattice constant of 2.46 Å [71]. The super periodicity due to the buffer layer's interaction with the SiC reconstruction is called the $(6\sqrt{3}\text{x}6\sqrt{3})\text{R}30°$ and the length of the unit cell is 32 Å [71]. This is equivalent to 13 graphene hexagons. $6\sqrt{3}$ is the number of SiC lattice units that have the same length as 13 graphene rings. It is considered the true periodicity of the graphene that grows on the silicon face and has been experimentally observed by x-ray diffraction, low energy electron diffraction, and scanning tunneling microscopy [72, 73]. However, often the simple quasi-(6x6) periodicity is observed by scanning tunneling microscopy which gives rise to a unit cell of about 20 Å [72, 73]. The reason for this discrepancy is not well understood. The peak to peak corrugation of the buffer layer is theoretically predicted to be 1.2 Å [71].

The bonding between carbon atoms in the buffer layer lattice with the silicon atoms in the lattice below cause a periodic corrugation. The carbon atoms are pulled towards the silicon atoms where there is an sp^3 bond (See bottom part of Fig. 11). Figure 11 also shows a theoretical calculation of the buffer layer. The plot displays the two unit cells (the $(6\sqrt{3}\text{x}6\sqrt{3})\text{R}30°$ (dashed diamond) and quasi-(6x6) (solid diamond)).

Growth on the silicon face is a process that takes place from the inside out [74]. This means that the first layer that forms is the buffer layer. This layer forms after three bilayers of silicon desorb from the crystal. The carbon atoms that remain can form a single layer of carbon atoms in the topological arrangement of graphene, i.e. the buffer layer (Fig. 12a). If the crystal is heated to a higher temperature, more silicon atoms sublimate out of the crystal and the remaining carbon atoms form a new buffer layer below the first buffer layer. The previous buffer layer becomes the first graphene layer and the carbon layer formed underneath is bonded to the substrate with the $(6\sqrt{3}\text{x}6\sqrt{3})\text{R}30°$ periodicity (Fig. 12b). The monolayer of graphene is situated on top of the corrugated buffer layer so it shows the same long range periodicity but the corrugation is lower, about 0.4 Å (Fig. 13) [71].

Graphene growth was initially performed in ultra high vacuum which led to very inhomogeneous and low quality graphene samples. The surface morphology was dramatically improved by growing graphene in an argon atmosphere at atmospheric pressure [68]. The increased pressure in an inert atmosphere reduces the rate of silicon desorption. This allows the growth process to take place at higher temperature, providing excess kinetic energy for the carbon atoms left on the surface to reorganize into a uniform layer.

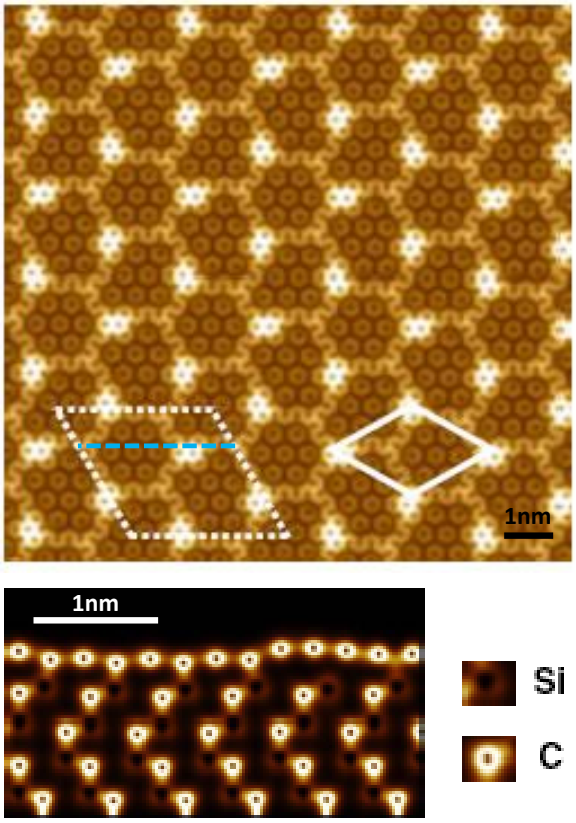

Figure 11: The charge-density map of the buffer layer on SiC(0001) is shown on top. The $(6\sqrt{3}\text{x}6\sqrt{3})\text{R}30^\circ$ (dashed diamond) and quasi-(6x6) (solid diamond) are indicated. The cross-section below was taken along the green dashed line. The figure is from ref. [71].

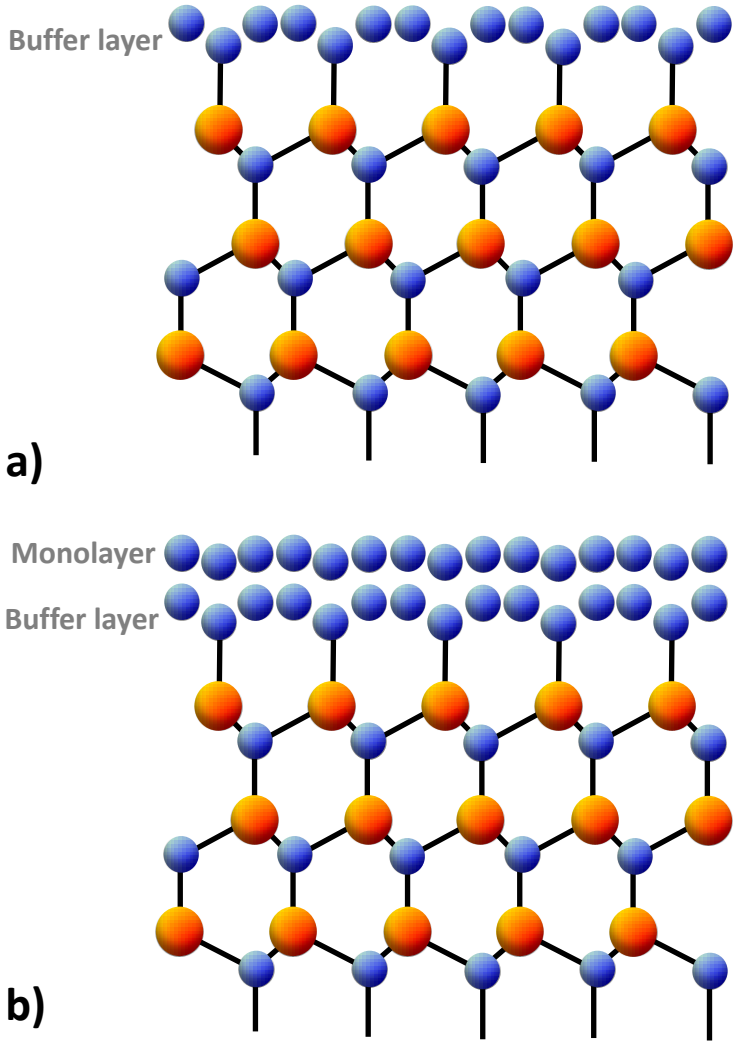

Figure 12: a) A diagram of the buffer layer with bonds to the SiC reconstruction below. b) A diagram showing the monolayer on top of the buffer layer.

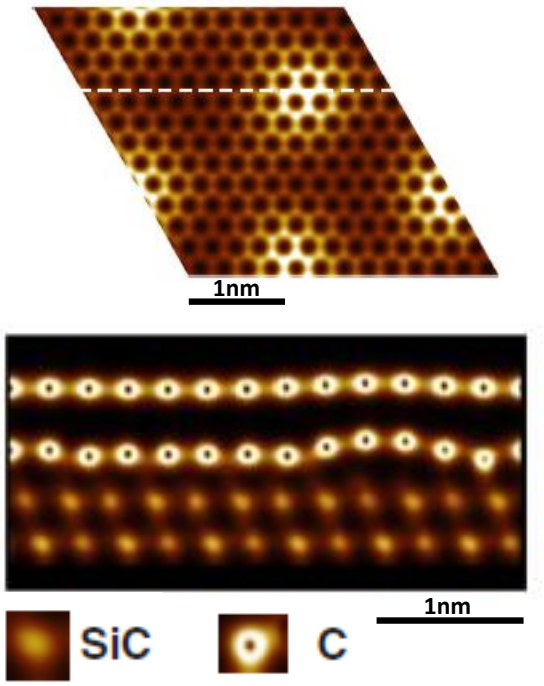

Figure 13: The charge-density map of monolayer graphene on SiC(0001) is shown on top. The cross-section below was taken along the white dashed line. The figure is from ref. [71].

Therefore, growth of graphene is now typically performed in chemical vapor deposition (CVD) systems in an inert argon atmosphere. The growth system installed at NEST (Fig. 14) is a prototype system designed by Aixtron. It is a vertical CVD reactor with direct heating via a graphite heater. The sample is placed on top of the graphite heater and a current is passed through the graphite, heating it to the desired temperature, measured by an infrared sensor. The process gases are let into the growth chamber above the sample. Although the system is different, the growth concept is the same as in a classic CVD system. Our preliminary results from the Aixtron prototype system will be presented to demonstrate the different samples that can be produced and the methods implemented to characterize the samples. The samples used for the hydrogen adsorption experiments were produced with optimized growth processes in a classical CVD system and the description of these samples follows.

3.2.1 *Hydrogen Etching Process*

Commercially produced and polished 6H silicon carbide wafers were the starting material for all the samples produced at NEST. However, even polished wafers have scratches on the surface (see Fig. 15) which need to be removed to create an atomically flat surface. To remove the scratches, the silicon carbide wafers are heated to 1500°C in an argon-hydrogen atmosphere at 450 mbar. The silicon on the surface evaporates and the hydrogen molecules crack on the surface of the SiC crystal forming hydrocarbons which are volatile and carried away. After 5 minutes of hydrogen etching the scratches are removed leaving an

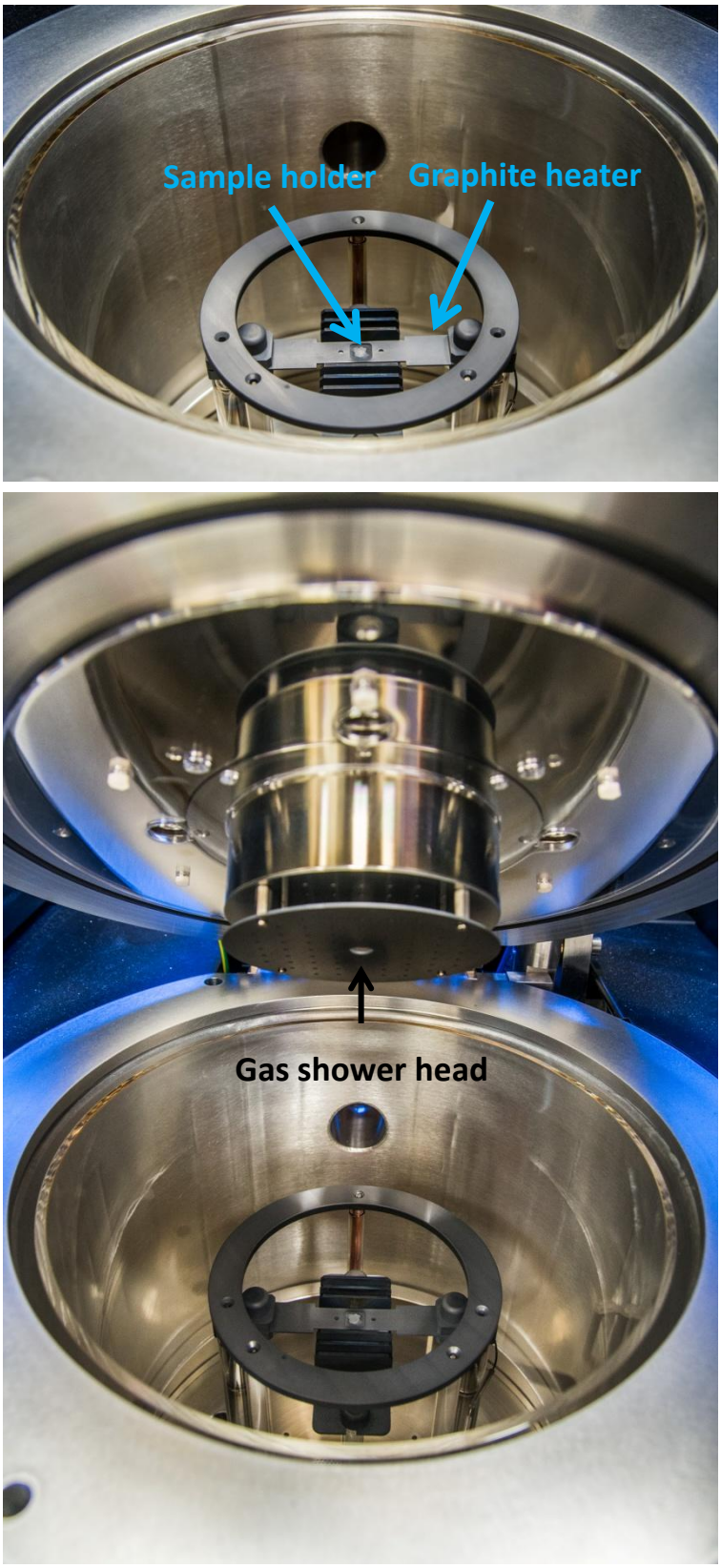

Figure 14: The top photograph is the prototype CVD by Aixtron. The growth chamber is seen from above with the graphite heater. The sample's position during growth is also labeled. The bottom photograph shows the CVD with the top partially closed to show the shower head where the process gases enter.

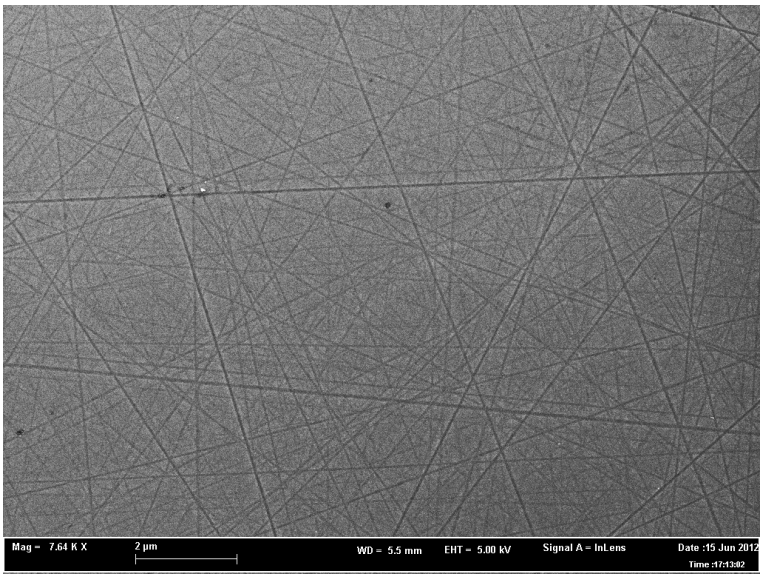

Figure 15: SEM image of scratches on a pristine SiC(0001) surface.

atomically flat surface with steps (Fig. 16). The steps result from the inability to cut the silicon carbide crystal exactly along the crystallographic axis SiC[0001]. The small angle off the crystallographic axis means that multiple atomic planes are cut through and form steps.

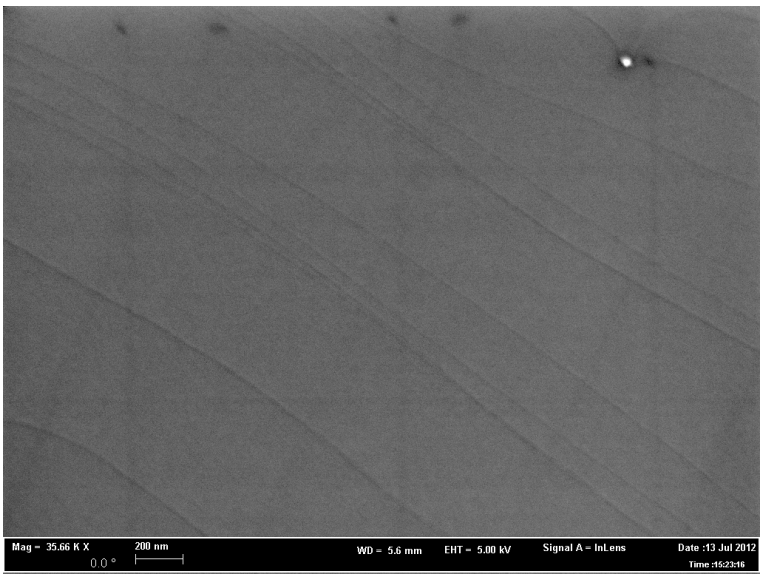

Figure 16: SEM image of atomic steps on SiC(0001) after hydrogen etching.

3.2.2 *Growth Process*

Once the SiC(0001) surface is atomically flat, uniform carbon layers can be grown on the surface. The growth process initiates at the step edge when the sample is heated to 1550°C (buffer layer) or 1600°C (monolayer graphene) for 12 minutes (buffer layer) or 10 minutes (monolayer graphene). The growth occurs in an argon atmosphere of 790 mbar for the buffer layer and 750 mbar

for monolayer graphene. These parameters are system dependent. The high pressure slows the growth by preventing sublimation of the silicon, while at the same time it permits the growth to take place at a higher temperature [68]. When three layers of silicon sublimate from the surface, there are enough carbon atoms to create a single layer of graphene. The high temperature supplies additional kinetic energy to the carbon atoms allowing them to migrate along the surface and create large areas of uniform, high quality graphene.

3.2.3 *Hydrogen Intercalation*

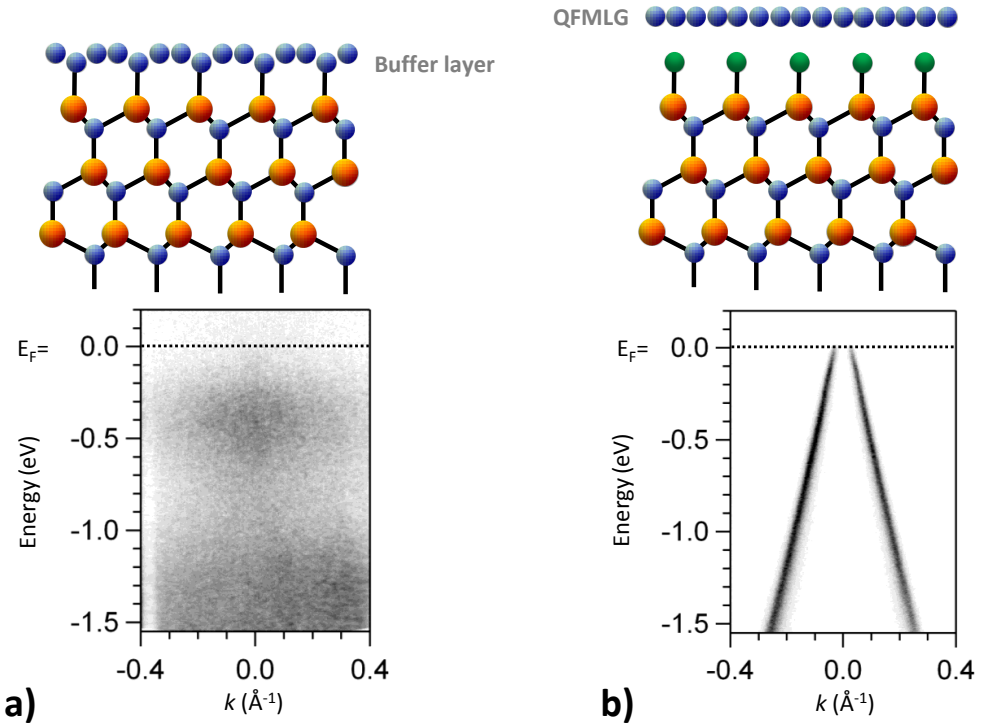

Figure 17: a) ARPES measurements of a buffer layer. b) ARPES measurements of quasi-free-standing monolayer graphene (QFMLG) showing the π-bands of graphene after hydrogen intercalation. The dark color indicates high intensity meaning areas where there are electronic states. The white areas are where there are no states. Diagrams of the buffer layer and QFMLG are above the ARPES measurements. The blue circles are carbon atoms. The orange circles are silicon atoms. The green circles are hydrogen atoms. ARPES measurements courtesy of Dr. Camilla Coletti (IIT, NEST Pisa).

Hydrogen intercalation is a process that allows for breaking the silicon-carbon bonds between the buffer layer and the SiC reconstruction below. The silicon dangling bonds are passivated with atomic hydrogen, forming silicon-hydrogen bonds. The intercalation process is performed at elevated temperatures, 600°C to 1000°C, in a pure molecular hydrogen atmosphere at atmospheric pressure [75]. The molecular hydrogen bond cracks on the surface forming atomic hydrogen. On flat graphene, hydrogen-carbon bonds are unstable above about 450°C [2]. The intercalation process was performed above

this temperature to minimize the possibility of forming hydrogen-carbon bonds while providing optimal conditions for breaking the silicon-carbon bonds and forming silicon-hydrogen bonds. The process of hydrogen intercalation can restore the graphene band structure to the buffer layer as demonstrated in Fig. 17. Angle-resolved photoemission spectroscopy (ARPES) measurements manifest the electronic band structure of a material. The ARPES measurements on the buffer layer before hydrogen intercalation show two delocalized states at energy values below the Fermi level of around -0.2 eV to -0.6 eV and then below -1.0 eV [75]. These delocalized states are a result of the periodic bonding of the carbon atoms in the buffer layer to the SiC surface below [75]. These states are replaced by the characteristic π-bands of graphene after hydrogen intercalation [75]. Graphene formed by hydrogen intercalation is known as quasi-free-standing monolayer graphene (QFMLG).

3.3 TECHNIQUES FOR SAMPLE CHARACTERIZATION

The methods typically used for characterizing graphene samples are Raman spectroscopy, scanning electron microscopy (SEM), ARPES, and x-ray photoelectron spectroscopy (XPS). Raman spectroscopy is useful for identifying how many layers of graphene have been grown and is widely used as a reliable method for characterizing graphene. SEM can provide topological information on the growth uniformity and if the growth is initiating at the step edge. Remarkably, SEM images provide a clear contrast between single layers. However, identifying whether the layer is the buffer layer, monolayer or bilayer from SEM measurements alone is not possible. ARPES can be used to reproduce the filled electronic bands. XPS uses the photoelectric effect to extract information on the chemical composition of a surface by analyzing a set of well defined peaks in a photoelectron spectrum. One drawback of this technique is that it cannot directly detect hydrogen. The work presented in this thesis is focused on the interaction of hydrogen and graphene at an atomic scale making the best method of characterization scanning tunneling microscopy (STM). STM is a technique that can provide atomic resolution images of a surface. The quality of the graphene lattice can be evaluated. Furthermore, the long range periodicity can be observed and the corrugation can be measured. Once these pristine surfaces have been characterized, they can be exposed to atomic hydrogen. The positions of the hydrogen atoms can be distinguished on the graphene lattice, making STM an extremely valuable method for probing this system. The most relevant approaches for characterizing the samples, keeping in mind the aim of this thesis, are micro-Raman spectroscopy and STM which will be presented in the following sections.

3.3.1 *Raman Spectroscopy: Setup*

Spatially-resolved Raman spectroscopy was performed at room temperature in air. The 488 nm line of an Argon laser was focused by a 100x objective lens on the sample with a spot diameter of 350 nm. The backscattered light was collected by a single-grating spectrometer onto a Peltier-cooled CCD. An off-axis

CCD camera was used to select the laser position. Piezoelectric micrometers on the sample stage provide precise positioning and focusing of the laser on the sample and can be programmed to collect Raman spectra maps on a user defined grid.

3.3.2 *STM Theory*

Scanning tunneling microscopy (STM) was first achieved in 1981 by Gerd Binnig and Heinrich Rohrer and its novelty led to the Nobel Prize in 1986 [76]. The concept is to create a map of the density of states of a surface at a given energy using the tunneling of electrons. The resolution of these maps is routinely on the atomic scale so in a very naive picture, the STM provides an image of the positions of the atoms on a surface.

The basic concept behind STM is electron tunneling from (to) a sharp metallic tip to (from) a conducting surface directly below the tip. By raster scanning the tip across the surface and recording one of two parameters, tunneling current, I, or distance, d, between the sample and the tip, an image is created. In the case that the tunneling current is recorded, the bias voltage, i.e. the difference in voltage between the tip and the sample, and the distance of the tip from the sample, selected at the beginning of the scan, are held constant. A map is created where the topography is given by the tunneling current. These types of images are taken in the constant height mode. A more common technique used to image a surface via STM is known as the constant current mode. The tunneling current is held constant by a feedback mechanism which changes the tunneling junction distance, d, to maintain a constant current. The resulting image is a topographic map of the density of states of the surface at a given energy defined by the bias voltage. All the images shown in this thesis were obtained using this method.

The first theory of STM tunneling presented in 1983 is a simplified model of how atomic resolution is achieved [77]. The full theory related to tunneling and atomic resolution is more profound and complex and should include the wave function of the tip. The results presented in 1983 clarify some of the basic concepts and are presented below. In the model, the tip apex is approximated as spherical with a radius R. The first important result is that tunneling and therefore the tunneling conductance, σ, depends exponentially on the tip and sample distance in agreement with quantum mechanics [77]. The tunneling of an electron can be described quantum mechanically using the Schrödinger equation. The electron wavefunction is found to exponentially decay in a barrier and the probability density of detecting the electron at a given point is the square of the wavefunction [78]. In STM, the bias voltage applied to induce tunneling is considerably smaller than the work function, the energy need to expel the electron to the vacuum [78]. If the tunneling current is defined as the sum of the all electrons tunneling from the tip to the sample and the density of states of the tip and sample are assumed to be constant, the tunneling is proportional to [77, 78]:

$$\sigma \propto e^{-2\kappa d} \tag{16}$$

In the above equation κ is the inverse of the wavefunction decay length, and d is the vacuum gap between the tip and the sample. Typically d is on the order of 10 Å and the tunneling current decreases by one order of magnitude with a distance increase of 1 Å. This explains why tunneling occurs from the last atom or formation of atoms at the tip.

A more elaborate result of the tunneling current was provided by Bardeen's formalism [79]. To a first order approximation, the tunneling current is given by [80]:

$$I = \frac{2\pi e}{\hbar} \sum_{\mu,\nu} f(E_\mu)[1 - f(E_\nu + eV)]|M_{\mu\nu}|^2 \delta(E_\mu - E_\nu) \tag{17}$$

where $f(E)$ is the Fermi function, $M_{\mu\nu}$ is the tunneling matrix between the tip states and the sample states and V is the bias voltage applied between the tip and sample. ν designates the sample and μ, the tip. Calculating the tunneling matrix elements $M_{\mu\nu}$ is a formidable problem that should account for the detailed electronic structure of the tip and the surface. Despite these details, the meaning of the equation is that the tunneling current is the sum of all the tunneling events between the occupied states, $f(E_\mu)$, of the tip and the unoccupied surface states in the energy range of E_ν to $E_\nu + eV$. If the bias voltage polarity is reversed, then the occupied and unoccupied states as defined above are inverted.

In reality calculating the tunneling current is an extremely complex function when the electronic structure and form of the tip are brought into consideration. The tips are often made of tungsten, as is the case here, and the transition metal's d_{z^2} states on the surface form sharp dangling bonds that allow for the high lateral and vertical resolution in STM [81].

3.3.3 *Scanning Tunneling Spectroscopy Theory*

The tunneling current as defined in the equation above (17) can be written in another form as follows [82]:

$$I = \frac{4\pi e}{\hbar} \int_0^{eV} |M_{\mu\nu}|^2 \rho_\mu(E_F - eV + \epsilon)\rho_\nu(E_F + \epsilon)\delta\epsilon. \tag{18}$$

This equation has a few important assumptions. The bias voltage is assumed to be small and the Fermi functions have been replaced with step functions which imply a sharp cutoff at E_F between the filled and empty states. ρ is the density of states of the sample or tip. The tunneling current equation can be further simplified by considering the matrix elements to be nearly constant in the range of values measured [79]. The equation is then simplified to:

$$I \propto \int_0^{eV} \rho_\mu(E_F - eV + \epsilon)\rho_\nu(E_F + \epsilon)\delta\epsilon. \tag{19}$$

The tunneling current is proportional to the density of states of the sample and the tip [82]. If the density of states of the tip is constant then the current is

proportional to the density of states of the sample at a given voltage V. By taking the derivative of the current as a function of voltage, the sample density of states can be recovered. In other words, if the current is recorded at a given position over a range of voltages (I/V curves) and the derivative is taken (dI/dV) and plotted as a function of V, the graph is proportional to the density of states. These types of measurements are known as scanning tunneling spectroscopy (STS).

To measure the true density of states, the dI/dV curve should be normalized by I/V. This removes the tip-sample distance dependence that can change the form of the I/V curves [83].

3.3.4 *Tip Etching*

The dc electrochemical tip etching electronics and apparatus were homebuilt using the model from J. P. Ibe et al [84]. The tips were etched from tungsten wire. The electrochemical reaction occurs at the junction between the air and the basic solution [84, 85].

An electrical potential is applied between the tungsten wire (anode) immerged in a 2M NaOH solution and a gold ring (cathode) at the meniscus of the liquid surface. A positive voltage applied at the tungsten wire oxidizes at the liquid surface and forms WO_4^{2-} [84]. The cathode reduces the water to form OH^- and H_2 gas [84].

The oxidation reaction causes the wire emerged in the solution to loose mass, predominately at the interface between the liquid and the air. As the wire thins, the voltage drop across the anode-electrolyte-cathode interface increases and the current decreases. Once the wire breaks, the resistance between the anode and the cathode dramatically increases and the current drops to nearly zero. To make sharp tips, the electrochemical reaction must stop when the wire breaks, otherwise the etching will continue and dull the tip. The home built electronics stops the etching process at precisely this point.

Optimizing the etching process resulted in tips with a diameter of less than 20 nm when measured by scanning electron microscopy (SEM). Figure 18 is an SEM image of a tip etched with this setup. The optimal parameters obtained were a 0.25 mm diameter tungsten wire with a length of 1.5 cm. 3 mm of the wire were submerged in the 2M NaOH solution with a cutoff voltage to stop the etching reaction of 2.7 V and a starting voltage difference of 4 V. The average etching time was 8 to 10 minutes. The freshly etched tip is then cleaned with DI water, acetone, and isopropanol.

3.3.5 *In Situ Tip Preparation*

The tips are then brought into the STM ultra high vacuum chamber. The electrochemical etching process leaves an insulating layer of tungsten oxide (WO_3) on the surface of the tips, which must be removed to attain a stable tunneling junction [85]. The tips are subsequently placed on a tip preparation tool, which consists of a filament at a fixed distance from the tip with contacts to apply a voltage difference between the tip and the filament.

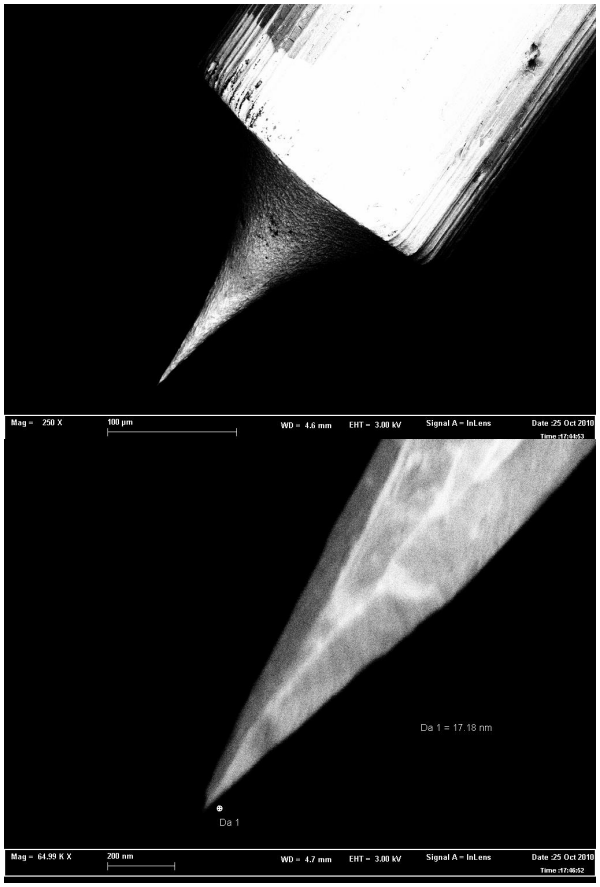

Figure 18: Scanning electron microscope image of a tip. The lower panel is a close up of the tip. The circle (with a diameter of ~17 nm) next to the tip can be used to discern how sharp the tip is. Tips like this give atomic resolution.

The tips are degassed overnight by running a current through the filament, which anneals the tips without deforming them. Following the degas, the oxide is removed by bombarding the tip with electrons emitted from the filament. A voltage difference of 600 V is applied between the tip (positive) and the filament (negative). The current through the filament is quickly increased until the emission current measured at the tip is 10 μA. This removes the oxide without blunting of the tip.

These tips are now stable and ready for use for STM and STS measurements.

3.3.6 *STM Setup*

The STM we set up is a variable temperature ultra high vacuum STM from RHK Technologies (Fig. 19). Images can be acquired from temperatures down to 100K and up to 1500K. The UHV system is comprised of three chambers. The smallest is the load lock which is used for loading and removing samples and tips without bringing the entire STM system to atmospheric pressure. The load lock can be pumped down to $\sim 1 \times 10^{-8}$ mbar by a turbo pump backed by a scroll pump in approximately 8 hours. Once this pressure is reached, the sample or tip can be moved into the preparation chamber ($\sim 1 \times 10^{-10}$ mbar) or the STM chamber ($\sim 5 \times 10^{-11}$ mbar). The preparation chamber is equipt with a mass spectrometer, a metal evaporator, low energy electron diffraction (LEED), Auger electron spectroscopy (AES), and a thermal hydrogen cracker designed by Tectra. The preparation and STM chambers each have an ion pump and a titanium sublimation pump. The STM chamber contains solely the STM. During imaging, the STM head rests on the sample holder which is on a stage. The stage suspension system is a combination of spring suspension and eddy current damping. While taking measurements, the turbo and scroll pumps are disengaged and the entire apparatus is on a pneumatic vibration isolation system.

The experiments described in this thesis utilized the thermal hydrogen cracker and the STM. The thermal hydrogen cracker breaks the H_2 bond creating atomic hydrogen. The H_2 molecule is passed through a heated capillary that thermally breaks the molecular bond leaving the hydrogen atoms to flow into the chamber. The capillary is heated by creating a 1 kV voltage difference between the capillary walls and the tungsten filament. The electrons emitted by the filament are accelerated towards the walls of the capillary and upon impact, release their kinetic energy as heat. When the sample is within 10 cm of the shutter of the hydrogen cracker, the vast majority of hydrogen atoms do not recombine before hitting the surface of the sample [86].

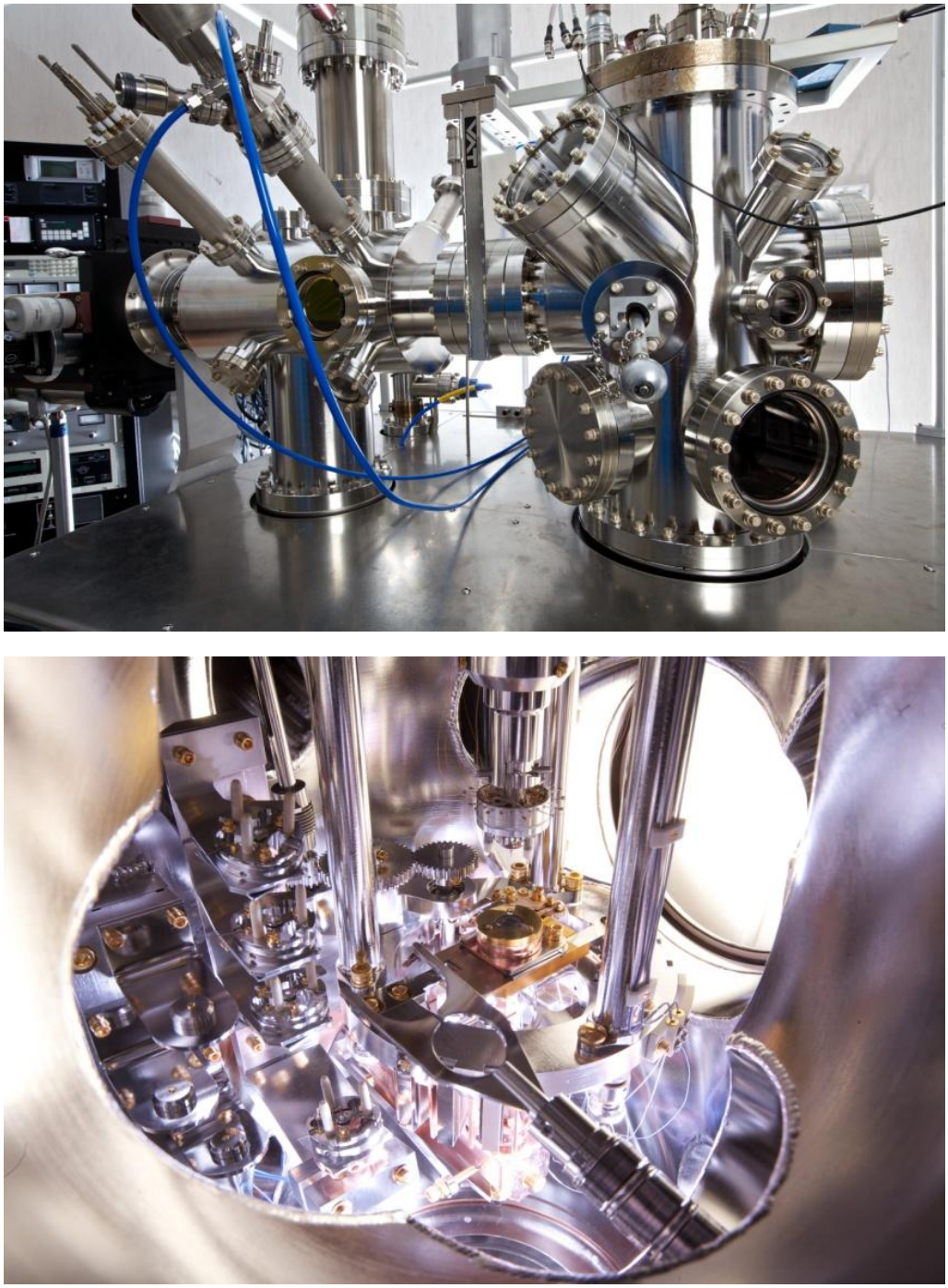

Figure 19: Scanning tunneling microscope used in the experiments presented in this thesis. The lower image is a view inside the STM chamber. Photographs courtesy of Massimo Brega.

3.4 BUFFER LAYER ON SIC

3.4.1 *Characterization of the Buffer Layer*

A buffer layer sample was grown in our prototype system after removing the scratches by hydrogen etching. The silicon carbide was heated to 1550°C for 12 minutes in an argon atmosphere at 790 mbar. The Raman spectra acquired on the sample do not show the 2D peak around 2700 cm^{-1} (Fig. 20), indicative of graphene and graphite. The peak structure visible below 1900 cm^{-1} is due to the SiC crystal [87].

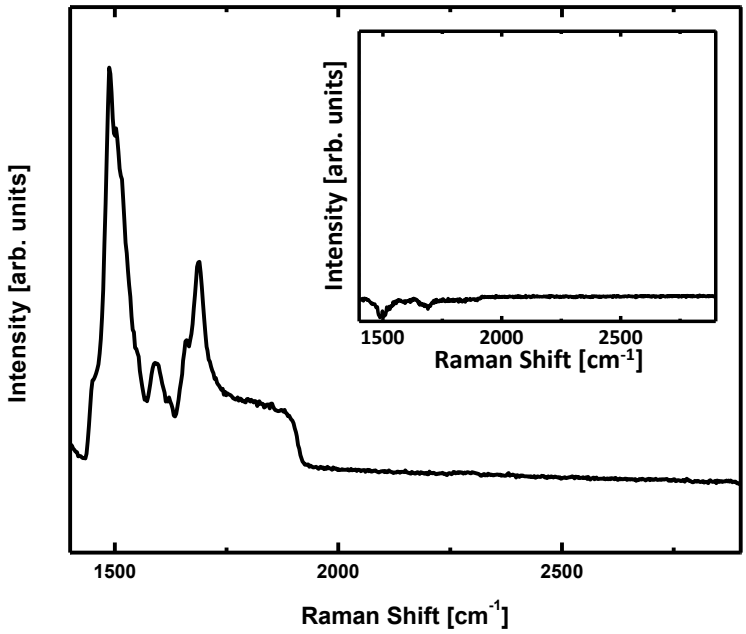

Figure 20: Raman spectrum of the buffer layer. The spectrum does not show a 2D peak around 2700 cm^{-1}. The inset shows the Raman spectrum of the buffer layer after the SiC substrate spectrum has been subtracted. No 2D peak or G peak are visible.

In buffer layer samples, there is no G band or 2D band making it difficult to distinguish between the signal of silicon carbide and that of the buffer layer using Raman spectroscopy alone [88]. When the growth is stepwise and the process has been perfected, it is possible to deduce where the buffer layer is, provided that its presence has been verified by other characterization methods such as ARPES (see Fig. 17a). When the monolayer graphene signal is found at the step edges and there is no monolayer signal in the terraces, then the buffer layer is assumed to be in the terrace. In these preliminary studies, only Raman spectroscopy and SEM were used to characterize the samples.

The SEM images provide information regarding the morphology of the growth. The buffer layer in Fig. 21, shows terraces approximately 1µm in width. The steps consist of two shades of grey. When the SEM images are considered with the Raman measurements which showed no 2D peak across the steps of the

Figure 21: SEM image of the buffer layer. The step are clearly visible with two shades of grey. The darker shades along the step edges are the buffer layer. The lighter areas are silicon carbide.

sample, it can be deduced that the lighter shade is the silicon carbide surface and the darker shade is the buffer layer. The growth is stepwise with the darker shade on the edge of the steps. This is one of the first buffer layer samples grown in the prototype system newly installed in Pisa and further analysis and characterization should be carried out before these samples are used for experiments.

The buffer layer samples characterized below were grown in an optimized classical radio-frequency (RF) induction furnace under an Ar atmosphere at about 1400°C [89]. They were first characterized by angle-resolved photoemission spectroscopy (ARPES), X-ray photoelectron spectroscopy (XPS), atomic force microscopy (AFM), and micro-Raman spectroscopy. ARPES and XPS results for the buffer layer samples are in line with reference [75] and confirm the validity of the preparation protocol.

Combined Raman and AFM measurements were obtained on the sample. The shape of the terraces typically present on the SiC substrate was exploited to obtain spatially-resolved Raman spectra in an area that could be easily identified and measured by AFM. AFM imaging was performed by a Caliber (Veeco) instrument configured in intermittent-contact mode, where topography and phase-images were simultaneously acquired. It was possible to acquire high resolution images of the graphene grown on SiC terraces and to distinguish between the buffer layer and monolayer graphene both by topography and by phase contrast [90].

Spatially-resolved Raman spectra on the buffer layer regions show the typical SiC bands and no graphene-related bands. However, at selected positions the typical 2D band of monolayer graphene was also detected, characterized by a single Lorentzian peak centered at 2760 cm^{-1} with an average full-width at half maximum (FWHM) of ~55 cm^{-1}, which suggests the presence of inhomogeneous compressive strain [87, 91]. Figure 22 shows the Raman signal

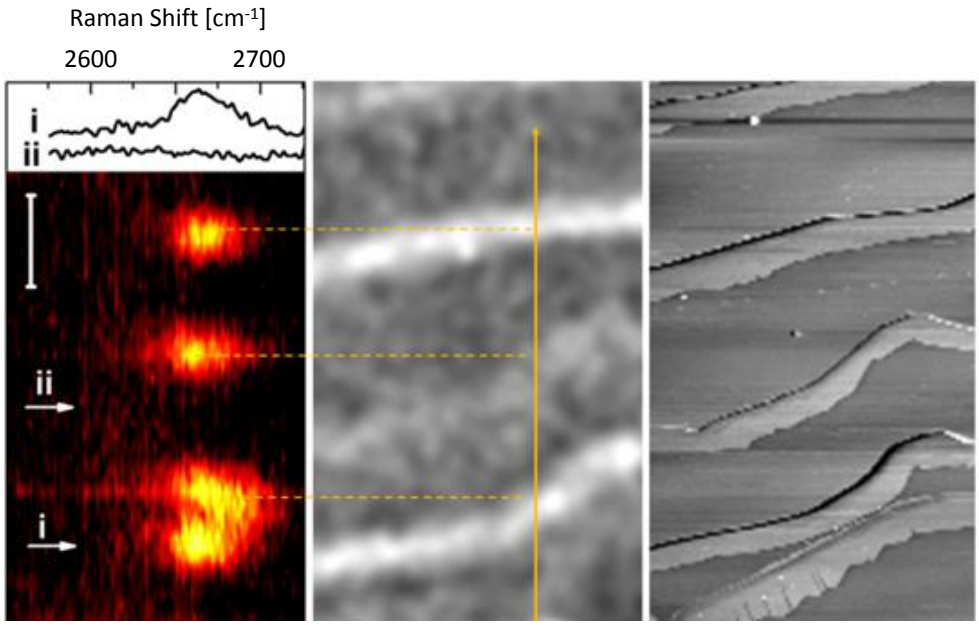

Figure 22: The left panel is an intensity map of the 2D peak acquired along the line in the image in the central panel. The bright areas of the Raman intensity map indicate areas with a peak. The spectrum i was acquired at the step edge (see arrow labeled i) and shows the 2D peak associated with monolayer graphene. The spectrum ii was acquired in the terrace and has no 2D signal indicating the presence of the buffer layer. The central panel is an image taken by an off-axis CCD camera on the micro-Raman setup. The third panel is an AFM phase image showing the steps. From these measurements it is clear that the growth is stepwise with the buffer layer in the terrace and the monolayer signal at the edge.

(left panel), the optical image of the sample (central panel), and the AFM phase signals (right panel) obtained at the same area on the sample. The combined Raman and AFM measurements show that monolayer graphene is only present in the proximity of substrate steps. This is consistent with ARPES and XPS data for the same sample that indicate a low coverage of monolayer graphene. Away from step edges, the sample is covered by only the buffer layer, which in fact does not produce graphene-related Raman signals.

3.4.2 *Atomically-Resolved STM Images of the Buffer Layer*

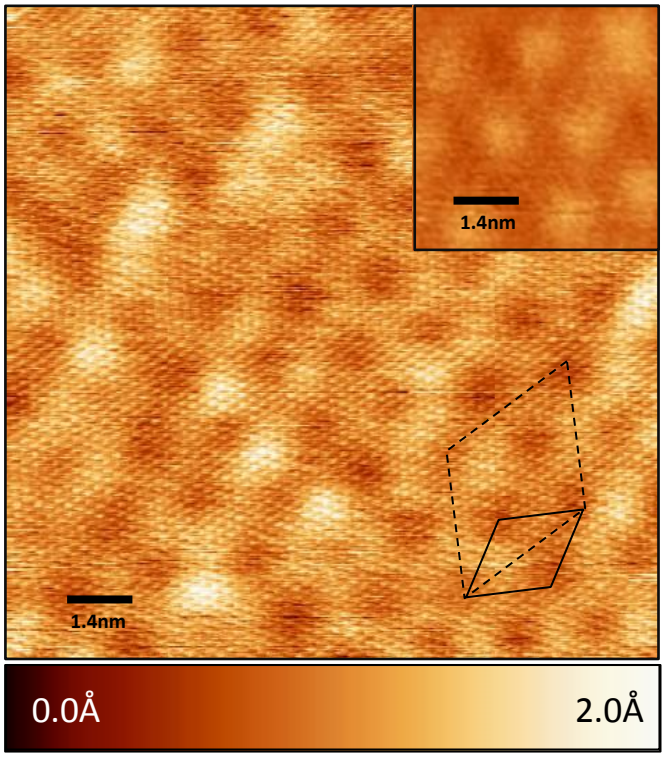

Figure 23: STM images of the buffer layer. The inset shows a low-resolution image of the buffer layer. In the main STM image, atomic resolution is visible and both the quasi-(6x6) (solid diamond) and the $(6\sqrt{3}\text{x}6\sqrt{3})\text{R}30°$ (dotted diamond) are visible. Image parameters: +1.7 V, 0.3 nA.

STM was performed within the central terrace regions (away from step edges) where Raman and AFM analysis confirm the presence of the buffer layer on the sample surface. Figure 23 shows two images of the buffer layer taken with a sample tunneling bias U_T of +1.7 V where the long-range periodicity of the surface is easily observed in STM. The main plot in Fig. 23 shows the surface imaged under tunneling conditions where, already on this large scale, atomic resolution of the buffer layer can be recognized. This situation was attained only after imaging the same surface area for an extended period of time (several hours) and most likely as a result of achieving stable tip and tunneling conditions. The tunneling conditions typically remain stable for about 30 minutes. At earlier stages, images such as those shown in the inset of Fig. 23 and in previous works [69, 72, 92, 93, 94, 95, 96] were obtained.

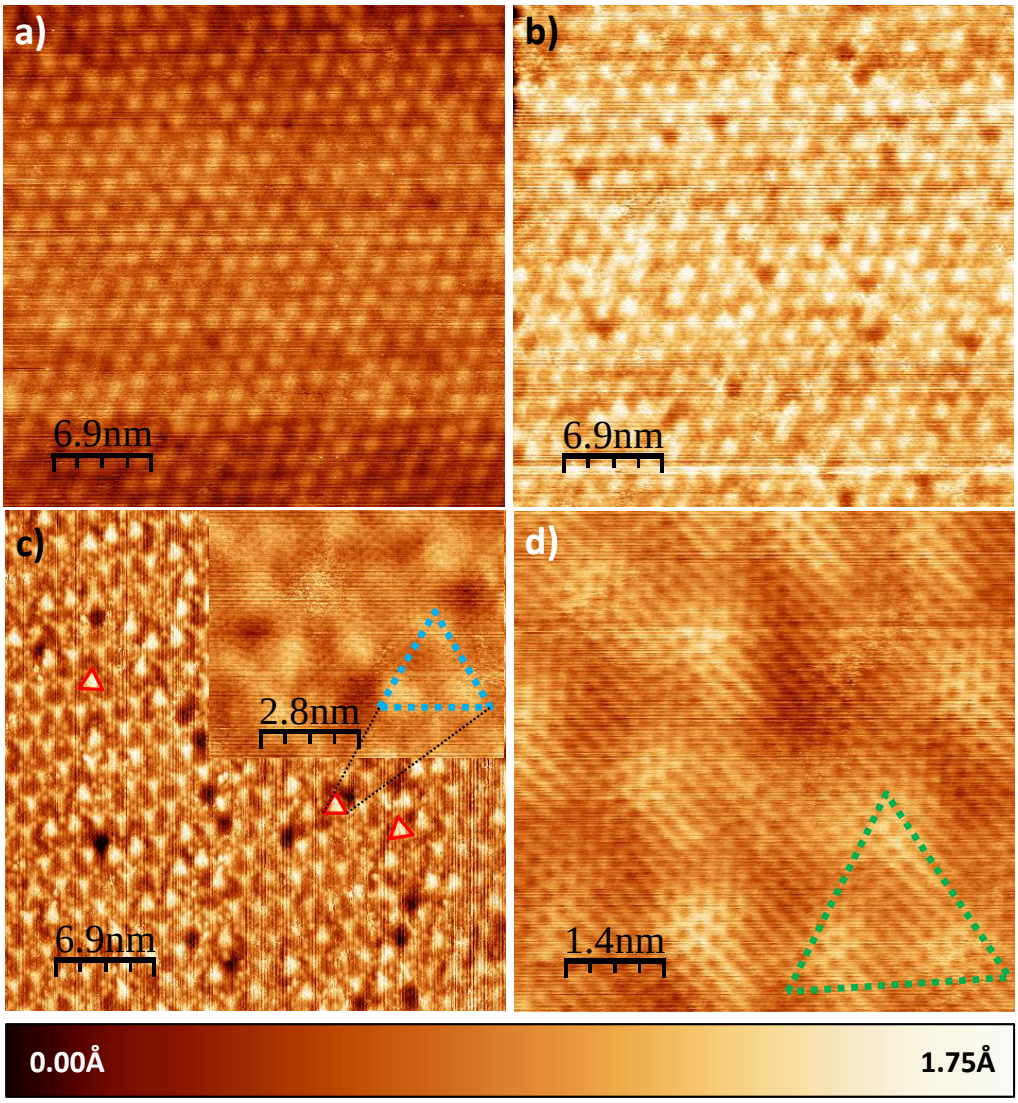

Figure 24: STM images of the buffer layer over time. a) The typical resolution observed on the buffer layer. b) Slightly improved resolution after scanning. c) The best resolution on the buffer layer reported in literature. It is obtained after prolonged scanning on the same area. The inset is a zoomed in image showing that the triangular formations on the surface can be resolved. d) Atomic resolution on the buffer layer where the triangular formations are still visible. Image parameters: a) −0.54 V, 0.3 nA b) −0.54 V, 0.3 nA c) −0.54 V, 0.3 nA d) −0.22 V, 0.3 nA.

Before obtaining atomic resolution on the buffer layer, images only show the very basic quasi-(6x6) superperiodicity indicated by the solid diamond in Fig. 23. As the tunneling conditions stabilize, the simple bright spots with spherical forms shown in Fig. 24a begin to take on more definition (Fig. 24b). When the raised areas have taken on triangular form and there are small circular spots visible in the areas between the triangular forms, the tunneling conditions are approaching those necessary for atomic resolution of the buffer layer (Fig. 24c). These images are on a large scale but once the image size is reduced it becomes clear that the triangular forms are actually three circular protrusions that could not be differentiated at the previous magnification (Fig. 24c inset). Already at this scale, the atomic resolution is visible. If the scan area is further reduced (24d), the hexagonal lattice becomes clearly visible. When the tunneling conditions stabilize and the resolution improves, the images show more details and the quasi-(6x6) superstructure is resolved. This accounts for the variation of the buffer layer images observed in literature [69, 72, 92]. The pictures shown in Fig. 23 are dominated by the quasi-(6x6) corrugation which is indicated in the main image by the solid diamond together with the $(6\sqrt{3}x6\sqrt{3})R30°$ unit cell as a dashed diamond. The measured unit vector lengths of the two periods are 1.85 nm and 3.2 nm, respectively, as expected [72]. The strong and easily imaged corrugation of the surface is a consequence of the covalent bonds that form between approximately 30% of the buffer layer carbon atoms and the silicon atoms of the SiC(0001) surface [70, 97], as sketched in Fig. 25. The buffer layer is smoothly varying on an atomic scale with a superstructure due to the covalent bonds to the substrate. The out of plane displacement of single atoms is limited by their covalent bonds to the three neighboring carbon atoms; it is energetically favorable to distribute the strain on several neighboring bonds. The typically observed long range periodicity known as the quasi-(6x6) observed for the buffer layer [71, 72, 93, 98] is clearly resolved in the STM image shown in Fig. 26. When STM images of the buffer layer cover a small area, it is often difficult to clearly recognize the long range periodicity since very few periods are present and only the change in height is apparent. However, these images indubitably resolve an additional periodicity that displays a graphene-like atomic arrangement. The atomic structure of the buffer layer is fully resolved in Fig. 25, a close up STM image obtained at a sample bias of -0.223 V. The honeycomb structure has a measured lattice constant of 2.5 Å $\pm$ 0.1 Å clearly showing a graphene-like topography. The graphene lattice constant is 2.46 Å which falls within the error of the measured buffer layer lattice constant. Some atomically resolved images of the buffer layer also show the $(6\sqrt{3}x6\sqrt{3})R30°$ unit cell. Resolving the honeycomb structure was also possible at higher biases but never for values of $|U_T| < 200$ mV. Tunneling conditions became unstable below this sample bias, as expected for the buffer layer [95]. Atomically-resolved images such as the one reported in Fig. 25 were consistently acquired when measuring within the terraces in several different areas of the sample. These first STM images of the buffer layer with full atomic resolution clarify the debate concerning the atomic structure of the buffer layer. They demonstrate that the buffer layer is topologically identical to monolayer graphene and thus represents a true periodic carbon honeycomb structure.

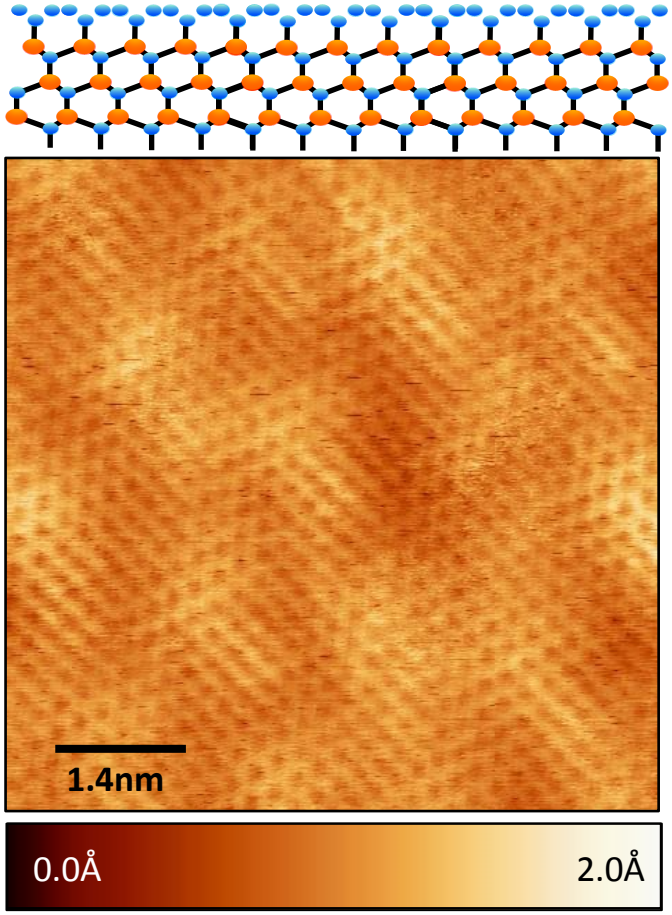

Figure 25: Atomic resolution STM image of the buffer layer. Image parameters: −0.223 V, 0.3 nA. The diagram above is a representation of the covalent bonds between the buffer layer and the substrate. The orange circles are Si and the blue circles are C.

Up until this point, the structure of the buffer layer on an atomic scale was still debated since complete atomic resolution had eluded STM studies. Several reports suggested a hexagonal atomic arrangement such as in monolayer graphene [70, 71, 72, 93, 97, 98], but also a nanomesh structure with isolated carbon islands was proposed [92]. The discovery that the buffer layer can be converted into pristine sp^2-bonded graphene (the so-called quasi-free-standing monolayer graphene (QFMLG)) via the intercalation of hydrogen at the interface with the SiC substrate (see sketch in the inset to Fig. 17) [75] was a strong argument in favor of the hexagonal atomic arrangement of the buffer layer. In spite of this, recently an arrangement of hexagonal, pentagonal, and heptagonal atomic placements [99] was put forward as the buffer layer geometry. The clarification of the atomic structure of the buffer layer is imperative for understanding and controlling the epitaxial growth of mono- and few-layer graphene on SiC(0001). The above atomically-resolved STM images of the buffer layer clearly demonstrate a graphene-like honeycomb structure, hence resolving the dispute on the atomic arrangement within the interface layer.

3.4.3 *Corrugation*

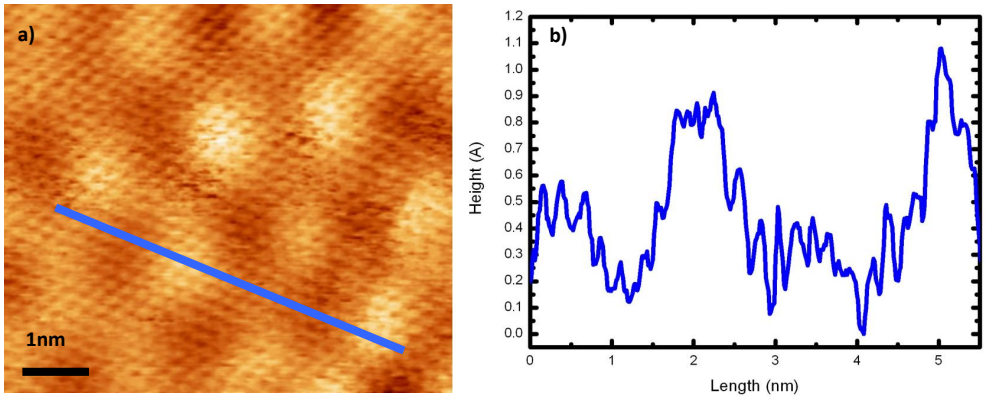

Figure 26: a) STM image of the buffer layer. b) The profile taken along the blue line shows the high corrugation. Image parameters: 2 V, 0.3 nA.

Figure 26a illustrates a roughness analysis of the surface. For this purpose the images were filtered with a Gaussian profile of decay length 3 pixels (1 pixel ~0.18 Å) to reduce noise. A line-profile analysis of the buffer layer image is shown by the blue line in Fig. 26b and demonstrates the high corrugation of this interface layer which is a result of the spatially-varying coupling to the SiC substrate mediated by covalent bonds as noted previously. The peak-to-peak corrugation value of 1.1 Å agrees with what was theoretically calculated by Varchon et al. [71]. The root mean square (RMS) roughness value, calculated from 5 buffer layer images of 25 nm^2 each, is 0.178 Å $\pm$ 0.020 Å.

3.4.4 *STS Analysis*

To further demonstrate that the atomic resolution images were obtained on the buffer layer and not on minor inclusions of monolayer graphene, STS was

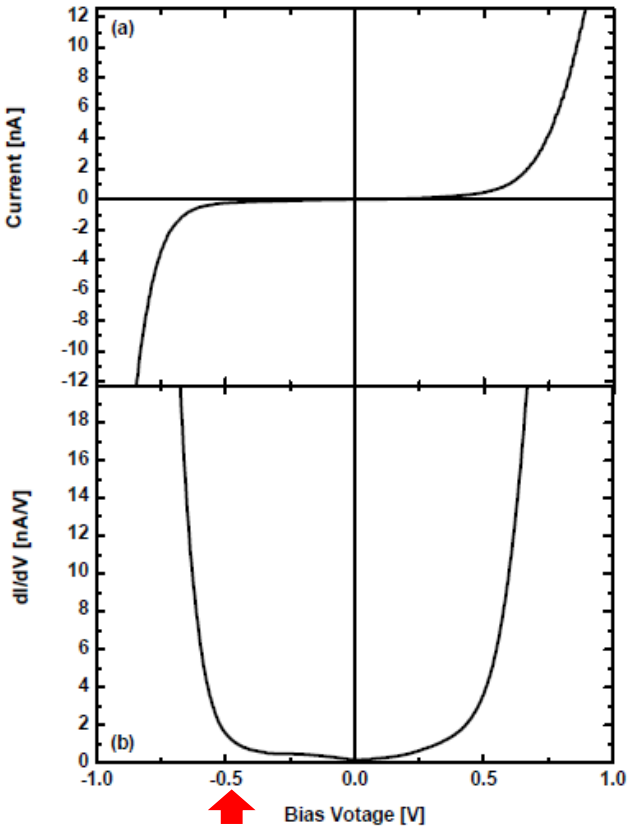

Figure 27: STS acquired on the buffer layer on an area where atomic resolution was observed. a) I/V and b) dI/dV vs. V curves. The red arrow indicates where the delocalized states in the buffer layer are visible in the ARPES measurements. Setpoint: −0.53 V, 0.3 nA.

performed on the same areas imaged by STM. Figure 27a shows the average of multiple I-V curves acquired in various points on the buffer layer. The extremely low currents measured for tunneling voltages in the range from -0.5 V to $+0.5$ V confirm that the images were taken on buffer layer areas. A low density of states in the vicinity of the Fermi level is a consequence of the strongly-modified electronic structure of the buffer layer due to partial hybridization of its carbon atoms with the SiC substrate [70, 97]. Figure 27b shows the differential conductance spectrum, i.e. the derivative of the I-V curve plotted in panel a. The buffer layer spectra show virtually no conductance over an energy range of approximately $\pm$ 0.5 eV with respect to the Fermi level. The reported dI/dV curve is qualitatively similar to the one obtained by Rutter et al. for the buffer layer [95].

As a summary of the results on the buffer layer, the Raman measurements demonstrate that the samples are buffer layer except at the step edges where there are monolayer inclusions, typical of growth on SiC(0001) which starts at the step edge. The long range $(6\sqrt{3}\text{x}6\sqrt{3})\text{R}30^\circ$ periodicity due to C-Si bonds is visible when the STM images are taken on a large scale. When atomic resolution is achieved, the variation in height is more than 1 Å as expected. These are the first atomically resolved images of the buffer layer showing the true honeycomb structure of the carbon atoms clarifying the debate surrounding the topography of the buffer layer. The bias voltage needed for atomic resolution is in the energy range where there are delocalized states in the buffer layer (see ARPES data in Fig. 17a).

3.5 MONOLAYER GRAPHENE ON SIC

3.5.1 *Characterization of Monolayer Graphene*

Figure 28a shows a Raman spectrum after substraction of the SiC background, leaving the monolayer graphene spectrum clearly visible. The G band is at 1610 cm^{-1} and the 2D band is at 2760 cm^{-1}. The shift in the G and 2D bands is a result of doping and strain in the graphene layer [87, 100]. It is often arduous to extract the G peak as it lies on the side of a peak of the silicon carbide spectrum. A simple subtraction of the silicon carbide spectrum from the combined graphene-silicon carbide spectrum does not produce a single peak with a flat background as expected (see Fig. 28a). A likely explanation for this is the graphene layer that grows on top of the silicon carbide interacts with the substrate modifying the Raman spectrum so the subtraction of the silicon carbide Raman spectrum does not result in a level background. For this reason, we focus on the 2D peak to identify the graphene samples grown on silicon carbide. A spatial map of the intensity of the 2D band is shown in Fig. 28b. The uniform light areas indicate the presence of the 2D band, evidence of monolayer graphene whereas the dark areas are the buffer layer, no 2D peak is observed.

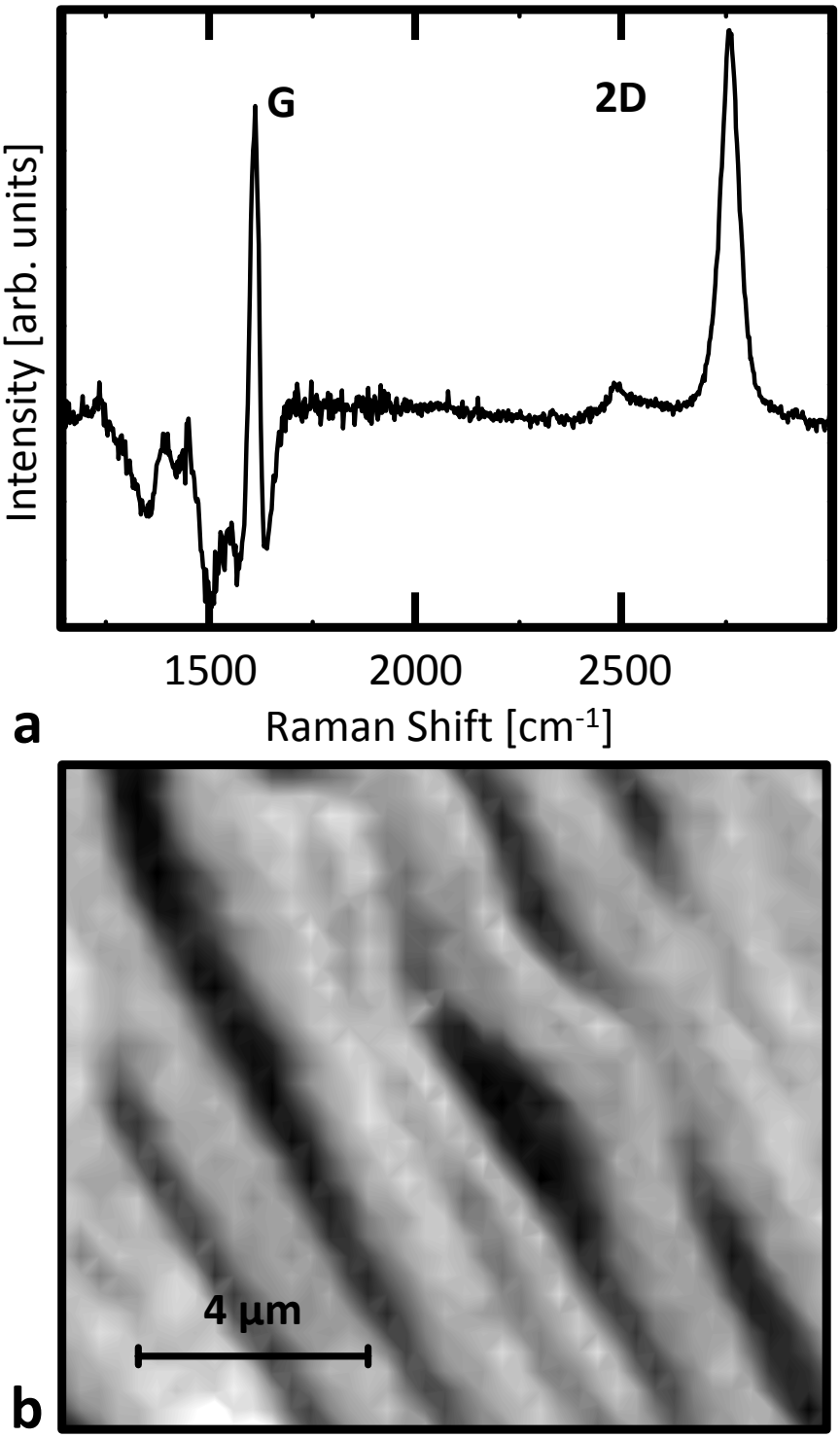

Figure 28: (a) The Raman spectrum of monolayer graphene after subtracting the SiC background. The G band is at 1610 cm^{-1} and the 2D band is at 2760 cm^{-1}. (b) Micro-Raman intensity map of the 2D band. The light areas indicate the presence of a 2D peak similar to the one seen in panel a. The dark areas do not have a 2D peak. These regions are the buffer layer.

3.5.2 *Atomically-Resolved STM Images of Monolayer Graphene*

The STM images on monolayer graphene are sensitive to the tunneling bias. Since the density of states is linear where the π-bands cross, it would appear that the best STM images would be acquired away from the Dirac point where the density of states is higher and the tunneling would be more favorable. Contrary to this reasoning, the best images were acquired at low bias. The reason why the best atomic images of the graphene layer were obtained at low bias may result from bringing the tip closer to the sample. As the bias is decreased, the distance between the tip and the sample is decreased to allow the same amount of tunneling current to be detected. When the tip is very close to the sample, the corrugation measured is higher [80]. This might explain why images at a lower bias provide atomic resolution. Some of the best monolayer images were obtained at a bias of ~0.115 V, a bias at which the buffer layer could not be atomically imaged. Images acquired at low bias (Fig. 30) resolve the honeycomb lattice almost immediately, unlike the buffer layer where the atomic images are only obtained after prolonged imaging.

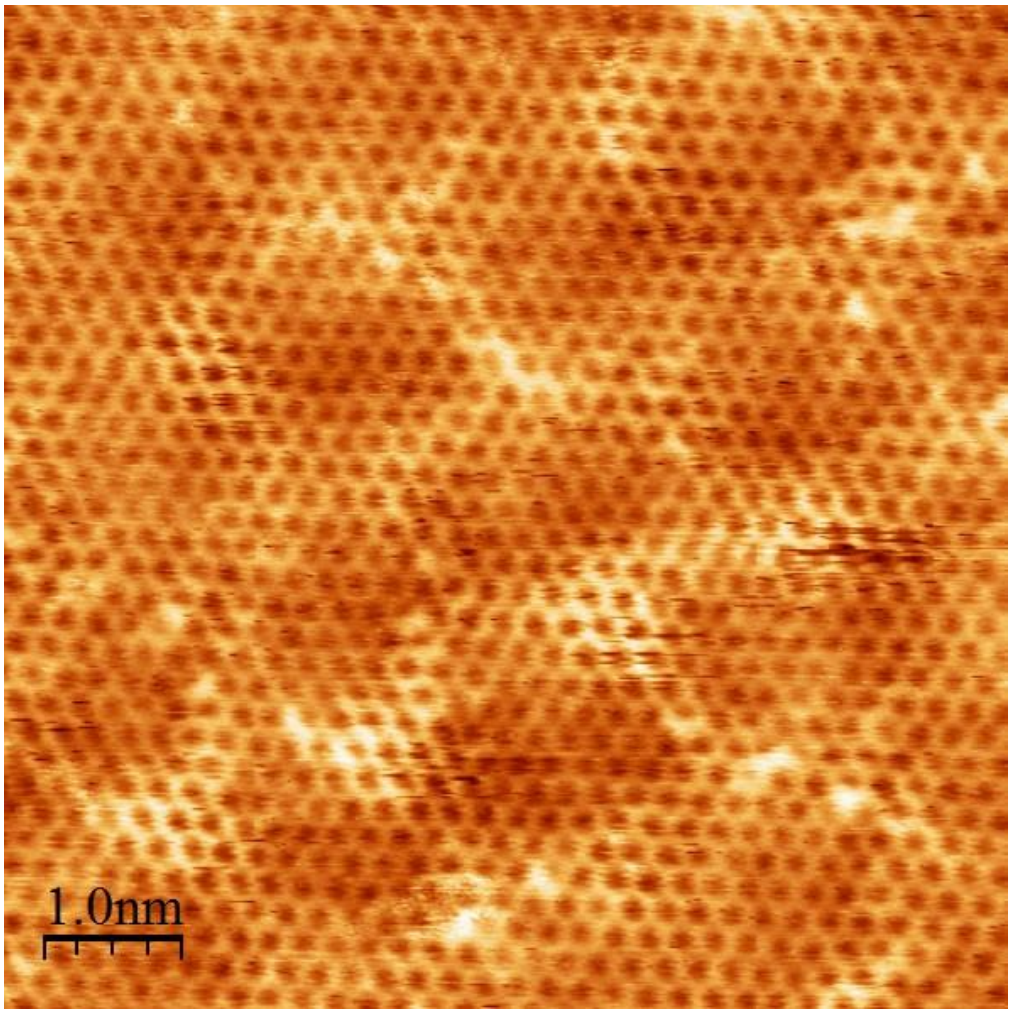

Figure 29: STM image of monolayer graphene. Image parameters: −0.292 V, 0.3 nA.

An atomic resolution STM image acquired on monolayer graphene with a bias voltage of −0.292 V and a tunneling current of 0.3 nA is shown in Fig. 29. The quality of the monolayer is clearly visible due to the lack of defects. The white spots on the image are probably adsorbates stuck on the surface.

3.5.3 *Corrugation*

Both the buffer layer and monolayer graphene are hexagonal lattices formed by carbon rendering the identification of the layer a more in depth process. The corrugation of the monolayer is lower than the buffer layer. The monolayer is a relaxed graphene lattice and does not conform exactly to the buffer layer below which exhibits a much higher corrugation (~1.2 Å) due to the sp^3 bonds to the silicon reconstruction. The peak to peak height in the case of monolayer graphene is ~0.4 Å, topological information that can be extracted from STM images (see Fig. 30).

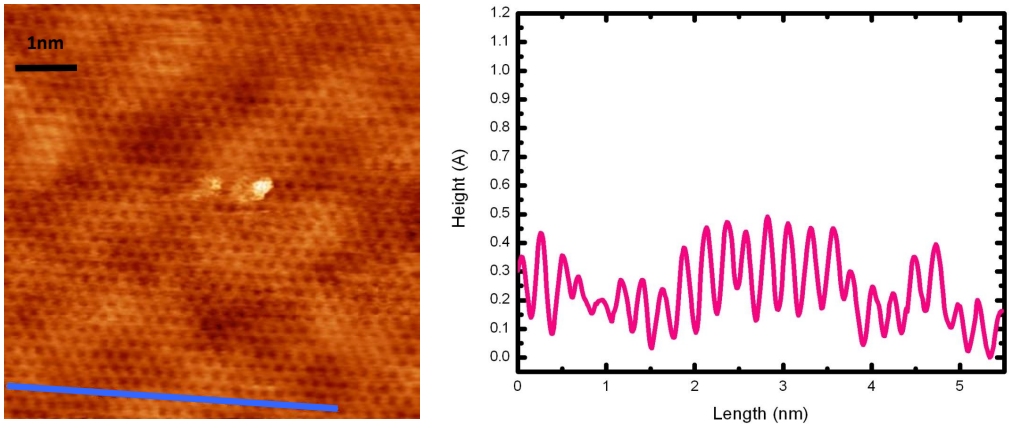

Figure 30: STM image of monolayer graphene. The profile was taken along the blue line. Image parameters: +0.023 V, 0.3 nA.

3.5.4 *STS Analysis*

The buffer layer has delocalized states that form due to the periodic sp^3 bonds to the substrate that interrupt the sp^2 bonds in the carbon lattice forming an insulating material. Monolayer graphene is a gapless semiconductor with a linear band structure in which the π-bands cross. The density of states can be probed by STS. A dI/dV versus V average curve shown in Fig. 31 obtained from 30 spectra shows that the density of states decreases approximately symmetrically to a minimum around a bias voltage of zero, similar to the observations by Lauffer et al. [93]. Usually graphene grown on SiC(0001) is n-doped with a carrier density of about $n = 10^{13}$ cm^{-2} [70]. Monolayer graphene grown on SiC(0001) has the Dirac point shifted to −0.4 eV [101, 102] yet the density of states extracted from STS measurements appears to have a minimum at a bias voltage of 0 V and does not go completely to zero. The results obtained here are in agreement with the results of other groups [93, 95].

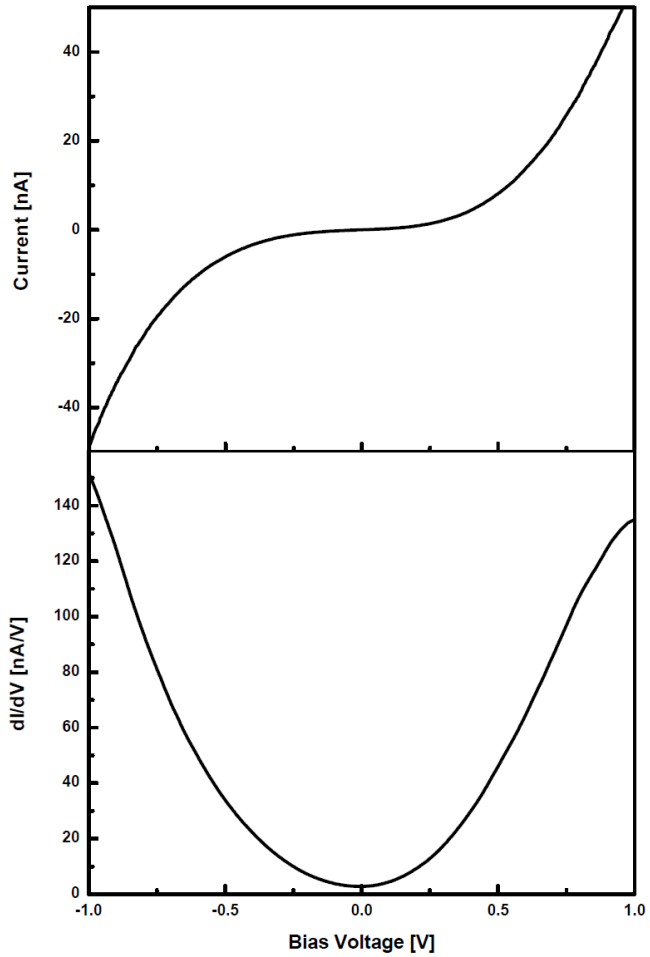

Figure 31: STS of monolayer graphene. Setpoint: 0.115 V, 0.3 nA

The STS data obtained on monolayer graphene on SiC(0001) shows a minimum of the dI/dV curve at a sample bias of approximately 0 V. At first glance, this is in disagreement with the angle-resolved photoemission spectroscopy (ARPES) results showing that the Dirac point on monolayer graphene on SiC(0001) is at approximately −0.4 eV to −0.5 eV [93, 101, 102, 103]. One would expect a minimum in the STS dI/dV data at approximately −0.4 V to −0.5 V and not at 0 V since STS data is a measure of the density of states of a material.

The first piece of the puzzle concerns the dI/dV of monolayer graphene that shows a minimum at 0 V, the chemical potential of the graphene sample. In 2008, Zhang et al. discovered that the minimum in the STS measurements results from the reduction of elastic tunneling around the chemical potential in addition to the suppression of inelastic tunneling from out-of-plane acoustic phonons below approximately 67 meV [103]. The contribution from inelastic tunneling through channels opened by the acoustic phonons significantly augments the conductance through the following process. Electrons tunnel from the STM tip to the σ^* band in the vicinity of the Γ point. Subsequently, the electrons lose energy to an out-of-plane acoustic phonon with momentum **K′** (**K**) and fall to an available **K** (**K′**) state at the chemical potential thereby conserving energy and momentum [103]. If the phonon-mediated inelastic tunneling cannot occur because there is not enough excess energy, the electron must tunnel directly to the states at the chemical potential, which are close to the **K** (**K′**) points [103]. Since the tunneling current decays exponentially and the decay length is smaller for electrons tunneling to large momentum surface states such as around **K** (**K′**), the STS measurements have a minimum at 0 V where the elastic tunneling is greatly reduced and the inelastic tunneling channels are inaccessible [77, 103].

In all publications, there is always a clear minimum in the STS measurements at 0 V but the Dirac point is only weakly visible as a small dip when the graphene is on an SiO_2 covered Si substrate [93, 95, 103, 104]. In monolayer graphene on SiC(0001), the STS data has a minimum at 0 V but no minimum is visible at approximately −0.4 V, as expected from the ARPES measurements [70, 93, 95, 101, 102]. There are two factors which contribute to the missing minimum in monolayer graphene on SiC(0001); the buffer layer and the relationship of tunneling current with distance [93]. The buffer layer, as discussed previously has a delocalized state at around −0.2 to −0.6 eV, precisely in the range of the Dirac point of monolayer graphene. This delocalized state is apparent in the STS dI/dV data obtained on the buffer layer as shown in Fig. 27b. STS on monolayer has contributions from both the monolayer and the buffer layer since the tunneling current decreases exponentially with distance (Eq. 16) [77, 93]. The resulting STS spectrum on monolayer graphene does not show a dip in the dI/dV curve at approximately −0.4 V as expected from ARPES measurements because the buffer layer has a delocalized state in that range which cancels out the expected minimum, leaving only the minimum at 0 V due to the chemical potential [93]. In the bilayer graphene case, the contribution of the buffer layer to the bilayer graphene STS is negligible due to the exponential behavior of tunneling current with distance and therefore the dip in the density of states is clearly visible at the Dirac point of bilayer graphene at 0.31 eV [93].

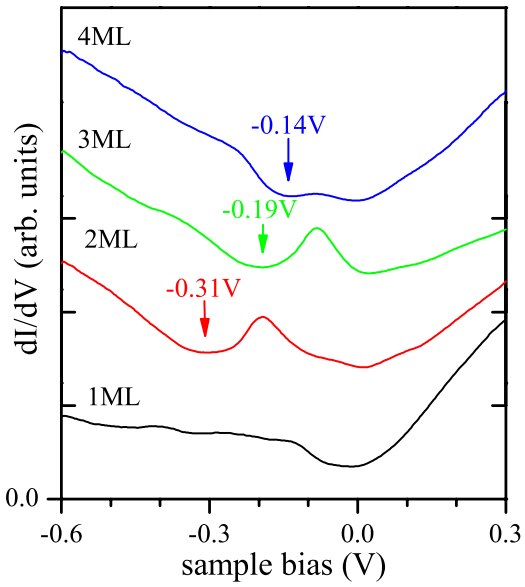

Figure 32: Spectra, dI/dV versus sample bias (V), from single to four layer graphene on SiC(0001), (black line, red line, green line, and blue line, respectively). The spectra are vertically offset with the tick marks on the dI/dV axis representing the zero dI/dV for each spectrum [93]. The figure is from reference [93].

In trilayer and quadlayer graphene, the minimum in the STS data below 0 V shifts to higher energy in agreement with the ARPES measurements [93, 101]. Figure 32 shows the STS of monolayer to quadlayer graphene on SiC(0001) as measured by Lauffer et al. in which the features described above are visible [93]. In summary, the buffer layer's delocalized states in the same range as the Dirac point in monolayer graphene on SiC(0001) are contributing to the STS spectra, canceling out the minimum as expected from the ARPES data [93].

In conclusion, monolayer graphene can be identified by STM by the hexagonal lattice arrangement of the carbon atoms with a low peak-to-peak height variation of 0.4 Å, much lower than the buffer layer. The STM measurements can be acquired at a bias voltage below 0.2 V, where the buffer layer cannot be imaged. Furthermore, the STS dI/dV data show a minimum around 0 V with a nearly symmetric shape around 0 V, typical of monolayer graphene. These monolayer graphene samples were not grown in our lab in Pisa since the CVD parameters are still being optimized.

3.6 QUASI-FREE-STANDING MONOLAYER GRAPHENE ON SIC

3.6.1 *Characterization of Quasi-Free-Standing Monolayer Graphene*

A high quality graphene monolayer can be formed by converting a buffer layer into a monolayer. As was shown previously, the buffer layer is topologically identical to the monolayer without exhibiting the electronic properties of graphene. Passivating the SiC reconstruction with atomic hydrogen, thereby breaking the silicon-carbon bonds and returning the carbon layer to its zerogap semiconductor state, could provide high quality graphene since the starting material is essentially defect free. The quasi-free-standing monolayer graphene was characterized by ARPES (not presented here), micro-Raman, and STM.

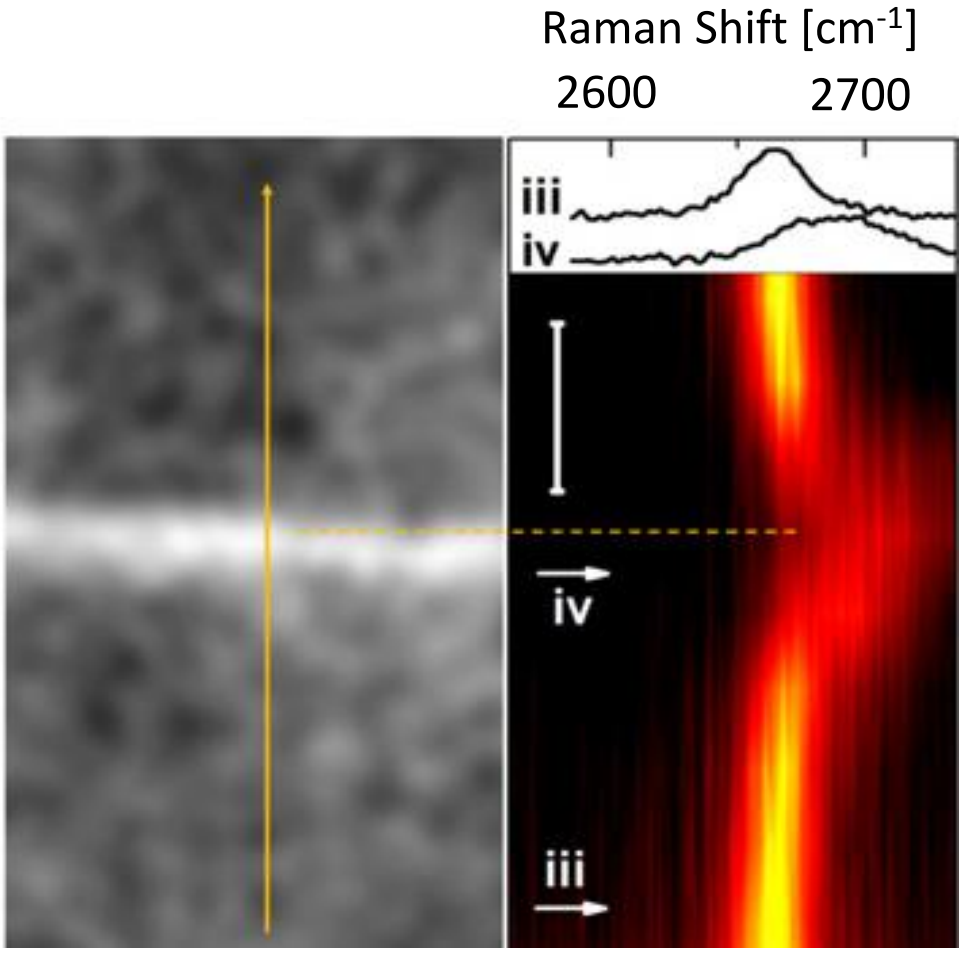

Figure 33: The panel on the left is an optical image taken by the off-axis CCD camera on the micro-Raman setup. The right panel shows the Raman spectrum of the 2D peak of QFMLG obtained across the step shown on the left. The 2D band shows monolayer graphene (iii) on the terrace and multilayer graphene (iv) at the step edge.

The micro-Raman maps of the 2D band on the buffer layer (Fig. 22) show the step edge growth of graphene. On the terraces the samples are uniformly

buffer layer but at the step edge where the growth initiates, there is monolayer graphene (Fig. 22). Passivation of the buffer layer samples leads to monolayer graphene on the terraces with multilayer graphene at the step edge. Figure 33 shows that on the terraces, there is a symmetric 2D band at 2663 cm^{-1} with a FWHM of ~30 cm^{-1}, indicating the presence of monolayer graphene. Near the step edges, the 2D peak becomes much broader and shifts to higher energies. The broadening of the 2D peak attests to multiple layers of graphene and shifts can occur because of doping [100]. QFMLG is known to be p-doped [75] so it is possible that the multiple layers at the step edge are also p-doped which cause the shift observed in Fig. 33.

3.6.2 *Atomically-Resolved STM Images of Quasi-Free-Standing Monolayer Graphene*

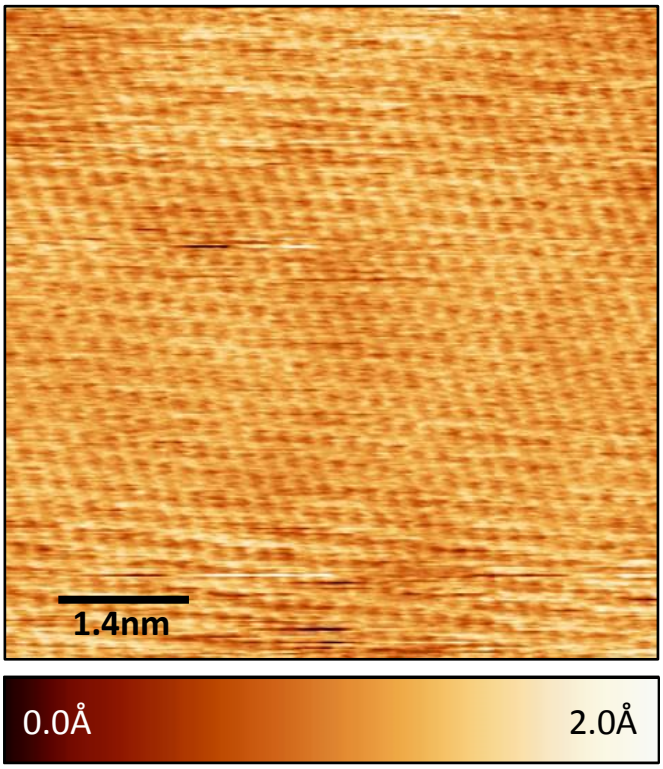

Figure 34: STM image of QFMLG. Image parameters: +0.103 V, 0.3 nA.

Figure 34 shows an STM image of QFMLG obtained at a sample bias of +0.103 V, a bias that yields clear atomically resolved images on monolayer graphene but at which the buffer layer cannot be imaged [69, 72, 73, 93, 95, 105]. The lattice constant extracted from these images is 2.4 Å ± 0.1 Å consistent with that of pristine graphene. The quasi-(6x6) periodicity present on the buffer layer disappears after intercalation of hydrogen, and the layer appears flat. Also, no obvious atomic defects can be observed in Fig. 34 or in other QFMLG images. This indicates that the process of hydrogen intercalation is rather gentle, and de-

spite the high process temperature additional atomic defects are not noticeably introduced into the graphene layer.

3.6.3 *Corrugation*

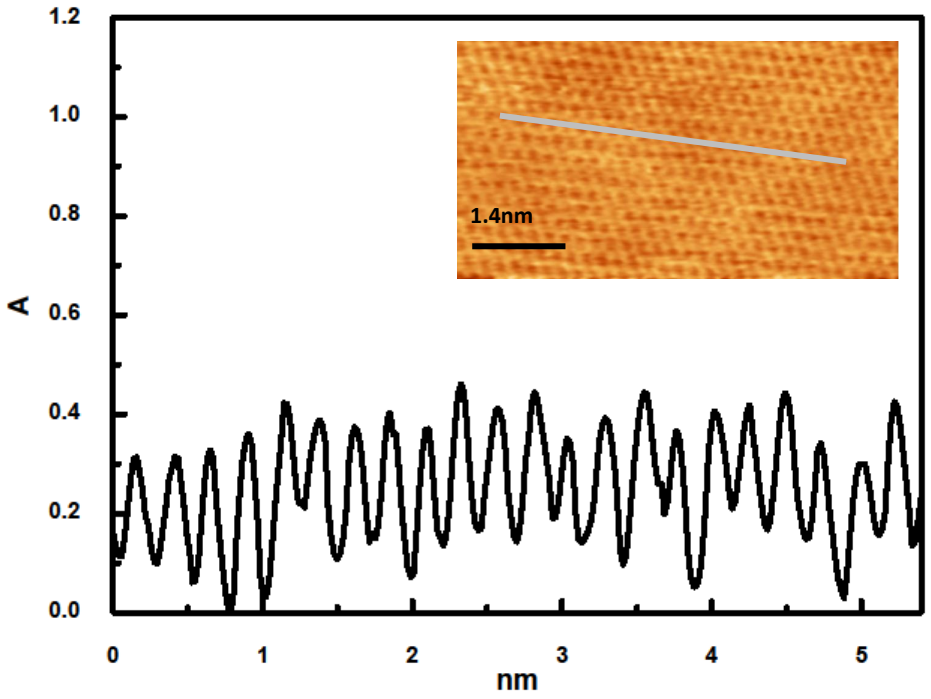

Figure 35: Profile of QFMLG obtained along the grey line in the inset. Image parameters: −0.1 V, 0.3 nA.

A roughness analysis was carried out on the QFMLG. The same Gaussian smoothing applied to the buffer layer images was used to reduce the noise in the QFMLG images. A line profile analysis yields a peak-to-peak corrugation of approximately 0.4 Å, as shown in Fig. 35. The RMS value calculated from 5 QFMLG images is 0.125 Å ± 0.005 Å, demonstrating that QFMLG is flatter than the buffer layer. When comparing the RMS values of these two surfaces it is important to consider that both the long-range corrugation due to the reconstruction and the atomic corrugation contribute to the peak-to-peak values, so that the real differences in reconstruction-related corrugation are actually more pronounced. For the buffer layer, the corrugation due to the $(6\sqrt{3}x6\sqrt{3})R30°$ reconstruction alone amounts to approximately 0.6 Å [73]. On the other hand, for QFMLG the peak-to-peak corrugation is dominated by the graphene lattice (~0.3 Å) while the residual long-range variations are around 0.1 Å.

The STM images of the QFMLG show that the long range periodicity is no longer visible. The STM images provide the topological information needed to demonstrate that the hydrogen intercalation process was successful and the long range periodicity due to the sp^3 bonded carbon atoms has been relieved.

3.6.4 *STS Analysis*

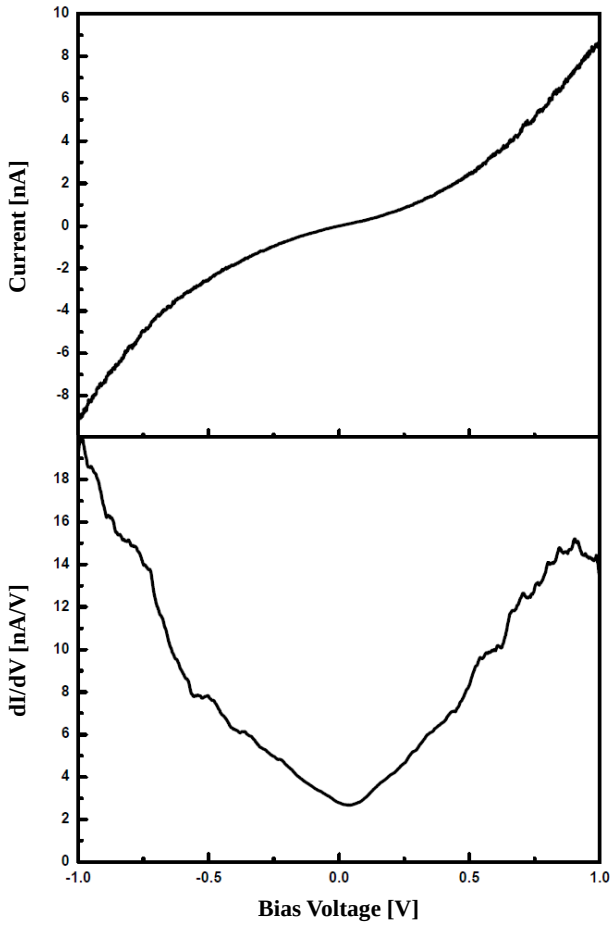

Figure 36: STS of QFMLG. It is similar to that of monolayer graphene (Fig. 31). Setpoint: 0.1 V, 0.3 nA.

The electronic structure of QFMLG should be similar to that of monolayer graphene. The differential conductance curves of QFMLG display a minimum near zero sample bias but the value is finite and does not vanish similarly to as-grown monolayer graphene on SiC(0001) (see Fig. 31). QFMLG appears to be slightly p-type doped as the minimum of the dI/dV curve i.e., the Dirac point, is shifted to a positive sample bias of about 13 mV (Fig. 36).

In summary, hydrogen intercalation lifts the electronic coupling of the buffer layer to the substrate and changes the electronic structure from an insulator to pristine graphene. The quality of the QFMLG was studied by STM and showed no obvious atomic defects indicating both the quality of the starting lattice (buffer layer) and the effective and non destructive intercalation process. The QFMLG is also extremely flat and does not appear to have any sort of intrinsic rippling.

4

HYDROGEN ON CORRUGATED GRAPHENE

Atomic hydrogen was adsorbed on the surface which was subsequently studied by scanning tunneling microscopy and spectroscopy. Initially, the monolayer graphene sample was exposed to a low flux of atomic hydrogen for a short duration of time. As the exposure time increased, a band gap opened as predicted for graphane [67]. Section 4.1.1 will address this behavior. As the quantity of hydrogen adsorbed on the surface augmented, the tunneling between the tip and the sample became increasingly unstable at the optimal tunneling parameters because the number of states available for tunneling decreased to zero. This constraint dictated the parameters for studying the interaction between hydrogen and graphene as a function of curvature: short exposure to a low flux of atomic hydrogen and a low bias voltage to resolve the graphene lattice. Our initial studies focused on identifying the stable hydrogen conformations on the graphene surface and comparing them to theory. Simultaneously the preferential adsorption of hydrogen on the convex areas, exacerbating the long range periodicity of the monolayer graphene on SiC(0001) was observed by scanning tunneling microscopy. The graphene-hydrogen binding energy on the convex areas of the lattice was estimated by a stepwise heating of the graphene layer followed by STM measurements. At approximately 650°C the hydrogen desorbed from the surface leaving a pristine, defect-free graphene layer. The quality of the graphene is maintained after multiple hydrogenation and dehydrogenation cycles making it a very promising reusable material for hydrogen storage. These experiments will be described in detail in this chapter followed by a short section on the preliminary results obtained on hydrogenation of the SiC(0001) buffer layer, a graphene-like lattice with a higher local curvature than monolayer graphene on SiC(0001).

There have been various studies of hydrogen adsorption and desorption on graphite [106, 107, 108, 109, 110, 111] but there is very little experimental work on the adsorption and desorption of hydrogen on graphene as a function of curvature [112]. The in-depth characterization of monolayer graphene on SiC(0001), the buffer layer and quasi-free-standing monolayer graphene were presented in the previous chapter to show their corrugation which will be used in the following to study the interaction of atomic hydrogen on graphene and the effect of local curvature on this interaction. Quasi-free-standing monolayer graphene is exceptionally flat rendering it unsuitable for corrugation studies. The buffer layer is highly curved but the results on this surface must be analyzed with caution since there are sp^3 bonds to the substrate in the concave areas eliminating the possibility of forming C-H bonds in the troughs. Monolayer graphene on SiC(0001) is an advantageous system for studying the role of local curvature on the binding energy of hydrogen on graphene. This system is periodically corrugated on a nm scale and there are no sp^3 bonds to the substrate.

4.1 HYDROGEN INTERACTION ON CORRUGATED MONOLAYER GRAPHENE

4.1.1 *Experiment*

The monolayer graphene samples used in the experiments were characterized as discussed in chapter 3. Figure 37 summarizes the results. Panel a is the Raman spectrum of the monolayer after subtracting the SiC background. A micro-Raman spatial map of the intensity of the 2D peak is shown in panel b. The light areas show a 2D peak such as the one in panel a, indicating monolayer graphene. The dark areas are the buffer layer where no 2D peak is measured. Panel c shows an STM image of the sample with the graphene lattice clearly visible as well as the quasi-(6x6) superperiodicity. The area where the STM image was taken was further verified to be monolayer graphene by STS measurements. The dI/dV vs. V plotted in Fig. 37d is the average of 320 I/V spectra acquired along an evenly spaced grid where the STM image was obtained. There were no significant differences observed for spectra on and off the hills. In agreement with other STS studies of monolayer graphene on SiC(0001) [93, 95, 104], a minimum at zero bias was observed which does not reach zero and no particular features at the Dirac point (which is located at ca. −0.4 V [101, 102]). A cross section shown as the purple line in Fig. 37c, is plotted in Fig. 37e. A peak to peak maximum variation in height of 35 pm over a length of about 2 nm, along the quasi-(6x6) periodicity was measured. Such a corrugation is typical for monolayer graphene on SiC(0001) [71] and lower than that of the buffer layer which is ~110 pm [73]. From the STM image, it is clear that the surface is clean with no adsorbates or defects.

The monolayer graphene was successively exposed to atomic hydrogen in situ with an atomic flux of ~5.1 x 10^{12} H atoms/(s cm^2) ± 0.1 x 10^{12} H atoms/(s cm^2) for varying lengths of time and subsequently measured by STM and STS. Low coverage, which occurred after a 5 second exposure to atomic hydrogen results in a surface coverage of about 0.8%±0.1%. The graphene-hydrogen system was stable and it was possible to obtain atomic resolution on the surface. After hydrogen exposure of 25 seconds and of 145 seconds (surface coverage around 3.8%±0.2% and 22.1%±0.6%, respectively), the system became exceedingly difficult to image, and good atomic resolution was not possible. However, STS measurements could be acquired.

Figure 38 shows average STS data obtained as a function of increased atomic hydrogen exposure. The black line is from pristine graphene, mirroring the results of previous groups [93, 95, 104]. The red line, obtained after hydrogen exposure for 5 seconds, shows a shoulder at negative voltages that increases for a 25 second exposure (green line). After an atomic hydrogen exposure for 25 seconds, the dI/dV curve indicates that a gap has opened of ~0.4 eV and increases to 1.5 eV after 145 seconds of atomic hydrogen exposure. The formation of a gap is evidence of chemisorption of hydrogen on the monolayer. The gaps are clearly visible in Fig 38b. No significant differences for spectra on and off of the hills was observed. A plausible explanation is that the wavefunction of the chemically adsorbed hydrogen on the graphene is likely to extend more than 1 nm from the C-H bond. Since the spacing between maximally convex areas is

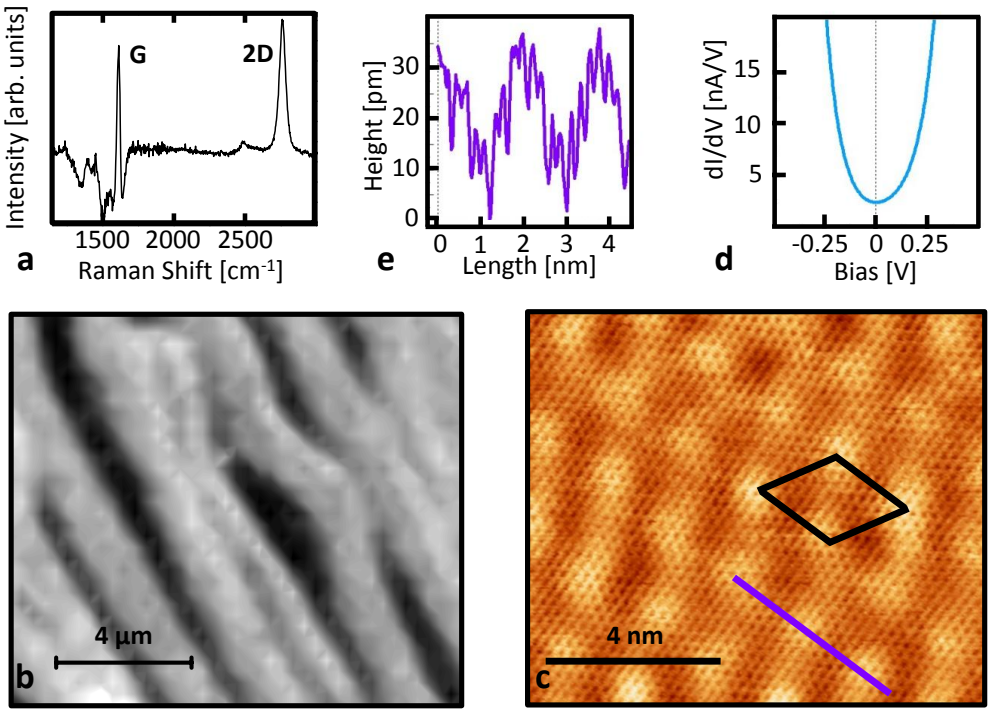

Figure 37: Characterization of monolayer graphene on SiC(0001). a) Raman spectrum averaged over a 12 µm x 12 µm area after subtraction of the SiC background. The spectrum shows the characteristic G and 2D bands at 1610 cm^{-1} and 2700 cm^{-1}. b) Integrated intensity of the 2D peak as a function of the position on the sample. The dark (light) areas show the absence (presence) of the 2D band indicating the absence (presence) of monolayer graphene. c) STM image of monolayer graphene obtained at bias voltage 115 mV and tunneling current 0.3 nA. The diamond shows the quasi-(6x6) superstructure. d) Average STS data obtained in this area of the sample. e) Cross section taken along the purple line indicated in c.

less than 2 nm, it is therefore possible that the wavefunctions overlap leading to a smoothing of the STS data.

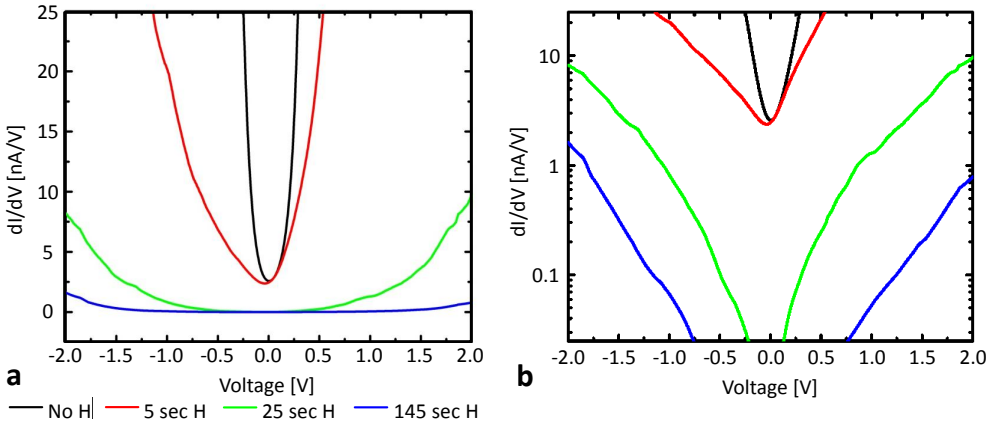

Figure 38: STS of monolayer graphene upon hydrogen exposure plotted on (a) a linear and (b) a logarithmic scale. The black curve corresponds to pristine graphene. The red curve corresponds to a low coverage of hydrogen (5 second hydrogenation). The green and blue curves are for higher coverages (25 seconds and 145 seconds of hydrogenation, respectively). The increasing tendency towards insulating behavior is in agreement with the saturation of the π-bonds and the opening of a gap. Setpoints: 0.3 nA, 115 mV (no H); 0.3 nA, 115 mV (5 sec H); 0.3 nA, 1 V (25 sec H); 0.3 nA, 2 V (145 sec H).

The spectra also explain why STM imaging became increasingly difficult for higher hydrogen coverage. The atomically-resolved images of graphene were obtained at voltages below 200 mV. With increased hydrogenation, the density of states at those bias voltages decreased to zero, excluding the possibility of achieving stable tunneling conditions and therefore images at those biases. Furthermore imaging at a higher bias, outside of the gap, caused the tip to snap towards and away from the sample, probably due to electron induced desorption of hydrogen from the graphene surface. The results presented in the following section are all obtained after a 5 second hydrogenation process.

4.1.2 *Results After a 5 Second Exposure to Atomic Hydrogen*

The STM images of monolayer graphene are dramatically altered when atomic hydrogen bonds to the carbon atoms. Figure 39 shows two STM images of monolayer graphene grown on SiC(0001). The left image is from pristine graphene and the right image is after exposure to atomic hydrogen for 5 seconds. The z-scale is the same in both images emphasizing the out-of-plane modification due to the addition of hydrogen to the surface. After hydrogenation, all the graphene hills have protrusions at the peaks. Looking closely, it is evident that the protrusions are various combinations of hydrogen atoms; para dimers (Fig. 40a), ortho dimers (Fig. 40c) and tetramers (Fig. 40e). In the para dimer configuration (Fig. 40b inset), the two hydrogen atoms are on opposite sides of the hexagon lattice of graphene. When the two hydrogen atoms bind to neighboring carbon atoms they form an ortho dimer (Fig. 40d inset). The tetramers

observed were formed from two ortho dimers on opposite sides of the hexagonal lattice (Fig. 40f inset).

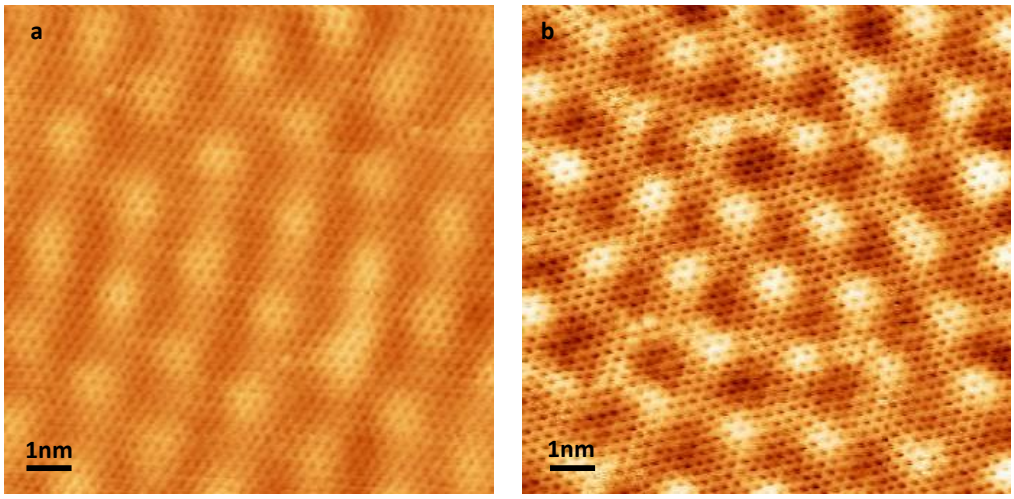

Figure 39: a) STM image of pristine monolayer graphene. b) STM image of monolayer graphene after 5 seconds of hydrogenation. The two images have the same z-scale. Setpoints: a) 115 mV, 0.3 nA, b) 50 mV, 0.3 nA

The hydrogen atom conformations were also identified from the comparison with Density Functional Theory (DFT) calculations, shown in (b, d, f) [3]. These calculations were performed on a model system, consisting of a supercell of 180 C atoms in which the corrugation is obtained by lateral compression [3]. The calculation setup and model system is the same used in previous studies (details provided in reference [3]), but with a lower level of corrugation, in order to better match the natural curvature of the monolayer. After adding H atoms in an ortho, para or tetramer conformation on the hills, the system is relaxed and the electronic structure is calculated. The simulated STM images are then obtained from the iso-electronic density surfaces of the states near the Fermi level (see Fig. 40 caption). The lighter areas are elevated with respect to the darker areas just as in the STM images. Ultimately, the calculated STM images reported in panels b, d, and f confirm the observations of a para dimer, an ortho dimer and a tetramer, as reported in panels a, c, and e, respectively. Notably, the most prevalent configuration found in the STM scans was the tetramer (Fig. 40e), not reported in previous studies. This might be a result of a high concentration of hydrogen on the surface resulting in complex structural arrangements formed by combining basic dimers, which require the least amount of energy to assemble. It is also possible that cooperative effects might induce H atoms to cluster on the graphene surface, a process that has been theoretically proposed [3, 113].

Studies by Dumont et al. [106], of hydrogen adsorption on graphite, reported that the most stable configuration was the ortho dimer, while in our experiment we saw predominantly tetramers, which can be considered pairs of ortho dimers. In 2009, Balog et al., published STM results on monolayer graphene on SiC(0001) showing that hydrogen adsorbs along the superstructure and that the hydrogen adsorbs in dimer configurations [112]. The reported extension of the dimers was more than 10 Å, and they were not atomically resolved. In a

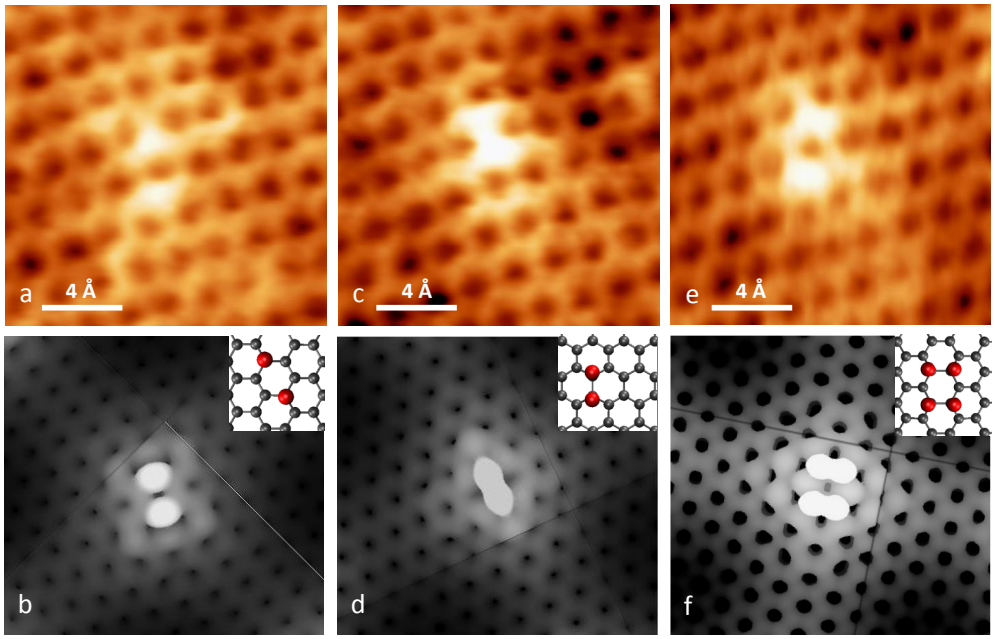

Figure 40: a) A para dimer observed in a scanning tunneling microscopy (STM) image obtained on a monolayer graphene surface after a low dose (5 sec) of atomic hydrogen. b) Simulated STM image obtained from Density Functional Theory (DFT) calculations of the charge density isosurface of the para dimer. c) STM image of an ortho dimer and d) corresponding simulation. e) STM image of a tetramer and f) corresponding theoretical calculation. In each case (b, d, and f), the electronic density is evaluated integrating over a sufficient number of electronic states between the Fermi level and the offset. The insets in b, d, and f are schematics of the various hydrogen configurations observed and described in the respective pairs of panels. Parameters for the STM images were bias voltage 50 mV and tunneling current 0.3 nA. The density charge level for the iso-surfaces and the shades scale are chosen in order to match with experimental images. Higher areas are lighter.

following paper by Šljivančanin et al. [110] from the same group, structures on graphite with the same dimensions were defined as extended hydrogen dimers, configurations with two hydrogen atoms that are not on the same hexagon in the graphene lattice [110]. The study showed both the measured extended dimers covering a length of more than 10 Å [110], which is similar to the work by Balog, et al. [112], and their theoretical simulation [110]. This later work clarifies the discrepancy between the length of the graphene lattice and the length of the hydrogen structures observed by defining the previously known dimers as extended dimers. On the contrary, the dimers observed here are defined as two hydrogen atoms on the same hexagon and are atomically resolved directly on top of the carbon atoms, which agrees with the simulations (Fig. 40). Furthermore, both the ortho and para dimers do not extend beyond 4 Å (Fig. 40).

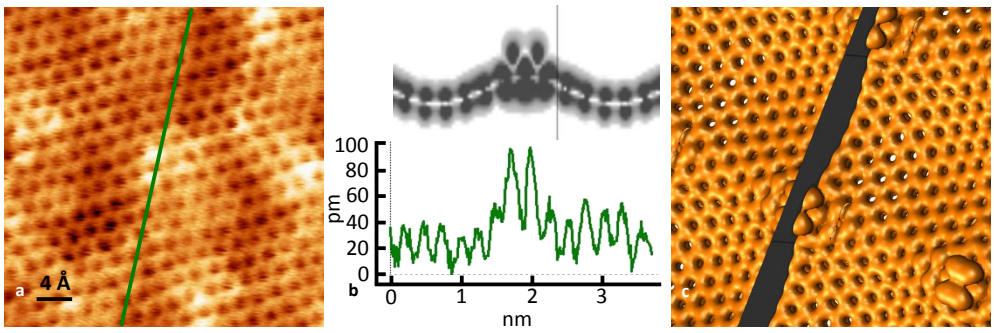

Figure 41: a) STM image with a tetramer located in the center. The cross section shown in the lower half of b was taken along the green line in a. The upper half of b shows the charge density profile for a tetramer cut along the same orientation as a in the charge density map from DFT calculations, represented in c. The same procedure for evaluating the electronic density was used as in the DFT calculations reported in Fig. 40 and the shades scale was selected to correspond with the STM image. The positions of the atoms and the local curvature where the hydrogen atoms are attached are in agreement. Set points: bias voltage 50 mV, tunneling current 0.3 nA.

Figure 41 show an STM image (Fig. 41a) and cross section in green (Fig. 41b) and the theoretical equivalent (Fig. 41c) of a tetramer. The cross sections of the C-H bonds in the STM images affirm that the hydrogen attaches on top of the hills forming protrusions of approximately 50 pm. This is much less than approximately 1.1 Å, the expected C-H bond length [3, 67]. This may be due to the fact that carbon is slightly more electronegative than hydrogen so the electronic wavefunction is pulled towards the graphene surface. The theoretical cross section shows that the hydrogen carbon bond is concentrated more closely to the carbon atom, indicated by the darker shades of grey that start at approximately half the height of the hydrogen wavefunction (Fig. 41b). In fact half of 1.1 Å is 55 pm which agrees quite nicely with the measured change in height of 50 pm.

Remarkably, as visible from the STM images in Fig. 40 and Fig. 41, the hydrogen preferentially binds on sites where the lattice is maximally convexly curved (i.e., lighter contrast areas). DFT calculations relating the local curvature, defined for a given carbon atom as the distance out of the plane defined by the three nearest neighbor carbon atoms, and the hydrogen-graphene bind-

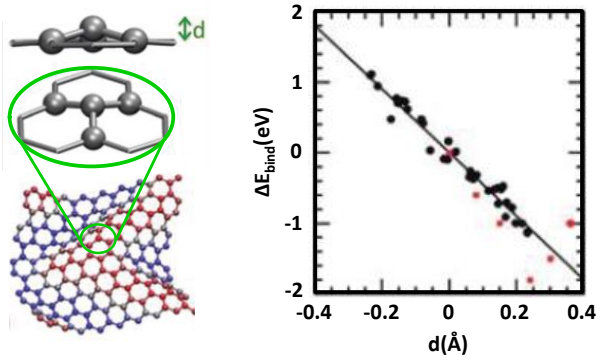

Figure 42: Schematic of local curvature. The linear relationship between C-H binding energy and local curvature is plotted on the right. Figure taken from reference [3].

ing energy are reported in Fig. 42 [3]. The relationship between C-H binding energy and local curvature is linear and varies over 2 eV as the active carbon atom changes from convex, puckering out the plane by 0.2 Å to concavely positioned out the plane by 0.2 Å, as plotted in Fig. 42 [3]. More precisely, the binding energy of a hydrogen atom attached to a convexly puckered carbon atom in the lattice is negative and can become positive as the corrugation is changed to concavity indicating unstable hydrogen bonding sites [3]. Conceptually, the correlation between local graphene curvature and binding energy is comprehensible. This is conceivable because the most favorable formation of an sp^3 bonded molecule such as methane, CH_4, is a tetrahedral structure. The carbon atom is situated in the center of a tetrahedral where the vertices are the positions of the hydrogen atoms. The hydrogen atoms are positioned in such a way as to maximize the distance between any given hydrogen atom. The same concept can be applied to graphene. In other words, the change from an sp^2 to sp^3 hybridization requires the bonds to form the lowest energy configuration that deforms the surface towards a tetrahedral form. The carbon atom in question is pulled out of the plane to maximize the distance between the neighboring carbon atoms and the hydrogen atom, a tetrahedral conformation analogous to that of methane. If the local curvature is privy to that arrangement, the formation of a C-H bond is more favorable and the barrier for atomic H adsorption is reduced or even eliminated. This is the same rationale that explains why there is no hydrogen attached in the concavely curved areas of the graphene lattice. This is a direct demonstration of the geometrical preferential formation of graphene-hydrogen bonds.

After identifying the stable hydrogen conformations on the locally puckered graphene lattice, the hydrogenated sample was heated in steps of 50°C and subsequently measured by STM in order to measure the desorption energy barrier for hydrogen. Figure 43 is a summary of the main results obtained. The top left STM image shown in Fig. 43 was obtained from pristine graphene. A cross section taken across the surface (blue line) is shown below the STM image and displays a height variation of 40 pm as expected [71]. The average root mean square (RMS) roughness value calculated from this image after noise removal by Gaussian smoothing is 9.92 pm. Following a 5 second exposure to

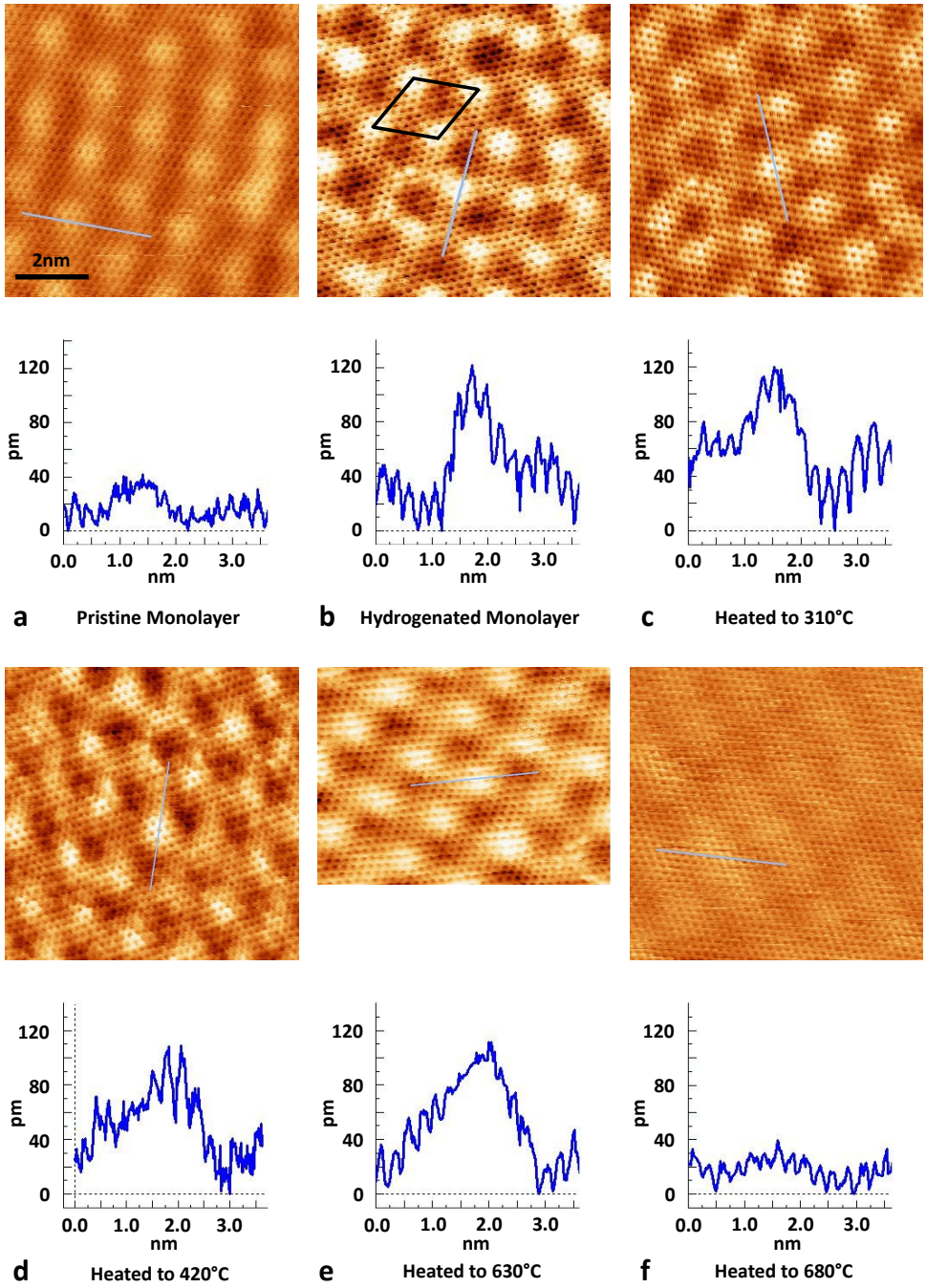

Figure 43: STM images of graphene with corresponding cross sections. a) Pristine graphene (115 mV, 0.3 nA). b) Graphene after exposure to atomic hydrogen for five seconds resulting in a low coverage of hydrogen (50 mV, 0.3 nA). A diamond showing the quasi-(6x6) superstructure is also shown. The cross section below shows a large increase in corrugation due to the C-H bonds on the convex areas of the graphene surface. Selected STM images of graphene after annealing for five minutes in steps of approximately 50°C from 310°C to 680°C are shown: c) 310°C (50 mV, 0.3 nA), d) 420°C (50 mV, 0.3 nA), e) 630°C (50 mV, 0.3 nA), and f) 680°C (112 mV, 0.3 nA). The STM image of graphene after a five minute annealing at 680°C shows a clean surface and a corrugation equivalent to that of the pristine graphene (panel a), indicating that the hydrogen has desorbed from the surface. The color scale and image size is the same for all STM images. All images were obtained at room temperature.

atomic hydrogen, the corrugation dramatically increases reaching a value of 120 pm with an RMS value of 25.6 pm.

This corrugation remains following a 50°C stepwise 5 minute annealing up to 630°C as seen in images acquired at 310°C and 420°C. It is important to note that the bright areas visible on the unheated hydrogenated graphene (Fig. 43) are not strictly restricted to the peaks of the reconstruction but are also visible in the areas with lower local curvature. However, at higher temperatures, the hydrogen remains solely on the peaks of the graphene lattice where the local convex curvature is maximized. This is in agreement with theory [3] which predicts that the C-H bond energy is greatly diminished when the local curvature becomes concave. Finally, when the sample is heated to 680°C, the hydrogen desorbs from the peaks and the graphene relaxes back to the pristine structure, as can be discerned by the cross section. The RMS value calculated from the image at 630°C (Fig. 43) is 17.86 pm, and after heating to 680°C (Fig. 43), it reduces to 8.93 pm, similar to the RMS value of the pristine graphene monolayer. All images in Fig. 43 have the same z-scale to emphasize that hydrogen attaches on the hills, increasing the corrugation along the quasi-(6x6) supercell indicated by the diamond in the hydrogenated STM image in Fig. 43, which has the same periodicity shown on the pristine monolayer.

The corrugation trend is shown in Fig. 44 that reports the RMS values calculated from the height variation of STM images obtained before hydrogenation (black data points), after hydrogenation (red data points) and after progressive heating in steps of 50°C (blue data points). The graphene height variations in the pristine case and after annealing to 680°C are similar. Hydrogenating the sample greatly increases the roughness due to the presence of chemisorbed hydrogen on the surface. This corrugation remains approximately constant up to 630°C. The hydrogen desorbs between 630°C and 680°C. This is duly confirmed by the RMS values which drop back to that of pristine graphene in such temperature range.

Using 650°C (~930K) as the approximate temperature of the hydrogen desorption from the puckered graphene, the only positions where hydrogen is stable at elevated temperatures, a desorption energy barrier of 1.4eV is deduced [114]. The basis of this calculation is the combination of the Arrhenius equation with heating and the assumption of first-order desorption. This assumption was motivated by the observation of dimer arrangements of the hydrogen atoms on graphene similar to what has been observed for hydrogen released from graphite [115] and Rh(110) [116]. First-order desorption means that the hydrogen atoms on the surface desorb in pairs and the pairing process does not occur separately from the desorption process [116]. A second-order process is associated with a multi-step process where for example the hydrogen atoms diffuse across the surface, combine to form pairs and desorb [116]. In the STM experiments we observed hydrogen dimers on the maximally convex areas of the graphene which remained stable until the dimer desorbed. Using the Arrhenius equation with the assumption of a constant heating rate, one has [117]:

$$\frac{E_d}{\kappa T_m} = A\tau_m e^{\frac{-E_d}{\kappa T_m}}. \tag{20}$$

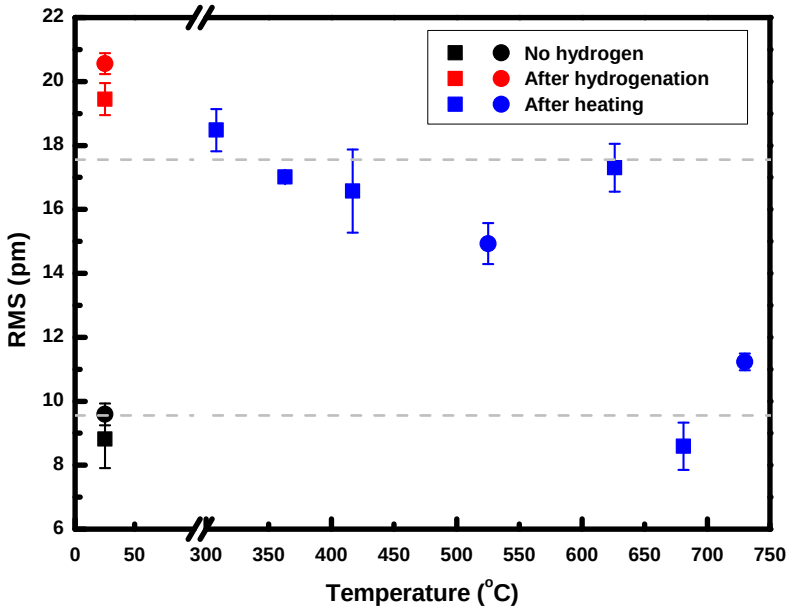

Figure 44: Average root mean square (RMS) values calculated from the height variation of STM images as a function of temperature. The data were collected from two samples (squares and circles). Each point is the average RMS from the images obtained at that temperature. The error bars denote the standard deviation of these averages. The pristine graphene (black data points) has a low corrugation that dramatically increases when the sample is exposed to a low dose (5 sec) of atomic hydrogen (red data points) at room temperature. The RMS remains high until the sample is heated to 680°C at which point the corrugation relaxes back to that of pristine graphene. This occurs because the C-H bonds are broken and the hydrogen desorbs from the graphene. The grey dashed lines are guides to the eye.

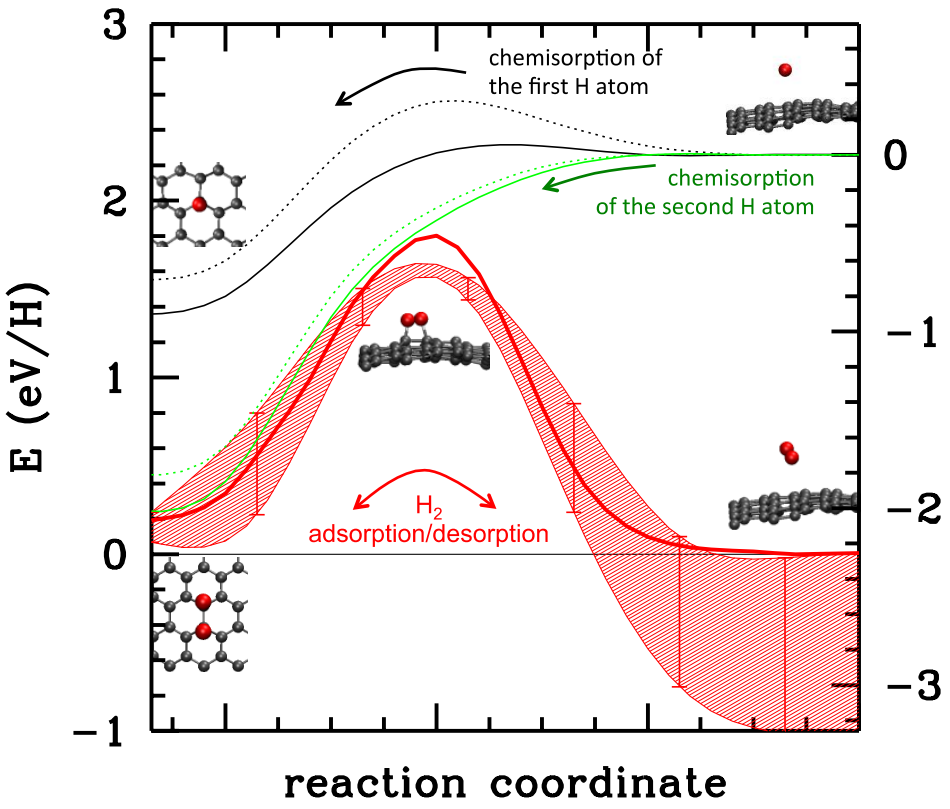

Figure 45: Energy profiles for the reactions of chemisorption of atomic and molecular hydrogen. Black solid line: chemisorption of a single H atom on a convex site. Green solid line: chemisorption of a second H atom in ortho position with respect to the first. For comparison, curves for the same processes on flat graphene are reported as dotted lines. Red solid line: associative desorption/dissociative adsorption profile at 0K temperature. Red shaded band: the same at 300K. The error bars are due to the energy fluctuations of the system. Representative shapshots taken from the simulations are reported. The reaction coordinate is a combination of the H-H and C-H distances (arbitrary units) as calculated in Ref. [3]. The reaction path from adsorbed (left) to desorbed hydrogen (right) is followed by increasing the C-H distance and constraining the H-H distance in a controlled fashion [3]. The energy scales on the left and right y-axis are both in eV, but with two different reference levels: on the left the reference energy level is that of unbound molecular hydrogen; on the right, the energy level is that of the unbound atomic hydrogen. Their offset is the hydrogen molecule dissociation energy per atom.

τ_m is the time after which the desorption temperature T_m is reached, and A the Arrhenius constant (whose typical value is 10^{13} sec^{-1} [107]). We set $\tau_m \sim 10^3$ sec (~15 min), the same order of magnitude as the experimental time to desorb all the hydrogen from the surface. Using this value, one has $\frac{E_d}{\kappa T_m} \sim 33$, hence $E_d \sim 2.8$ eV/molecule or ~ 1.4 eV/atom. The value obtained for the barrier changes less than 0.05 eV with a variation of τ_m over 30 minutes indicating the validity of the approximation of τ_m. Additionally, the Arrhenius constant can be changed by one order of magnitude while the energy barrier changes less than 10%. This value for the desorption barrier is consistent with the DFT calculations (Fig. 45), showing a barrier of 1.55 eV at T = 0 (solid red line in Fig. 45) that decreases to 1.4 eV (red shaded band in Fig. 45) as an effect of the dynamical fluctuations of the graphene sheet at room temperature. The calculations also show that the dimers are approximately as stable as molecular hydrogen and more stable than single hydrogen atoms chemisorbed on graphene. Two effects contribute to this: first, the chemisorption of an isolated H atom is favored on convex areas (difference between dotted and solid black lines in Fig. 45). The local curvature increases after the first H atom is adsorbed because the carbon atom puckers out of the graphene plane [3]. This effect induces adhesion of subsequent H atoms (green lines in Fig. 45). The adhesion of atomic hydrogen becomes thus barrierless. On the other hand, the desorption of hydrogen (or the adsorption of molecules) is a process with a barrier. Starting from the ortho dimer, the first part of the red curve follows the reverse of association, until reaching the activated process, at which point the two H atoms prefer to bind together and form a molecule than to separate, thus following the red line instead of the green one.

In summary, the preferential chemisorption of atomic hydrogen on graphene was demonstrated. Atomic hydrogen did not attach to the locally concave graphene surface, evidence of the instability of the C-H bond at room temperature in these regions. Chemisorption occurred in the areas where the local curvature is maximally convex. This shows that these sites are both the most energetically favorable for hydrogen adsorption and the most stable. The various combinations of hydrogen atoms on graphene were identified: para dimers, ortho dimers and tetramers. Furthermore, the hydrogen adsorbed on the π-bonds of the graphene lattice with lower local curvature tended to desorb at a lower temperature, which indicates a lower binding energy in agreement with previous calculations [3]. The curvature dependent adsorption and desorption of hydrogen combined with the robust quality of graphene provides the basis for the exploitation of graphene as a scaffold for reusable hydrogen storage devices that do not depend on temperature or pressure changes. The hydrogen would be adsorbed in the areas that are convex which can reduce the energy barrier for binding atomic hydrogen to graphene to zero. The hydrogen-carbon bonds on the locally convex areas of graphene are thermally stable up to high temperatures (650°C) as was shown in Section 4.1.2. On the areas where the local curvature is concave, the atomic hydrogen is unstable. The local curvature of the graphene lattice could be inverted changing the convex areas to concave areas which would release the hydrogen. A device that relies on controlling the curvature to adsorb and release hydrogen would transform the field of hy-

drogen storage since such devices would function independent of changes in pressure and temperature. A possible method for modifying the curvature is presented in Chapter 5.

4.1.3 *Hydrogen on Graphene Compared to Other Carbon Materials*

Graphene is a flexible and robust material that chemisorbs hydrogen preferentially based on local curvature. Regions of convex local curvature are the most chemically active and result in strong carbon-hydrogen bonds. There are other carbon based materials with intrinsic curvature such as carbon nanotubes and fullerenes. These materials have been considered for hydrogen storage but both fall short of the standards set by the U.S. Department of Energy [44]. A brief description of the hydrogen adsorption studies on carbon nanotubes and fullerenes will illuminate the advantages of graphene as a possible candidate for hydrogen storage.

Carbon Nanotubes:

Adsorption mechanisms in carbon nanotubes can be divided into chemisorption and physisorption as in graphene. The bulk of theoretical and experimental work on the interaction of hydrogen and carbon nanotubes focuses on physisorption of molecular hydrogen both inside and around the carbon nanotubes [118, 119, 120, 121].

Chen et al. modeled the hydrogen uptake in nanotubes as a function of tube diameter [118]. The mechanism for molecular hydrogen storage in carbon nanotubes appears to be interplay between van der Waals interactions of the carbon atoms and the hydrogen as well as between the hydrogen molecules. The hydrogen is theoretically stored within the carbon nanotubes [118]. The model divides the carbon nanotubes into four groups based on diameter: tiny tubes, (0.9 nm and smaller), small tubes, (1.1 nm to 2.4 nm), medium tubes, (2.6 nm to 4.1 nm), and large tubes, (4.2 nm and up) [118]. Only carbon nanotubes with a diameter of 2.6 nm to 4.1 nm were predicted to achieve 6.5 wt% hydrogen [118]. Smaller carbon nanotubes are strained and when the diameter of the nanotube is tiny, the strain was expected to fracture the nanotube [118]. On the other hand, when the carbon nanotubes are larger than 4.1 nm, collapse is anticipated [118]. This indicates that physisorption inside the carbon nanotubes is not predicted to achieve the ultimate goal set by the DOE of 7.5 wt% [44].

Chemisorption on carbon nanotubes has received less attention but within the theoretical realm of studies, the overwhelming message is binding energy of hydrogen adatoms is found to be inversely proportional to the nanotube radius [122, 123, 124]. The chemisorption of adatoms on carbon nanotubes has been calculated using density functional theory [122]. As the nanotube radius increases, the binding energy of the hydrogen atom is expected to approach that of hydrogen on graphene. Therefore, theoretical calculations on carbon nanotubes [122, 123, 124] are in agreement with those on graphene [3], as the curvature increases, the binding energy increases.

Carbon nanotubes with a diameter greater than 1.25 nm, are not predicted to chemisorb one hydrogen atom per carbon atom in the exo-hydrogenation configuration with all the hydrogen atoms adsorbed on the outside of the nanotube [124]. Completely hydrogenated nanotubes would have the same gravimetric density as graphene, approximately 8 wt% [2]. Only small diameter tubes are expected to be fully hydrogenated and all carbon nanotubes with diameters greater than 1.25 nm will only be partially hydrogenated [123, 124]. It is significant that experimentally, the process of producing and purifying carbon nanotubes is complex and separating carbon nanotubes by exact diameter is extremely challenging. Experiments often remark on the purity of the tubes as well as the range in diameters.

Pioneering hydrogen adsorption experiments were performed by Dillon et al. in 1997 [120]. The single-walled carbon nanotubes were not purified or separated from the soot generated simultaneously during the nanotube production process and consequently made up 0.1 to 0.2 wt% of the sample [120]. The hydrogenation process was performed at 133K and the temperature desorption spectra was acquired [120]. Temperature desorption spectra showed approximately 0.01 wt% of hydrogen desorbed below room temperature [120]. However, Dillon et al. surmised that if the single-walled carbon nanotubes could be purified, the gravimetric hydrogen storage capacity would increase to 5 to 10 wt% [120].

Subsequently, hydrogen adsorption experiments were performed on pretreated single wall carbon nanotubes with an average diameter of 1.85 nm and increased purity with respect to the experiments performed by Dillon et al. [120, 125]. At room temperature in an over pressurized H2 atmosphere of 10 to 12MPa, the carbon nanotubes were found to adsorb up to 4.2 wt% after 6 hours [125]. The hydrogen charging time and gravimetric capacity of the carbon nanotubes did not comply with the standard set by the DOE [44]. When the pressure was reduced to atmospheric pressure, the physisorbed hydrogen was released and amounted to approximately 3.4 wt% [125]. The remaining 0.6 wt% of hydrogen on the carbon nanotubes was released when the nanotubes were heated to 473K indicating that is was chemisorbed [125].

The most similar experiments to the experiments on monolayer graphene on SiC(0001), were performed in 2005 on single-walled carbon nanotubes exposed to atomic hydrogen [126]. The atomic hydrogen formed C-H bonds with the carbon atoms of the nanotubes with diameters ranging from 1 nm to 1.8 nm [126]. The 5.1 ± 1.2 wt% of hydrogen was stable up to 600°C [126]. The gravimetric capacity is markedly higher than in previous experiments deriving from the high purity of the carbon nanotubes. These results are in agreement with theory concluding that the total chemisorption of hydrogen on the nanotubes is not feasible when the diameter is above 1.25 nm [124]. Furthermore, as the diameter of the tubes increased, the local curvature decreased and the chemisorption of hydrogen was expected to respond similar to graphene.

Nikitin et al. [126] measured desorption of hydrogen to be around 600°C where as Liu et al. [125] measured desorption of hydrogen to be around 750°C. Although the reported diameters of the nanotubes in the two experiments are comparable, the discrepancy in temperature when the hydrogen was released may be due to a variation in tube diameters in these experiments. Another

explanation is that nanotubes with smaller diameters cannot relieve the stress due to carbon-hydrogen bonds culminating in weaker C-H bonds. Desorption of chemisorbed hydrogen in these experiments was in the same temperature range as monolayer graphene on SiC, around 650°C. This is surprising given that if the maximally curved region monolayer graphene on SiC(0001) is considered an arc on a circle, the diameter of the circle would be approximately 20 nm, resulting in a local curvature that is much smaller than the carbon nanotubes. A possible explanation for a comparable temperature range for hydrogen desorption from nanotubes with a diameter about 10 to 20 times smaller than that of graphene on SiC(0001), could conceivably be a consequence of the deformational strain on the carbon nanotubes from the hydrogen bonds which cannot be released. The strain may cause the carbon-hydrogen bond to be less stable than in corrugated graphene, where the strain can be released since the graphene layer is not rigidly fixed and the atoms can move to relax the strain.

Graphene curvature can theoretically be tuned to adsorb and release hydrogen. Two methods for modifying the curvature of the carbon nanotubes have been explored theoretically although to our knowledge experimental verification of hydrogen reactivity using these methods has not yet been published.

One potential technique for adsorbing the hydrogen on carbon nanotubes was explored by Srivastava et al. who performed theoretical calculations on bent carbon nanotubes [127]. In the study, the kink is along the length of the nanotube. The results indicated increased chemical reactivity in regions of high local convex curvature which are strained [127]. The kinked areas are characterized by a puckering of the carbon atoms out of the plane produced by the three neighboring carbon atoms. This distortion modified the local conformation of the bonds from sp^2 towards sp^3, spatially isolating the p-orbital resulting in increased chemical reactivity [127]. The binding energy of hydrogen to the kinked carbon nanotubes is predicted to increase by up to 1.6 eV as compared to undistorted nanotubes [127]. These theoretical results provide a possible method for chemisorbing the atomic hydrogen on the convexly bent regions of the nanotubes. Hydrogen is chemically stable on the regions of high local curvature and the difficulty lies in finding a viable method for inverting the curvature to release the chemisorbed hydrogen.

A second approach for tuning the binding energy was explored theoretically by squeezing the nanotube along the length of the tube creating an elliptical cross section rather than circular cross section as observed in a non deformed nanotube [122]. If the hydrogen is attached to a carbon atom on a highly curved region of the carbon nanotube, the C-H bond is expected to be stronger than on a flattened region of the distorted nanotube [122]. As in the bending of the nanotube, the binding energy of hydrogen can be altered, however, to release the hydrogen atoms, the curvature would need to locally change from convex to concave. A facile technique of inverting the curvature in a systematic manner has not yet been discovered. Additionally, it is not clear if the change in local curvature from convex to concave will cause excessive strain on the carbon-carbon bonds leading to fracturing of the nanotube.

In summary, carbon nanotubes have two indubitable disadvantages with respect to graphene. Firstly, the process of producing nanotubes requires extensive treatment to obtain tubes of high purity. These tubes often have a range

of diameters which complicate the possibility of using nanotubes for curvature based hydrogen storage when the state of the starting material is still not well controlled. The range in diameters results in varying degrees of local curvature and subsequently of the energy needed to adsorb and release the hydrogen. Notably, the gravimetric capacity in carbon nanotubes, has not yet reached the standards set by the DOE. The high gravimetric densities reported by Liu et al. [125] and Nikitin et al. [126], have not been easily reproduced [37]. Frequently, the gravimetric densities reported are in the range of 1 wt% at room temperature [37, 128]. The enormous variation in gravimetric capacity is an indication of the inability to repeatedly produce high purity, nanotubes with low variation in the tube diameter. Furthermore, the curvature of the tubes cannot be easily modified rendering the release of hydrogen a difficult feat. Graphene, on the other hand, is currently being produced on large scales by chemical vapor deposition and sold commercially [129]. It has been shown to be flexible and strong even after many changes in the local curvature [130] adding to the appeal of graphene for hydrogen storage.

Fullerenes:

Buckminsterfullerenes are carbon molecules characterized by pronounced curvature given that the radius of the spherical molecules is 3.55 Å. This translates to a protrusion of the carbon atom out of the plane defined by the neighboring carbon atoms of 0.29 Å which would correspond to a C-H binding energy of approximately 1.3 eV (Fig. 42) [3, 131]. Ab initio calculations find exohedrally hydrogenated buckminsterfullerenes with 36 and 48 chemisorbed hydrogen atoms to be the most stable [132]. The latter case translated to approximately 6.2 wt%, falling short of the ultimate gravimetric capacity standard set by the DOE but surpassing the 2017 target [44]. However, experimentally, chemisorption of hydrogen on C_{60} fullerenes has been shown to reach 3.7 wt% which is equivalent to 28 hydrogen atoms per 60 carbon atoms, not 36 atoms [131]. A limiting factor may be the strain induced by the fullerene distortion to accommodate the rehybridization from sp^2 to sp^3 [131].

In 1996, the U.S. Department of Energy financed research on fullerenes for hydrogen storage [133]. The fullerenes were exposed to molecular hydrogen at various temperatures ranging from 375°C to 425°C for 30 minutes which resulted in 0.65 wt% to 2.50 wt% hydrogen adsorption, respectively [133]. Temperature desorption measurements were acquired in the range from 28°C up to 400°C [133]. The temperature was increased at a constant rate, reaching 400°C in 90 minutes and maintained at 400°C for 30 minutes [133]. Below 400°C, the hydrogen released was negligible [133]. The potential barrier a hydrogen atom chemisorbed on the fullerene needed to overcome to break the C-H bond with the fullerene was calculated from the Arrhenius equation to be 0.8 eV per hydrogen atom [133].

The temperature needed to desorb atomic hydrogen from graphene on SiC(0001) was found to be approximately 650°C which corresponds to 1.4 eV per hydrogen atom. The local curvature on graphene on SiC(0001) is significantly lower than that of fullerenes, therefore, a lower temperature is expected to cause hydrogen desorption. The reason why this is not the case, is perhaps

caused by the deformational strain to the fullerene from the hydrogen bonded to the surface. The spherical form of the fullerene may not allow for the strain to dissipate whereas in graphene on SiC(0001), the atoms can adjust to minimize the strain, strengthening the carbon-hydrogen bond.

Fullerenes are produced by a combustion process that results in soot with varying degrees of purity ranging from 2% to 40% [134]. Additional processing can purify the fullerenes to 98% [134]. The fullerenes obtained are a mix of C_{60}, C_{70}, C_{90}, etc. [134]. The varying size of the fullerenes does not lend them to controllable curvature based storage mechanisms. The production and purification processes are a drawback to using fullerenes for hydrogen storage. Furthermore, as in the case of carbon nanotubes, buckminsterfullerenes have not attained the ultimate goals for the gravimetric capacity set by the DOE. In addition, the idea of modulating the binding energy of hydrogen on fullerenes by varying the local curvature is a formidable undertaking not yet explored. Graphene, however, is bendable and not brittle making it an ideal candidate for curvature based hydrogen storage devices with industrial scale production already underway [129].

4.2 HYDROGEN ON THE BUFFER LAYER

The preliminary experiments described in the following section are in agreement with the results presented for the monolayer graphene on SiC (0001).

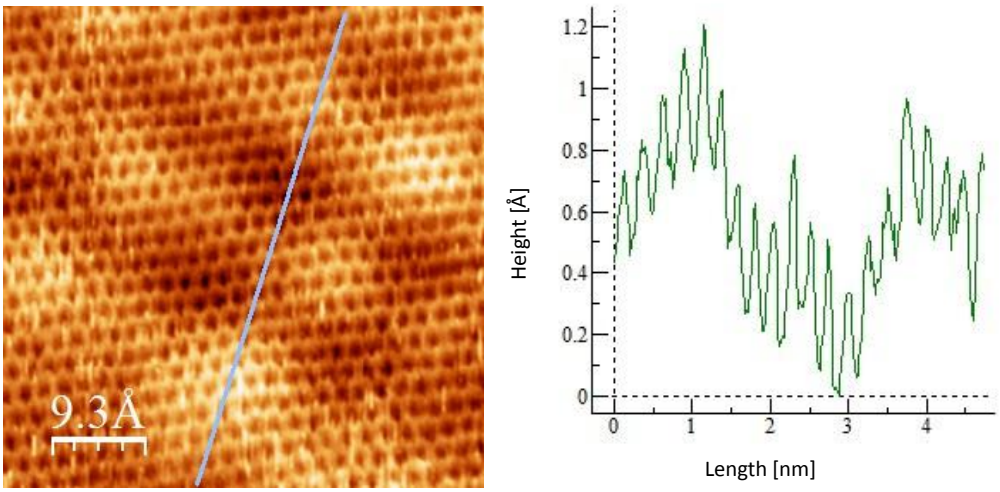

Figure 46: STM image of a pristine buffer layer. The image was Gaussian smoothed to remove the noise. The peak to peak height variation typical of the buffer layer can be observed in the cross section. Setpoint: bias voltage -0.54 V, tunneling current 500 pA.

4.2.1 *Experiment*

The buffer layer was characterized as discussed in detail in chapter 3. The buffer layer was placed in the STM with a base pressure of 1 x 10^{-10}mbar and an-

nealed to 600°C to remove the adsorbates. Figure 46 shows the pristine buffer layer. The cross section shows the intrinsic curvature with a peak to peak height of approximately 1 Å. Next, the sample was exposed to atomic hydrogen in situ at room temperature for 5 seconds at a chamber pressure of 5 x 10^{-9} mbar. A distinct change in the STM images was observed due to the low dose of atomic hydrogen. Hydrogen is found on some of the peaks of the superperiodicity but the effect was minimal. The sample was subsequently hydrogenated for another 20 seconds at the same hydrogen pressure.

4.2.2 *Results*

Comparing the pristine buffer layer to the 5 second hydrogenated buffer layer, a clear change was observed. The surface corrugation is enhanced by the chemisorption of hydrogen on the convex areas of the lattice. In Fig. 47, there are protrusions on the peaks with a change in height of approximately 1 Å in agreement with the C-H bond length [3]. An STM image of the sample after a second atomic hydrogen exposure of 20 seconds is shown in Fig. 48. Considering the first and second hydrogenation STM images together it is apparent that the hydrogen attaches in clusters in the locally convex areas of the superstructure. This further corroborates the theory that predicts the energy barrier can be reduced to zero by curvature effects. The reduction of the energy barrier for adsorbing the second hydrogen atom is a consequence of the local curvature of the graphene lattice, which increases when the first hydrogen atom is attached. As in the case of the monolayer graphene on SiC(0001), the hydrogen bonds to the locally convex carbon atoms in the lattice.

These results must be considered with caution since the corrugation of the buffer layer is due to periodic bonding with the silicon below. From the theoretical models it has been predicted that the atoms in the buffer layer bonded to the silicon are pulled toward the substrate thus creating the high corrugation. This indicates that the areas of local concavity are already sp^3 bonded meaning that in order to create a C-H bond in that area, the bond with the substrate must be broken. Consequently, the buffer layer alone is not an optimal system to test the theory of preferential hydrogen bonding. However, by comparing these initial results with those obtained on the monolayer, it is clear that the hydrogen binds predominantly on the peaks of the buffer layer where the local convexity is maximized. One advantage of the buffer layer system is that the pristine layer has a curvature about 3 times that of the monolayer on SiC(0001) so the adsorption of hydrogen as a function of curvature should be enhanced.

4.3 CONCLUSIONS

The studies on monolayer graphene on SiC(0001) and the preliminary studies on the buffer layer show that the atomic hydrogen adsorbs on areas of high local convex curvature and the C-H bond is stable up to approximately 650°C. The locally concave areas of the lattice are not conducive to chemisorption of hydrogen at room temperature. The instability of atomic hydrogen on the concavely corrugated regions can be exploited, as discussed theoretically [3], to create hy-

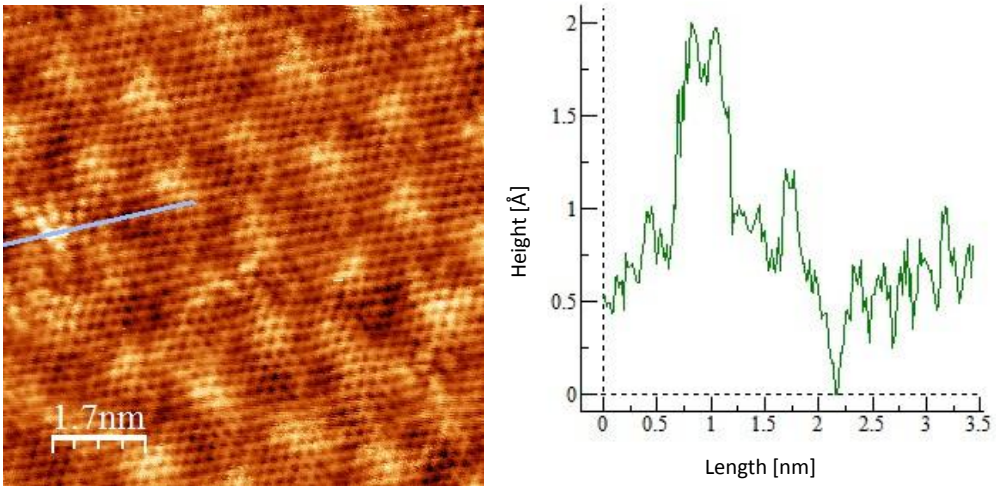

Figure 47: STM image of the buffer layer after a 5 second exposure to atomic hydrogen as described in the text. The image is dramatically different from the pristine buffer layer in Fig. 46. The white spots are hydrogen chemisorbed on the surface. The cross section shows the change in height when compared to the pristine buffer layer (Fig. 46 before exposure to atomic hydrogen) where two hydrogen atoms are chemisorbed on the peak of the buffer layer reconstruction. The peak to peak height increases to approximately 2 Å. Setpoint: bias voltage 0.43 V, tunneling current 500 pA.

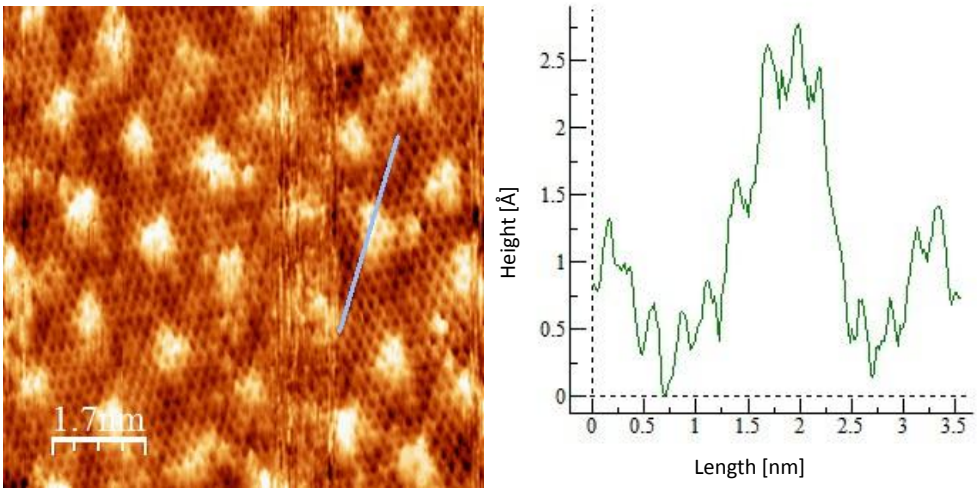

Figure 48: STM image of the buffer layer after a total atomic hydrogen exposure time of 25 seconds as described in the text. The hydrogen atoms (white areas) are clustered on the tops of the super periodicity of the buffer layer as seen in the cross section, further distorting the super periodicity of the buffer layer. A Gaussian smoothing was applied to the image to remove the noise. Setpoint: bias voltage -0.42 V, tunneling current 500 pA.

drogen storage devices that rely on the local curvature alone for adsorbing and desorbing hydrogen.

5 CONCLUSIONS

The interaction between atomic hydrogen and graphene was experimentally explored by STM in view of using graphene as a scaffold to store hydrogen in a safe, compact, inexpensive, and efficient manner. A brief summary of the current state of the art in hydrogen storage materials and devices was presented in chapter 2 indicating the strengths and weaknesses of the various materials in terms of the standards set by the U.S. Department of Energy (DoE). Only the high pressure tanks meet the standards in terms of gravimetric and volumetric density. However, the tanks are not an ideal solution due to safety and cost issues. Furthermore, all hydrogen storage devices relay on a change in pressure and/or temperature for loading and releasing hydrogen. Graphene, on the other hand, theoretically meets the standards set by the DoE with the advantages of being safe, nontoxic, and cheap. However, the differentiating factor setting graphene in a category of its own was presented in the experiments and theory described in the previous sections. Evidence that graphene can adsorb and release hydrogen using a mechanism that exploits solely the local graphene curvature makes graphene the first potential hydrogen storage device that does not depend on temperature or pressure changes. In order to create a graphene based hydrogen storage device, the basic interplay between hydrogen and graphene must be well understood.

Theoretical studies state that by controlling the local curvature of graphene, the atomic hydrogen affinity could be tuned [3]. Convexly curved areas of graphene should form extremely stable carbon-hydrogen bonds at room temperature [3]. On the contrary, hydrogen-carbon bonds are predicted to be unstable in concavely curved areas of the lattice [3]. Finding a suitable system to test these predictions presented a significant hurdle. Exfoliated graphene on SiO_2 is corrugated but the morphology is dependent on the substrate which exhibits an amorphous surface. This would require measuring the exact same area before and after hydrogenation and correlating the measurements with graphene curvature would be a nontrivial task. Furthermore, each specific area of the exfoliated graphene would have a different local curvature. The ideal system is one with an intrinsic periodicity. STM images on a periodically curved system would eliminate the necessity of measuring the same position by making all areas identical. More importantly, it allows for a striking indication of the effect of curvature on the graphene-hydrogen system since all the atomic hydrogen on the same positions on the periodically curved graphene will interact in the same manner. For this purpose, we studied graphene on SiC(0001). It has an intrinsic curvature due to the super periodicity with a change in z of ~40 pm over a length of ~1.8 nm periodically. Scanning tunneling microscopy measurements showed that atomic hydrogen strongly bounds to the carbon atoms with a maximum convex curvature, following the long range periodicity. The results presented in this thesis are in agreement with studies of hydrogen on graphene on Ir(111) [135]. The Moiré pattern of graphene on Ir(111) has a lower cor-

rugation than graphene on SiC(0001). The long range periodicity is ~2.53 nm with a change in z of 27 pm [136]. When graphene on Ir(111) was exposed to atomic hydrogen, the hydrogen followed the Moiré pattern and opened a band gap [135]. We observed an analogous situation on monolayer graphene on SiC(0001). Moreover, we were able to identify the stable hydrogen configurations and compare them to theory. We found para dimers, ortho dimers, and tetramers. This is the first time they have been atomically resolved on a graphene lattice. The C-H bonds on the graphene lattice with maximum local convex curvature were stable up to ~650°C. The hydrogen on areas with lower local curvature desorbed at lower temperatures. Where the local curvature was concave, the hydrogen did not form stable bonds at room temperature. The experimental results presented in this thesis provide the basis for curvature dependent hydrogen storage devices that operate at room temperature and pressure.

Further research is necessary to implement such devices. The next step is to develop a controllable method for inverting the curvature of graphene thereby initializing the adsorption and release of hydrogen. A monolayer graphene membrane is astonishingly strong due to the carbon-carbon bonds and the lack of defects over areas of hundreds of lattice sites [137]. A measure of the stiffness of a material is the Young's modulus. Graphene has a Young's modulus of ~1.0 terapascals [137] but is remarkably flexible [130]. Carbon nanotubes are essentially single sheets of graphene rolled up and can be as small as 3 Å in diameter with a circumference of 4 carbon rings, indicating that a single graphene sheet can withstand extensive deformations [138]. The flexibility of graphene was demonstrated in a scanning tunneling microscopy study where a graphene membrane vibrated between the substrate and the tip with a change in z of ~30 pm when the tip was placed at an appropriate distance from the graphene membrane and an alternating current was applied [130]. The graphene membrane remained intact and no defects were introduced by the vibration of a frequency of ~430 GHz [130]. This experiment shows that vigorously changing the curvature of the graphene lattice does not destroy the graphene, an essential quality that can be exploited for the adsorption and release of hydrogen by inverting the curvature.

Reversing the curvature of graphene to induce spontaneous desorption of chemisorbed hydrogen is one of the principle hurdles to overcome. Simulations by Tozzini et al. of a transverse acoustic phonon traveling through the graphene sheet have been suggested as a potential method for changing the curvature [37]. The curvature will be completely inverted after the wave has propagated half a period, releasing the hydrogen on the areas that were initially locally convex [37]. A piezoelectric substrate was proposed to produce the transverse acoustic phonons [37].

Another possible method for inducing a curvature change is to create a device that pulls the graphene across a curved substrate [139]. It has been shown, experimentally that graphene conforms to the substrate topography but it can slide across the substrate topography when pulled [140, 141]. If hydrogen is chemisorbed to graphene on a substrate with topography of nanoscale hills and valleys, as the graphene is pulled across the surface, the hydrogen will desorb when the graphene that was initially on the convex area is drawn into a concave

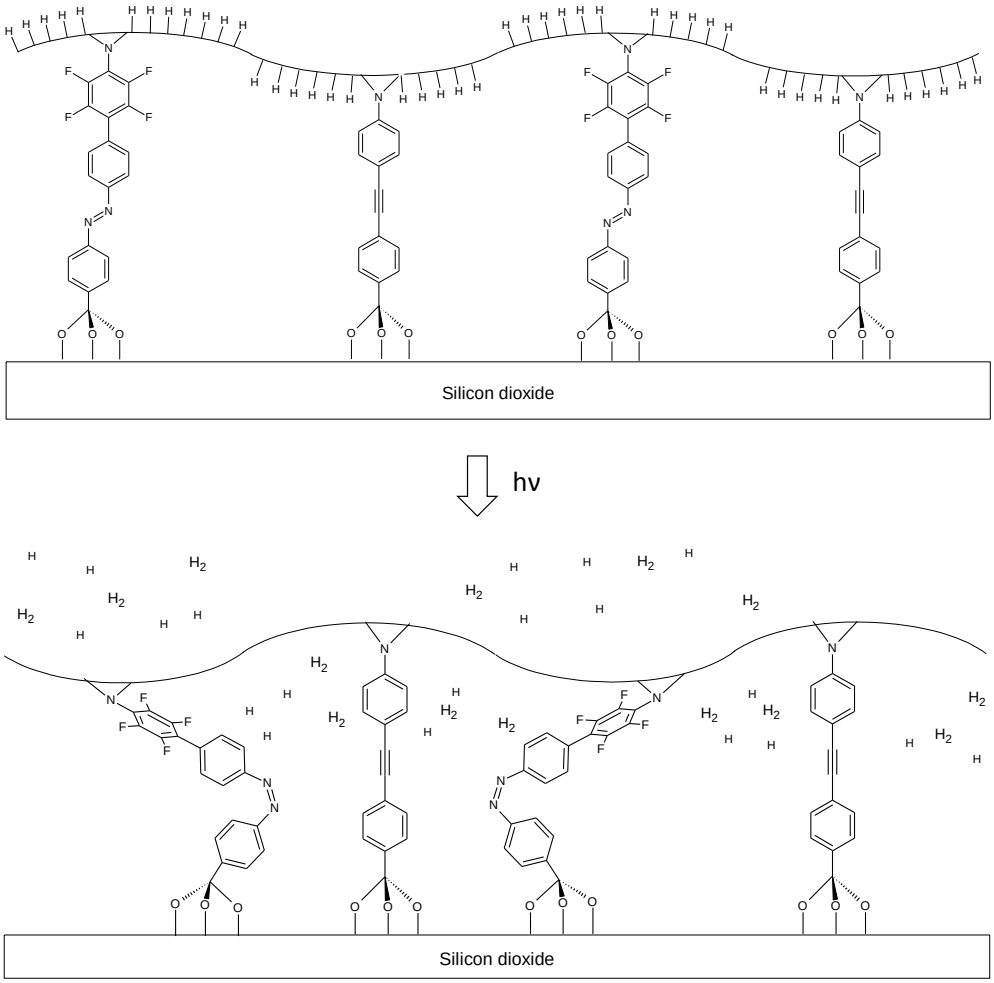

Figure 49: Schematic representation of a hydrogen storage device based on photoswitchable molecules that moderate the graphene curvature. The upper panel shows *trans*-PFPA-azobenzenes pushing the graphene layer out of the plane defined by the shorter non-photoswitchable molecules (diphenylacetylene derivatives). The hydrogen atoms are attached to the convex areas of the graphene lattice. In the lower panel, the photoswitchable molecules have been illuminated with light at a suitable wavelength inducing a conformation change to *cis*-PFPA-azobenzenes. The areas that were initially convex become concave and release the hydrogen.

area on the substrate [139]. Pulling of the graphene membrane can be achieved by building a device with a graphene layer on a nanometer rough substrate such as a Si/SiO_2 wafer with a trench towards one side and a metal electrode attached to the graphene layer [139]. If the pressure outside of the trench is larger than the pressure in the trench, the graphene membrane will bend towards the base of the trench, pulling the graphene layer across the surface of the substrate [140]. Another method for bending the graphene layer towards the trench can be achieved by applying a large voltage difference between the substrate and the graphene sheet [141]. If the graphene is pinned on one side by a metal electrode, as the gate voltage is increased the graphene membrane will slide across the topography of the substrate and release the hydrogen as the local curvature changes from convex to concave [139]. Furthermore, when the gate voltage is reduced to zero, the graphene across the trench once again becomes a flat membrane [141], indicating that the hydrogen desorption process can be performed many times using the same device, an important component to reusable hydrogen storage devices.

A third possibility for inverting the curvature is to functionalize a graphene monolayer with photoswitchable cis\trans molecules. If the photosensitive molecules are attached to a rigid substrate and a graphene monolayer, the corrugation could be controlled by illuminating the molecules with a wavelength that causes them to change configuration from cis to trans or vice versa. Molecules with a perfluorophenylazide (PFPA) portion can covalently attach to graphene [142]. A photoswitchable molecule whose photophysics is well known is azobenzene. Its photophysical features are still active when in contact with graphene [143]. If azobenzene contains a PFPA moiety it would probably covalently bond to graphene with a photoconversion wavelength in or near the UV [143]. If the graphene curvature can be inverted by changing the configuration of the PFPA-azobenzene molecules, a hydrogen storage device could function independent of temperature and pressure changes. In Fig. 49 a hypothetical scheme is depicted. In the upper panel the *trans*-PFPA-azobenzenes are pushing the graphene layer out of the plane defined by the shorter non-photoswitchable molecules (diphenylacetylene derivatives). The hydrogen atoms attach to the convex areas of the graphene layer. The C-H bonds would be stable at room temperature and pressure indefinitely. By illuminating the photoswitchable molecules, the corrugation is inverted and the hydrogen is released (Fig. 49 lower panel). If this concept works, it could be implemented on multilayered graphene structures with photoswitching molecules attached to adjacent sheets. Devices with these qualities have the potential to revolutionize the field of hydrogen storage. These would be the first devices that could adsorb, store, and release hydrogen without changes in pressure or temperature.

Part II

APPENDIX

A

CALCULATING THE ATOMIC FLUX OF HYDROGEN

Known:

The chamber pumping speed is 450 L/s.

The chamber pressure is 5 x 10^{-9} mbar.

Hydrogen gas bottle pressure is 12 bar.

Avogadros number N_A = 6.0221 x 10^{23} molecules/mol.

Using the ideal gas law, PV=nRT, 1 mole of gas occupies 2.03 L at room temperature (293 K) and 12 bar.

R is the universal gas constant with the value 8.324 J/(mol K).

The distance between the atomic hydrogen source and the sample is 10 cm.

When the pressure is constant in the chamber:

Gas in = Gas out

The hydrogen gas flows from the pressurized bottle with a given rate into the chamber. The number of molecules is constant in the chamber when the chamber pressure is constant.

(Hydrogen gas bottle pressure)$*$(Gas flow rate) = (Chamber pressure)$*$(Pumping speed)

Gas flow rate = (Chamber pressure)$*$(Pumping speed)/(Hydrogen gas bottle pressure)

Gas flow rate = (5 x 10^{-9} mbar)$*$(450 L/s)/(12000 mbar) = 1.88 x 10^{-10} L/s

Since all the values on the right side of the equation are known, the gas flow rate can be calculated. The volume of 1 mole of an ideal gas at 12 bar and 293 K can be calculated by the ideal gas law. Therefore, the number of hydrogen molecules can be calculated by the gas flow rate.

Number of H molecules = $N_A$$*$(Gas flow rate)/(2.03 L/mol)

Number of H molecules =

(6.0221 x 10^{23} molecules/mol)$*$(1.88 x 10^{-10} L/s)/(2.03 L/mol)

= 5.56 x 10^{13} molecules/s

The cracking efficiency is given by the manual of the atomic hydrogen source [86] and its value depends on the chamber pressure. See table on the following page.

Number of H atoms = (Number of H molecules)$*$(Cracking efficiency)$*$(2 H atoms/molecule)

Number of H atoms = (5.56 x 10^{13} molecules/s)$*$(1.0)$*$(2 H atoms/molecule)

= 1.11 x 10^{14} H atoms/s

The beam of H atoms diverges from a straight trajectory by 15° when it enters the chamber. With a bit of basic trigonometry, the diameter of the hydrogen beam can be derived at the position of the sample.

Radius of H at the sample = tan(15°)$*$(Distance to sample) = tan(15°)$*$(10 cm)

= 2.679 cm

Area of H at the sample = $\pi$$*$(Radius of H at the sample)^2 = 22.556 cm^2

With the above calculation, the flux of atomic hydrogen is given by:

Flux = (Number of H atoms)/(Area of H at the sample)

Flux = (1.11 x 10^{14} H atoms/s)/(22.556 cm^2) = 4.93 x 10^{12} H atoms/cm^2 s

Chamber pressure (mbar)	Cracking efficency (%)	Atomic hydrogen (H atoms)	Flux (H atoms/cm^2s)
5 x 10^{-7}	0.94	1.05 x 10^{16}	4.64 x 10^{14}
5 x 10^{-8}	0.99	1.01 x 10^{15}	4.88 x 10^{13}
5 x 10^{-9}	1.0	1.11 x 10^{14}	4.93 x 10^{12}
5 x 10^{-10}	1.0	1.11 x 10^{13}	4.93 x 10^{11}

BIBLIOGRAPHY

[1] M. Dresselhaus. Basic research needs for the hydrogen economy. *Argonne National Laboratory, U.S. Department of Energy, Office of Science Laboratory*, 2003.

[2] D. C. Elias, R. R. Nair, S. V. Mohiuddin, T. M. G.and Morozov, P. Blake, M. P. Halsall, A. C. Ferrari, D. W. Boukhvalov, M. I. Katsnelson, A. K. Geim, and K. S. Novoselov. Control of graphene's properties by reversible hydrogenation: Evidence for graphane. *Science*, 323:610–613, 2009.

[3] V. Tozzini and V. Pellegrini. Reversible hydrogen storage by controlled buckling of graphene layers. *J. Phys. Chem. C*, 115:25523–25528, 2011.

[4] Fabor-Castell. Pencils- a history. *http://www.faber-castell.ie/34507/All-About-Pencils/Pencils-A-History/default_ news.aspx*, 2008.

[5] Berol. History of pencils. *http://www.berol.co.uk/historyofpencils.html*.

[6] P. Avouris. Graphene: Electronic and photonic properties and devices. *Nano Lett.*, 10:4285–4294, 2010.

[7] A. Jorio, M. Dresselhaus, R. Saito, and G. F. Dresselhaus. Raman spectroscopy in graphene related systems. *Wiley-VCH*, Fourth Edition, 2011.

[8] J.-C. Charlier, X. Gonze, and J.-P. Michenaud. Graphite interplanar bonding: electronic delocalization and van der waals interaction. *Europhys. Lett.*, 28(6):403–408, 1994.

[9] A. K. Geim and K. S. Novoselov. The rise of graphene. *Nature Mat.*, 6:183–191, 2007. And references there in.

[10] K. S. Novoselov, A. K. Geim, S. V. Morozov, D. Jiang, Y. Zhang, S. V. Dubonos, I. V. Grigorieva, and A. A. Firsov. Electric field effect in atomically thin carbon films. *Science*, 306:666–669, 2004.

[11] K. S. Novoselov, D. Jiang, F. Schedin, T. J. Booth, V. V. Khotkevich, S. V. Morozov, and A. K. Geim. Two-dimensional atomic crystals. *Proc. Natl. Acad. Sci. USA*, 102:10451–10453, 2005.

[12] S. Roddaro, P. Pingue, V. Piazza, V. Pellegrini, and F. Beltram. The optical visibility of graphene: Interference colors of ultrathin graphite on SiO_2. *Nano Lett.*, 7(9):2707–2710, 2007.

[13] L. Gao, J. R. Guest, and N. P. Guisinger. Epitaxial graphene on Cu(111). *Nano Lett.*, 10:3512–3516, 2010.

[14] P. W. Sutter, J.-I. Flege, and E. A. Sutter. Epitaxial graphene on ruthenium. *Nature Materials*, 7:406–411, 2008.

[15] C. R. Dean, A. F. Young, I. Meric, C. Lee, L. Wang, S. Sorgenfrei, K. Watanabe, T. Taniguchi, P. Kim, K. L. Shepard, and J. Hone. Boron nitride substrates for high-quality graphene electronics. *Nature Nanotechnology*, 5:722–726, 2010.

[16] R. Kundu. Tight-binding parameters for graphene. *Modern Physics Letters B*, 25(3):163–173, 2011.

[17] P. R. Wallace. The band theory of graphite. *Physical Review*, 71(9):622–634, 1947.

[18] G. M. Rutter. Atomic scale properties of epitaxial graphene grown on SiC(0001). *Thesis, Georgia Institute of Technology*, 2008.

[19] A. H. Castro Neto, F. Guinea, N. M. R. Peres, K. S. Novoselov, and A. K. Geim. The electronic properties of graphene. *Reviews of modern physics*, 81:109–162, 2009.

[20] L. A. Falkovsky. Symmetry constraints on phonon dispersion in graphene. *Physics Letters A*, 372:5189–5192, 2008.

[21] J. Yan. Raman spectroscopy of graphene. *Thesis Columbia University*, 2009.

[22] V. Raman. The molecular scattering of light. *Nobel Lecture*, 1930.

[23] P. Y. Yu and M. Cardona. Fundamentals of semiconductors: Physics and materials properties. *Springer*, Fourth Edition, 2010.

[24] W. H. Weber and R. (Eds.) Merlin. Raman scattering in materials science. *Springer*, 2000.

[25] J. Yan, Y. Zhang, S. Goler, P. Kim, and A. Pinczuk. Raman scattering and tunable electron-phonon coupling in single layer graphene. *Solid State Commun.*, 143:39–43, 2007.

[26] J. Yan, Y. Zhang, P. Kim, and A. Pinczuk. Tuning of electron-phonon coupling in graphene. *Phys. Rev. Lett.*, 98:166802, 2007.

[27] S. Pisana, M. Lazzeri, C. Casiraghi, K. S. Novoselov, A. K. Geim, A. C. Ferrari, and F. Mauri. Breakdown of the adiabatic Born-Oppenheimer approximation in graphene. *Nature Materials*, 6:198–201, 2007.

[28] Z. H. Ni, H. M. Wang, Y. Ma, J. Kasim, Y. H. Wu, and Z. X. Shen. Tunable stress and controlled thickness modification in graphene by annealing. *ACS Nano*, 2(5):1033–1039, 2008.

[29] M. Huang, H. Yan, C. Chen, D. Song, T. F. Heinz, and J. Hone. Phonon softening and crystallographic orientation of strained graphene studied by Raman spectroscopy. *Proc. Natl. Acad. Sci. U. S. A.*, 106(18):7304–7308, 2009.

[30] A. C. Ferrari, J. C. Meyer, V. Scardaci, C. Casiraghi, M. Lazzari, F. Mauri, S. Piscanec, D. Jiang, K. S. Novoselov, S. Roth, and A. K. Geim. Raman spectrum of graphene and graphene layers. *Phys. Rev. Lett.*, 97:187401, 2006.

[31] A. C. Ferrari. Raman spectroscopy of graphene and graphite: Disorder, electron-phonon coupling, and doping and nonadiabatic effects. *Solid State Communications*, 143:47–57, 2007.

[32] S. Goler, J. Yan, V. Pellegrini, and A. Pinczuk. Raman spectroscopy of magneto-phonon resonance in graphene and graphite. *Solid State Commun.*, 152:1289–1293, 2012.

[33] J. Yan, S. Goler, T. D. Rhone, M. Han, R. He, P. Kim, V. Pellegrini, and A. Pinczuk. Observation of magnetophonon resonance of Dirac fermions in graphite. *Phys. Rev. Lett.*, 105:227401, 2010.

[34] Y. Kim, J. M. Poumirol, A. Lombardo, N. G. Kalugin, T. Georgiou, Y. J. Kim, K. S. Novoselove, A. C. Ferrari, J. Kono, O. Kashuba, V. I. Fal'ko, and D. Smirnov. Filling-factor-dependent magnetophonon resonance with circularly polarized phonons in graphene revealed by high-field magneto-Raman spectroscopy. *arXiv*, (1211.6094v1), 2012.

[35] N. S. Lewis. Powering the planet. *Engineering and Science*, (2):13–23, 2007.

[36] G. W. Crabtree and M. S. Dresselhaus. The hydrogen fuel alternative. *MRS Bulletin: Harnessing Materials for Energy*, 33:421–428, 2008.

[37] V. Tozzini and V. Pellegrini. Prospects for hydrogen storage in graphene. *Phys. Chem. Chem. Phys.*, 15:80–89, 2013.

[38] U. S. Department of Energy. Module 1: Hydrogen properties. *Hydrogen fuel cell engines and related technologies, http://www1.eere.energy.gov/hydrogenandfuelcells/tech_validation/ pdfs/fcm01r0.pdf*, pages 1–41, 2001.

[39] B. Esper, A. Badura, and M. Rögner. Photosynthesis as a power supply for (bio-)hydrogen production. *TRENDS in Plant Science*, 11(11):543–549, 2006.

[40] L. Schlapbach and A. Züttel. Hydrogen-storage materials for mobile applications. *Nature*, 414:353–358, 2001.

[41] C. Kerekes. Rv calculators-liquid weight calculator. *http://changingears.com/rv-sec-calc-liquid-weight.shtml?d=& d_ unit=m& g=& g_ unit=m& p=& p_ unit=m& w=& w_ unit=m*, 2012.

[42] D. K. Ross. Hydrogen storage: The major technological barrier to the development of hydrogen fuel cell cars. *Vacuum*, 80:1084–1089, 2006.

[43] BMW. Bmw cleanenergy: Overview. *http://www.bmw.com/com/en/insights/technology/cleanenergy/phase_2/cleanenergy.html*.

[44] U. S. Department of Energy. DoE targets for onboard hydrogen storage systems for light-duty vehicles. *http://www1.eere.energy.gov/hydrogenandfuelcells/storage/pdfs/targets_onboard_hydro_storage.pdf*.

[45] R. K. Ahluwalia, T. Q. Hua, J.-K. Peng, S. Lasher, K. McKenney, J. Sinha, and M. Gardiner. Technical assessment of cryo-compressed hydrogen storage tanks systems for automotive applications. *International Journal of Hydrogen Energy*, 35:4171–4184, 2010.

[46] N. Sirosh. Department of energy hydrogen composite tank program. *http://www1.eere.energy.gov/hydrogenandfuelcells/pdfs/merit03 - /44_quantum_neel_shirosh.pdf*.

[47] U. S. Department of Energy. FCT hydrogen storage: Gaseous and liquid hydrogen storage. *http://www1.eere.energy.gov/hydrogenandfuelcells /storage/hydrogen_storage.html*, 2008.

[48] B. Sakintuna, F. Lamari-Darkrim, and M. Hirscher. Metal hydrid materials for solid hydrogen storage: A review. *International Journal of Hydrogen Energy*, 32:1121–1140, 2007.

[49] M. L. Christian and K.-F. Aguey-Zinsou. Core-shell strategy leading to high reversible hydrogen storage capacity for $NaBH_4$. *ACS Nano*, 6(9):7739–7751, 2012.

[50] H. Imamura, K. Masanari, M. Kusuhara, H. Katsumoto, and T. Sumi. High hydrogen storage capacity of nanosized magnesium synthesized by high energy ball-milling. *Journal of Alloys and Compounds*, 386(1-2):211–216, 2005.

[51] M. Zhu, H. Wang, L. Z. Ouyang, and M. Q. Zeng. Composite structure and hydrogen storage properties in Mg-based alloys. *International Journal of Hydrogen Energy*, 31(2):251–257, 2006.

[52] K.-J. Jeon, H. R. Moon, A. M. Ruminski, B. Jiang, C. Kisielowski, R. Bardhan, and J. J. Urban. Air-stable magnesium nanocomposites provide rapid and high-capacity hydrogen storage without using heavy-metal catalysts. *Nature Materials*, 10:286–290, 2011.

[53] L. J. Murray, M. Dinca, and J. R. Long. Hydrogen storage in metal-organic frameworks. *Chem. Soc. Rev.*, 38:1294–1314, 2008.

[54] N. L. Rosi, J. Eckert, M. Eddaoudi, D. T. Vodak, J. Kim, M. OâKeeffe, and O. M. Yaghi. Hydrogen storage in microporous metal-organic frameworks. *Science*, 300:1127–1129, 2003.

[55] S. S. Kaye, A. Dailly, O. M. Yaghi, and J. R. Long. Impact of preparation and handling on the hydrogen storage properties of Zn_4O(1,4-benzendicarboxylate)$_3$ (MOF-5). *J. Am. Chem. Soc.*, 129:14176–14177, 2007.

[56] B. Panella, M. Hirscher, H. Pütter, and U. Müller. Hydrogen adsorption in metal-organic frameworks: Cu-MOFs and Zn-MOFs compared. *Adv. Funct. Mater.*, 16:520–524, 2006.

[57] J. C. Wang, R. W. Murphy, F. C. Chen, R. O. Loutfy, E. Veksler, and W. Li. Hydrogen storage in fullerenes and in an organic hydride. *Proceedings*

of the 1998 U. S. DOE Hydrogen Program Review, (NREL/CP-570-253115), 1998.

[58] P.-J. Tsai, C.-H. Yang, W.-C. Hsu, W.-T. Tsai, and J.-K. Chang. Enhancing hydrogen storage on carbon nanotubes via hybrid chemical etching and Pt decoration employing supercritical carbon dioxide fluid. *International Journal of Hydrogen Energy*, 37:6714–6720, 2012.

[59] S. Patchovskii, J. S. Tse, S. N. Yurchenko, L. Zhechkov, T. Heine, and G. Seifert. Graphene nanostructures as tunable storage media for molecular hydrogen. *Proc. Natl. Acad. Sci. USA*, 102(30):10439–10444, 2005.

[60] H. Lee, J. Ihm, M. L. Cohen, and S. G. Louie. Calcium-decorated graphene-based nanostructures for hydrogen storage. *Nano Lett.*, 10:793–798, 2010.

[61] C. Ataca, E. Aktürk, S. Ciraci, and H. Ustunel. High-capacity hydrogen storage by metalized graphene. *Appl. Phys. Lett.*, 93(043123), 2008.

[62] E. Beheshti, A. Nojeh, and P. Servati. A first-principes study of calcium-decorated, boron-doped graphene for high capacity hydrogen storage. *Carbon*, 49:1561–1567, 2011.

[63] E. Durgun, S. Ciraci, and T. Yildirim. Functionalization of carbon-based nanostructures with light transition-metal atoms for hydrogen storage. *Phys. Rev. B*, 77(085405), 2008.

[64] Z. M. Ao and F. M. Peeters. High-capacity hydrogen storage in Al-adsorbed graphene. *Phys. Rev. B*, 81(205406), 2010.

[65] H. An, C.-S. Liu, Z. Zeng, C. Fan, and X. Ju. Li-doped B_2C graphene as potential hydrogen storage medium. *Appl. Phys. Lett.*, 98(173101), 2011.

[66] T. Mashoff, M. Takamura, S. Tanabe, H. Hibino, F. Beltram, and S. Heun. Hydrogen storage with titanium-functionalized graphene. *Appl. Phys. Lett.*, 103(013903), 2013.

[67] J. O. Sofo, A. S. Chaudhari, and G. D. Barber. Graphane: A two-dimensional hydrocarbon. *Phys. Rev. B*, 75(153401), 2007.

[68] K. V. Emtsev, A. Bostwick, K. Horn, J. Jobst, G. L. Kellogg, L. Ley, J. L. McChesney, T. Ohta, S. A. Reshnov, J. Röhrl, E. Rotenberg, A. K. Schmid, D. Waldmann, H. B. Weber, and T. Seyller. Towards wafer-size graphene layers by atmospheric pressure graphitization of silicon carbide. *Nature Mater.*, 8:203–207, 2009.

[69] U. Starke and C. Riedl. Epitaxial graphene on SiC(0001) and SiC(000 − 1): from surface reconstructions to carbon electronics. *J. Phys.: Condens. Matter*, 21:134016, 2009.

[70] C. Riedl, C. Coletti, and U. Starke. Structural and electronic properties of epitaxial graphene on SiC(0001): a review of growth, characterization, transfer doping and hydrogen intercalation. *J. Phys. D: Appl. Phys.*, 43:374009, 2010.

[71] F. Varchon, P. Mallet, J.-Y. Veuillen, , and L. Magaud. Ripples in epitaxial graphene on the Si-terminated SiC(0001). *Phys. Rev. B*, 77:235412, 2008.

[72] C. Riedl, U. Starke, J. Bernhardt, M. Franke, and K. Heinz. Structural properties of the graphene-SiC(0001) interface as a key for the preparation of homogeneous large-terrace graphene surfaces. *Phys. Rev. B*, 76:245406, 2007.

[73] S. Goler, C. Coletti, V. Piazza, P. Pingue, F. Colangelo, V. Pellegrini, K. V. Emtsev, S. Forti, U. Starke, F. Beltram, and S. Heun. Revealing the atomic structure of the buffer layer between SiC(0001) and epitaxial graphene. *Carbon*, 51:249–254, 2013.

[74] J. B. Hannon, M. Copel, and R. M. Tromp. Direct measurement of the growth mode of graphene on SiC(0001) and SiC(000$\bar{1}$). *Phys. Rev. Lett.*, 107:166101, 2011.

[75] C. Riedl, C. Coletti, T. Iwasaki, A.A. Zakharov, and U. Starke. Quasi-free-standing epitaxial graphene on SiC obtained by hydrogen intercalation. *Phys. Rev. Lett.*, 103:246804, 2009.

[76] G. Binning and H. Rohrer. Scanning tunneling microscopy - from birth to adolescence. *Nobel lecture*, December 8, 1986.

[77] J. Tersoff and D. R. Hamann. Theory and application for the scanning tunneling microscope. *Phys. Rev. Lett.*, 50(25):1998–2001, 1983.

[78] C. J. Chen. Introduction to scanning tunnelling microscopy. *Oxford University Press, New York*, Second Edition:Chapter 1, 2008.

[79] J. Bardeen. Tunnelling from a many-particle point of view. *Phys. Rev. Lett.*, 6(2):57–59, 1961.

[80] J. Tersoff and D. R. Hamann. Theory of the scanning tunneling microscope. *Phys. Rev. B*, 31(2):805–813, 1985.

[81] C. J. Chen. Introduction to scanning tunnelling microscopy. *Oxford University Press, New York*, Second Edition:174–175, 2008.

[82] C. J. Chen. Introduction to scanning tunnelling microscopy. *Oxford University Press, New York*, Second Edition:53, 2008.

[83] R. M. Stroscio, J. A. Feenstra and A. P. Fein. Electronic structure of the Si(111) 2x1 surfaces by scanning-tunneling microscope. *Phys. Rev. Lett.*, 57(20):2579–2582, 1986.

[84] J. P. Ibe, P. P. Jr. Bey, S. L. Brandow, R. A. Brizzolara, N. A. Burnham, D. P. DiLella, K. P. Lee, C. R. K. Marrian, and R. J. Colton. On the electrochemical etching of tips for scanning tunnelling microscopy. *J. Vac. Sci. Technol. A*, 8(4):3570–3575, 1990.

[85] C. J. Chen. Introduction to scanning tunnelling microscopy. *Oxford University Press, New York*, Second Edition:314–316, 2008.

[86] Tectra. H-flux atomic hydrogen source, operating manual. *http://www.tectra.de/hydrogen.htm*.

[87] J. Röhrl, M. Hundhausen, K. V. Emtsev, T. Seyller, R. Graupner, and L. Ley. Raman spectra of epitaxial graphene on SiC(0001). *Appl. Phys. Lett.*, 92:201918, 2008.

[88] A. Tiberj, J. R. Huntzinger, N. Camara, P. Godignon, and J. Camassel. Raman spectrum and optical extinction of graphene buffer layers on the Si-face of 6H-SiC. *arXiv:1212.1196*, 2012.

[89] S. Forti, K. V. Emstev, C. Coletti, A. A. Zakharov, C. Riedl, and U. Starke. Large-area homogeneous quasifree standing epitaxial graphene on SiC(0001): electronic and structural characterization. *Phys. Rev. B*, 84:125449, 2011.

[90] J. Tamayo and R. Garcia. Deformation, contact time, and phase contrast in tapping mode scanning force microscopy. *Langmuir*, 12:4430–4435, 1996.

[91] D. A. Schmidt, T. Ohta, and T. E. Beechem. Strain and charge carrier coupling in epitaxial graphene. *Phys. Rev. B*, 84:235422, 2011.

[92] W. Chen, H. Xu, L. Liu, X. Gao, D. Qi, and et al. Peng, G. Atomic structure of the 6H-SiC(0001) nanomesh. *Surf. Sci.*, 596:176–186, 2005.

[93] P. Lauffer, K. V. Emtsev, R. Graupner, T. Seyller, L. Ley, S. A. Reshanov, and H. B. Weber. Atomic and electronic structure of few-layer graphene on SiC(0001) studied with scanning tunneling microscopy and spectroscopy. *Phys. Rev. B*, 77:155426, 2008.

[94] F. Owman and P. Mårtensson. The SiC(0001) $(6\sqrt{3}\text{x}6\sqrt{3})$ reconstruction studied with STM and LEED. *Surf. Sci.*, 369:126–136, 1996.

[95] G. M. Rutter, N. P. Guisinger, J. N. Crain, E. A. A. Jarvis, M.D. Stiles, T. Li, P. N. First, and J. A. Stroscio. Imaging the interface of epitaxial graphene with silicon carbide via scanning tunneling microscopy. *Phys. Rev. B*, 76:235416, 2007.

[96] P. Mallet, F. Varchon, C. Naud, L. Magaud, C. Berger, and J. Y. Veuillen. Electron states of mono- and bilayer graphene on SiC probed by scanning-tunneling microscopy. *Phys. Rev. B*, 76:041403, 2007.

[97] K. V. Emtsev, F. Speck, T. Seyller, L. Ley, and J. D. Riley. Interaction, growth, and ordering of epitaxial graphene on SiC(0001) surfaces: A comparative photoelectron spectroscopy study. *Phys. Rev. B*, 77:155303, 2008.

[98] S. Kim, J. Ihm, H. J. Choi, and Y.-W. Son. Origin of anomalous electronic structures of epitaxial graphene on silicon carbide. *Phys. Rev. Lett.*, 100:176802, 2008.

[99] Y. Qi, S. H. Rhim, G. F. Sun, M. Weinert, and L. Li. Epitaxial graphene on SiC(0001): More than just honeycombs. *Phys. Rev. Lett.*, 105:085502, 2010.

[100] A. Das, S. Pisana, B. Chakraborty, S. Piscanec, S. K. Saha, U. V. Waghmare, K. S. Novoselove, H. R. Krishnamurthy, A. K. Geim, A. C. Ferrari, and A. K. Sood. Monitoring dopants by raman scattering in an electrochemically top-gated graphene transistor. *Nat. Nanotechnol.*, 3:210–215, 2008.

[101] T. Ohta, A. Bostwick, J. L. McChesney, T. Seyller, K. Horn, and E. Rotenberg. Interlayer interaction and electronic screening in multilayer graphene investigated with angle-resolved photoemission spectroscopy. *Phys. Rev. Lett.*, 98:206802, 2007.

[102] C. Coletti, C. Riedl, D. S. Lee, B. Krauss, L. Patthey, K. von Klitzing, J. H. Smet, , and U. Starke. Charge neutrality and band-gap tuning of epitaxial graphene on SiC by molecular doping. *Phys. Rev. B*, 81:235401, 2010.

[103] Y. Zhang, V. W. Brar, F. Wang, C. Girit, Y. Yayon, M. Panlasigui, A. Zettl, and M. F. Crommie. Giant phonon-induced conductance in scanning tunneling spectroscopy of gate tunable graphene. *Nat. Phys.*, 4:627–630, 2008.

[104] V. W. Brar, Y. Zhang, Y. Yayon, T. Ohta, J. L. McChesney, A. Bostwick, E. Rotenberg, K. Horn, and M. F. Crommie. Scanning tunneling spectroscopy of inhomogeneous electronic structure in monolayer and bilayer graphene on SiC. *Appl. Phys. Lett.*, 91:122102, 2007.

[105] J. Y. Veuillen, F. Hiebel, L. Magaud, P. Mallet, and F. Varchon. Interface structure of graphene on SiC: an ab initio and STM approach. *J. Phys. D: Appl. Phys.*, 43:374008, 2010.

[106] F. Dumont, F. Picaud, C. Ramseyer, D. Girardet, Y. Ferro, and A. Allouche. Model for thermal desorption of hydrogen atoms from a graphite surface based on kinetic Monte Carlo simulations. *Phys. Rev. B.*, 77(233401), 2008.

[107] L. Hornekær, Ž. Šljivančanin, W. Xu, R. Otero, E. Rauls, I. Stensgaard, E. Lægsgaard, B. Hammer, and F. Besenbacher. Metastable structures and recombination pathways for atomic hydrogen on the graphite (0001) surface. *Phys. Rev. Lett.*, 96(156104), 2006.

[108] L. Hornekær, W. Xu, E. Lægsgaard, and F. Besenbacher. Long range orientation of meta-stable atomic hydrogen adsorbate clusters on the graphite (0001) surface. *Chem. Phys. Lett.*, 446:237–242, 2007.

[109] T. Zecho, A. Güttler, X. Sha, B. Jackson, , and J. Küppers. Adsorption of hydrogen and deuterium atoms on the (0001) graphite surface. *J. Chem. Phys.*, 117(18):8486–8492, 2002.

[110] Ž. Šljivančanin, E. Rauls, L. Hornekær, W. Xu, F. Besenbacher, and B. Hammer. Extended atomic hydrogen dimer configurations on the graphite(0001) surface. *J. Chem. Phys.*, 131(084706), 2009.

[111] L. Hornekær, E. Rauls, W. Xu, Ž. Šljivančanin, R. Otero, I. Stensgaard, E. Lægsgaard, B. Hammer, and F. Besenbacher. Clustering of chemisorbed

H(D) atoms on the graphite (0001) surface due to preferential sticking. *Phys. Rev. Lett.*, 97(186102), 2006.

[112] R. Balog, B. Jørgensen, J. Wells, E. Lægsgaard, P. Hofmann, F. Besenbacher, and L. Hornekær. Atomic hydrogen adsorbate structures on graphene. *J. Am. Chem. Soc.*, 131:8744–8745, 2009.

[113] D. Stojkovic, P. Zhang, P. E. Lammert, and V. H. Crespi. Collective stabilization of hydrogen chemisorptions on graphenic surfaces. *Phys. Rev. B.*, 68(195406), 2003.

[114] P. A. Webb. Introduction to chemical adsorption analytical techniques and their applications to catalysis. *Micromeritics Instrument Corp.*, 2003.

[115] E. A. Denisov and T. N. Kompaniets. Kinetics of hydrogen release from graphite after hydrogen atom sorption. *Physica Scripta*, T94:128–131, 2001.

[116] E. Vesselli, M. Campaniello, A. Baraldi, L. Bianchettin, C. Africh, F. Esch, S. Lizzit, and G. Comelli. A surface core level shift study of hydrogen-induced ordered structures on Rh(110). *J. Phys. Chem. C*, 112:14475–14480, 2008.

[117] D. P. Woodruff and T. A. Delchar. Modern techniques of surface science. *Cambridge University Press: New York*, 1994.

[118] Y. L. Chen, B. Liu, J. Wu, Y. Huang, H. Jiang, and K. C. Hwang. Mechanics of hydrogen storage in carbon nanotubes. *J. Mech. Phys. Solids*, 56:3224–3241, 2008.

[119] J. S. Arellano, L. M. Molina, A. Rubio, M. J. López, and J. A. Alonso. Interaction of molecular and atomic hydrogen with (5,5) and (6,6) single-wall carbon nanotubes. *J. Chem. Phys.*, 117:2281–2288, 2002.

[120] A. C. Dillon, K. M. Jones, T. A. Bekkedahl, C. H. Kiang, D. S. Bethune, and M. J. Heben. Storage of hydrogen in single-walled carbon nanotubes. *Nature*, 386:377–379, 1997.

[121] S. H. Barghi, T. T. Tsotsis, and M. Sahimi. Chemisorption, physisorption and hysteresis during hydrogen storage in carbon nanotubes. *Int. J. Hydrogen Energ.*, 39:1390–1397, 2014.

[122] O. Gülseren, T. Yildirim, and S. Ciraci. Tunable adsorption on carbon nanotubes. *Phys. Rev. Lett.*, 87(116802), 2001.

[123] A. Bilić and J. D. Gale. Chemisorption of molecular hydrogen on carbon nanotubes: A route to effective hydrogen storage? *J. Phys. Chem. C*, 112:12568–12575, 2008.

[124] T. Yildirim, O. Gülseren, and S. Ciraci. Exo-hydrogenated single wall carbon nanotubes. *Phys. Rev. B*, 64(075404), 2001.

[125] C. Liu, Y. Y. Fan, H. T. Cong, H. M. Cheng, and M. S. Dresselhaus. Hydrogen storage in single-walled carbon nanotubes at room temperature. *Science*, 286(1127), 1999.

[126] A. Nikitin, H. Ogasawara, D. Mann, R. Denecke, Z. Zhang, H. Dai, K. Cho, and A. Nilsson. Hydrogenation of single-walled carbon nanotubes. *Phys. Rev. Lett.*, 95(225507), 2005.

[127] D. Srivastava, D. W. Brenner, J. D. Schall, K. D. Ausman, M. F. Yu, and R. S. Ruoff. Predictions of enhanced chemical reactivity at regions of local conformational strain on carbon nanotubes: Kinky chemistry. *J. Phys. Chem. B.*, 103:4330–4337, 1999.

[128] B. Panella, M. Hirscher, and S. Roth. Hydrogen adsorption in different carbon nanostructures. *Carbon*, 43:2209–2214, 2005.

[129] Ltd. Bluestone Global Tech. Grat-film^{TM}. *http://bluestonegt.com/products/grat-filmtm/*, 2013.

[130] T. Mashoff, M. Pratzer, V. Geringer, T. J. Echtermeyer, M. C. Lemme, M. Liebmann, and M. Morgenstern. Bistability and oscillatory motion of natural nanomembranes appearing within monolayer graphene on silicon dioxide. *Nano Letters*, 10:461–465, 2010.

[131] P. Ruffieux, O. Gröning, M. Bielmann, P. Mauron, L. Schlapbach, and P. Gröning. Hydrogen adsorption on sp^2-bonded carbon: Influence of the local curvature. *Phys. Rev. B*, 66(245416), 2002.

[132] T. Guo and G. E. Scuseria. Ab initio calculations of tetrahedral hydrogenated buckminsterfullerene. *Chem. Phys. Lett.*, 191(6), 1992.

[133] J. C. Wang, F. C. Chen, and R. W. Murphy. Thermal management technology for hydrogen storage: Fullerene option. *In Proceedings of the 1996 US. DOE Hydrogen Program Review, U.S. Department of Energy*, 2:819–829, 1996.

[134] Nano-C Inc. Fullerene product portfolio. *http://www.nano-c.com/fullereneprod.html*, 2011.

[135] R. Balog, B. Jørgensen, L. Nilsson, M. Andersen, E. Rienks, M. Bianchi, M. Fanetti, E. Lægsgaard, A. Baraldi, S. Lizzit, Z. Sljivancanin, F. Besenbacher, B. Hammer, T. G. Pedersen, P. Hofmann, and L. Hornekær. Bandgap opening in graphene induced by patterned hydrogen adsorption. *Nature Mat.*, 9:315–319, 2010.

[136] A. T. N'Diaye, S. Bleikamp, P. Feibelman, and T. Michely. Two-dimensional Ir cluster lattice on a graphene Moiré on Ir(111). *Phys. Rev. Lett.*, 97(215501), 2006.

[137] C. Lee, X. Wei, J. W. Kysar, and J. Hone. Measurement of the elastic properties and intrinsic strength of monolayer graphene. *Science*, 321:385–388, 2008.

[138] X. Zhao, Y. Liu, T. Suzuki, R. O. Jones, and Y. Ando. Smallest carbon nanotube is 3A in diameter. *Physical Review Letters*, 92(12):125502, 2004.

[139] Y. Murata. Private communication. 2014.

[140] A. L. Kitt, Z. Qi, S. Rémi, H. S. Park, A. K. Swan, and B. B. Goldberg. How graphene slides: measurement and theory of strain-dependent frictional forces between graphene and sio_2. *Nano Lett.*, 13:2605–2610, 2013.

[141] W. Bao, K. Myhro, Z. Zhao, Z. Chen, W. Jang, L. Jing, F. Miao, H. Zhang, C. Dames, and C. N. Lau. In situ observation of electrostatic and thermal manipulation of suspended graphene membranes. *Nano Lett.*, 12:5470–5474, 2012.

[142] L.-H. Liu and M. Yan. Simple method for the covalent immobilization of graphene. *Nano Lett.*, 9(9):3375–3378, 2009.

[143] N. Peimyoo, J. Li, J. Shang, X. Shen, C. Qiu, L. Xie, W. Huang, and T. Yu. Photocontrolled molecular structural transition and doping in graphene. *ACS Nano*, 6(10):8878–8886, 2012.